**NTNU – Trondheim**
Norwegian University of
Science and Technology

# Acoustic and Mechanical Properties of Microbubbles Stabilized by Polymeric Nanoparticles

Andreas Finnøy

Master of Science in Physics and Mathematics
Submission date: June 2013
Supervisor: Catharina de Lange Davies, IFY

Norwegian University of Science and Technology
Department of Physics

# Acoustic and Mechanical Properties of Microbubbles Stabilized by Polymeric Nanoparticles

Andreas Finnøy

17. June 2013

**Abstract**

This thesis examines acoustic and mechanical properties of microbubbles stabilized by poly(butyl cyanoacrylate) nanoparticles. The microbubbles are developed with the purpose of being applied in combination with ultrasound as a novel drug delivery system to tumors. Knowledge about the acoustic and mechanical properties is essential to understand the interaction between ultrasound and the microbubbles, their drug delivery potential and stability in the circulatory system.

Microbubbles with different surfactant proteins, average diameter, and nanoparticle batches are analyzed and compared in this work.

Backscattered power and attenuation of ultrasound waves propagating through a suspension of microbubbles are measured in the frequency range 1-20 MHz. The measurements are done with microbubbles suspended in a sample chamber in a water tank. Attenuation are measured by using the same ultrasound transducer both for transmit and receive. The attenuation coefficients are plotted as function of frequency, and theoretical attenuation spectra calculated from the Church model and the Hoff model are fitted to the experimental spectra by appropriate estimation of viscoelastic properties of the microbubble shell. Using casein as a surfactant protein is found to increase the shear modulus and viscosity of the shell (avg. shear modulus and viscosity $30.7 \pm 2.8$ MPa and $1.29 \pm 0.06$ Ns/m$^2$) compared to when Bovine Serum Albumin (BSA) is used (avg. shear modulus and viscosity $7.4 \pm 1.1$ MPa and $0.46 \pm 0.03$ Ns/m$^2$). Microbubbles with BSA as surfactant protein and smaller average diameter (avg. shear modulus and viscosity $14.4 \pm 2.5$ MPa and $0.25 \pm 0.03$ Ns/m$^2$) show higher shear modulus, but lower viscosity compared to when the average diameter is larger.

The backscatter is received with a transducer different from the transmit transducer. When a transmit transducer with center frequency 1 MHz is used, the scatter spectra display higher harmonics at pressures above 5-15 kPa. Furthermore, destruction takes place above 170 kPa, but apparently more for the microbubbles with casein rather than BSA as surfactant protein. Smaller microbubbles seem to exhibit more resistance against destruction.

Measurements of microbubble shell elasticity is performed using atomic force microscopy (AFM) by applying nanoscale compressions (up to 500 nN) with a flat cantilever on isolated nanoparticle-stabilized microbubbles. Values of the Young's modulus are found by fitting obtained force-deformation curves to the simple theoretical Reissner model. In accordance with the attenuation measurements, the results indicate that the casein microbubbles (avg. Young's modulus $37 \pm 17$ MPa) have higher Young's modulus than BSA microbubbles (avg. Young's modulus $15 \pm 7.8$ MPa). The shell thickness is assumed to be 150 nm. A linear relation between the Young's modulus and the diameter is found for the microbubbles with casein as surfactant protein.

## Sammendrag

I denne masteroppgava blir akustiske og mekaniske egenskaper av mikrobobler stabilisert av poly(butyl cyanoacrylate) nanopartikler analysert. Mikroboblene er utviklet med formål å kunne bli brukt i kombinasjon med ultralyd som et nytt system for levering av legemiddel til kreftvev. Kunnskap om de akustiske og mekaniske egenskapene er viktig for å forstå interaksjonen mellom ultralyd og mikrobobler, potensialet for å levere legemidler, og stabiliteten i sirkulasjonen.

Mikrobobler med ulike surfaktantproteiner, gjennomsnittsstørrelser, og nanopartikkeltyper er analysert og sammenliknet i dette arbeidet.

Tilbakespredt effekt og attenuasjon av ultralydbølger som propagerer gjennom en mikroboblesuspensjon, er målt i frekvensområdet 1-20MHz. Målingene er gjort med mikroboblene lokalisert i et prøvekammer i en vanntank. Attenuasjon er målt ved å bruke den samme ultralydtransduceren for overføring og mottak. Attenuasjonskoeffisientene er plottet som funksjon av frekvens, og teoretiske attenuasjonsspektra bestemt ved hjelp av Church modellen og Hoff modellen, er tilpasset de eksperimentelle spektra ved å velge passende verdier for viskoelastiske skallparametrene. Å bruke casein som et surfaktantprotein er vist å øke skjærmodulusen og viskositeten av skallet (gj. snitt skjærmodulus og viskositet $30.7 \pm 2.8$ MPa og $1.29 \pm 0.06$ Ns/m$^2$) sammenliknet med å bruke Bovine Serum Albumin (BSA) (gj. snitt skjærmodulus og viskositet $7.4 \pm 1.1$ MPa og $0.46 \pm 0.03$ Ns/m$^2$). Mikrobobler med BSA som surfaktantprotein og mindre gjennomsnittsdiameter (gj. snitt skjærmodulus og viskositet $14.4 \pm 2.5$ MPa og $0.25 \pm 0.03$ Ns/m$^2$) har høyere skjærmodulus, men lavere viskositet enn de større mikroboblene.

Spredning forårsaket av mikrobobler er mottatt med en transducer ulik sendetransduceren. Når en sendetransducer med senterfrekvens 1 MHz er brukt, viser spredningsspektra flere harmoniske når trykket er høyere enn 5-15 kPa. I tillegg er destruksjon av bobler observert for trykk over 170 kPa, men tilsynelatende mer for mikrobobler med casein istedenfor BSA som surfaktantprotein. Mindre mikrobobler ser ut til å være mer resistante mot destruksjon.

Målinger av mikrobobleskallelastisiteten er gjort ved å bruke AFM og ved å gjøre kompresjoner med nanokrefter (opptil 500 nN) med en flat cantilever på isolerte nanopartikkelstabiliserte mikrobobler. Verdier for Young's modulus er funnet ved å tilpasse den målte kraft-deformasjonskurven til en teoretisk modell utviklet av Reissner. I samsvar med attenuasjonsmålingene viser resultatene at casein-mikrobobler (gj. snitt Young's modulus $37 \pm 17$ MPa) har høyere Young's modulus enn BSA-mirkobobler (gj. snitt Young's modulus $15 \pm 7.8$ MPa). Skalltykkelsen er antatt å være 150 nm. En lineær sammenheng mellom Young's modulus og diameteren er funnet for casein-mikrobobler.

# Preface

This Master's thesis concludes the Master of Science degree in Applied Physics and Mathematics at Norwegian University of Science and Technology. The specialization option has been Biophysics and Medical Technology.

My work for this thesis has been carried out at Department of Physics, NTNU, spring 2013, and has been a part of the project "Multifunctional nanoparticles in cancer diagnosis and therapy"which is an interdisciplinary collaboration between several research groups at NTNU, SINTEF and St. Olav's Hospital.

I would like to thank my supervisors for guidance and support with my Master's thesis. Catharina de Lange Davies (Professor, Dept. of Physics) has been my main supervisor and provided useful suggestions and constructive comments during the experimental work and report writing. For the part related to acoustic characterization, Yngve Hofstad Hansen (PhD student, Dept. of Physics) helped me to get started with the experimental work and shared knowledge and valuable advices about methods. Sigrid Berg (Research Scientist, SINTEF, Dept. of Medical technology) conducted the measurements during ultrasound imaging and transducer characterization, and together with Rune Hansen (Senior Research Scientist, SINTEF, Dept. of Medical technology), assisted in development of the experimental setup and discussion of results. During the experimental work with AFM, Astrid Bjørkøy (Department of Physics) gave appreciated assistance. Finally, I would like to thank Ýrr Mørch (Research Scientist, SINTEF Materials and Chemistry) for providing microbubbles and nanoparticles and information about them in addition for giving helpful interpretations of results.

# Contents

# Chapter 1

# Introduction

An increased incidence of cancer in Norway has been reported the last decades [1]. Simultaneously, there is a growing knowledge and understanding about the processes governing uncontrolled cell growth and proliferation causing tumorigenesis, resulting in a continuing development of new anti-tumor drugs. However, drawbacks shared with conventional chemotherapeutic agents are their systemic distribution in the body upon intravenous administration, and the subsequent poor delivery to the cancer cells in the tumor, in addition to unfavorable impact on healthy cells [2]. The demand for more efficient and targeted therapeutics is therefore high.

Recent years have witnessed significant progresses the field of nanotechnology, enabling opportunities for improved cancer therapy and diagnosis. Novel nanoscience-based drug delivery systems have been developed that show promising effects in overcoming physiological barriers in the circulatory system and the tumor, while at same time reducing adverse contact with normal tissue [3].

In this thesis, micrometer-sized gas bubbles (microbubbles) synthesized by SINTEF Materials and Chemistry will be characterized. What is interesting about this type of microbubble, is that polymeric nanoparticles are located in the microbubble shell, possibly stabilizing the bubble along with surfactant proteins. Together they are supposed to act as a theranostic system for use in oncology, both providing diagnostic information and therapeutic function. Encapsulating drug molecules in the nanoparticles prevents drug from leaking out of capillaries and target healthy cells. Because of their relatively large size, and in particular when bound to microbubbles, the nanoparticles are restricted from leaving non-leaky vessels in normal tissue, and systemic exposure to the drugs is hindered. On the other hand, the larger pores in tumor vessels can facilitate extravasation of nanoparticles. It is therefore desired that the nanoparticles can be released from the microbubble in the leakier vessels of the tumor. This can be achieved with high-intensity ultrasound focused into the tumor. Effects of ultrasound on microbubbles can induce collapse, subsequent release of nanoparticles and produce various phenomena, like shock waves and microjetting, that may assist the nanoparticles to reach the cancer cells. Besides, the microbubbles work as contrast agent for ultrasound, allowing imaging of the drug delivery vehicles in the body. However, the microbubbles are still in the development phase. An optimized selection of materials and parameters during the production depends on a thoroughly understanding of the microbubble and its interaction with ultrasound. How a microbubble behaves in an ultrasound field is largely determined by the mechanical properties of the shell.

The aim of this master thesis is to characterize and obtain acoustic and mechanic properties of the microbubbles stabilized by polymeric nanoparticles.

Specifically, the acoustic properties are studied in terms of attenuation and scatter of ultrasound from the microbubbles. Measurements of acoustic attenuation can give information about resonance frequency and damping of the microbubbles, and when the data is compared to theoretical models of an oscillating bubble, viscoelastic properties of the shell can be acquired. Scattering measured from the microbubbles show more directly the ability of the microbubble to function as a contrast agent. In addition, spectra of scattering provide information about non-linear properties and potential microbubble destruction.

Direct measurements of the mechanical properties are performed with atomic force microscopy (AFM). In essence, the microbubbles are compressed between a flat cantilever and a glass surface, and the applied force and the resulting deformation is measured. The experimental data is compared with a theoretic model, and a quantification of the elastic properties of the microbubble shell can be obtained.

# Chapter 2

# Theory

## 2.1 Tumor biology and therapeutic barriers

The ability of drugs to be successfully delivered to cancerous tissue is impacted by the physiology and micro-environment of the tumor. A malignant tumor consists of cells with mutations in oncogenes or tumor suppressor genes causing uncontrolled proliferation. The rapidly replicating cells accumulate, overproduce intracellular matrix molecules, and displace healthy cells. For a tumor to grow more than 1-2 $mm^3$, nutrition must be acquired by other means than diffusion. Tumors with cells that are able to produce proangiogenic factors can develop a vasculature and enhance the access of nutrition.The angiogenesis is more chaotic than in healthy tissue because of uncontrolled release of factors, and in contrast to the hierarchic ordered vessel network seen in normal tissue, a heterogeneous and meandering distribution of vessels is evolved in the tumor, both in terms of distance to the cells, diameter and permeability. In addition, smooth muscles and nerve innervation are absent at most vessels, causing a low and variable blood flow. While some regions can have a rich blood supply, other regions are badly covered and develop hypoxia, acidity and necrosis [4, 5, 6].

In general, blood vessels are leakier in tumors than in normal tissue because of large fenestrae and abnormal basement membranes. Excessive fluid and waste products are normally drained from the interstitial space of tissue by the lymphatic system. Tumors have in comparison a low drainage because of their dysfunctional lymphatic system. Molecules and fluid are then allowed to gather in the interior of the tumor. The phenomenon caused by the highly permeable blood vessels and the poor lymphatic draining is called the enhanced permeability and retention effect (EPR) [7, 8].

### Barriers for drug delivery

Therapeutic agents are mostly given systemically by oral administration or intravenous injection. When present in the blood, several barriers need to be passed before the drugs can reach and affect the cancer cells with high enough concentration to have therapeutic efficacy.

Before entering the site of the tumor, the drugs are subject to be cleared by the mononuclear phagocyte system (MPS). MPS, also known as the reticuloendothelial system (RES), consists of macrophages and monocytes in the spleen, lymph nodes and the blood, in addition to Kupffer cells in the liver. The system targets and get rids of foreign objects by means of opsonization and phagocytosis [9].

The blood is filtered in the glomeruli of the kidney. The renal system purifies the blood and removes foreign objects. Agents with diameter less than 10 nm are likely filtered out of the circulatory system [5].

As the therapeutic agents enter vessels in the tumor, the unorganized tumor vasculature and the heterogeneous blood flow prevent an even distribution of drugs. Regions of the tumor with absence of vessels or with low blood flow receive less or no drugs [5].

The agents need to leave the circulatory system through the vessel walls. This happens by diffusion and convection. Diffusion is a transport process caused by random collisions between the drug particles and water molecules and other molecules. The particles will tend to move in the direction of lower concentration. This transport process is slow and depends on particle size, viscosity and temperature. When there is a pressure difference between the vessels and the interstitium, convection will dominate as a transport process for the larger particles. However, the EPR effect, in addition to rapid cellular proliferation in a limited area, will produce a high interstitial pressure in the interior of the tumor. The high interstitial fluid pressure reduces the convection, and diffusion is therefore the main transport process in parts of the tumor. The diffusivity of the therapeutic agents is further reduced by the highly viscous interstitial fluid and steric and electrostatic barriers caused by extracellular matrix molecules [6].

The function of most chemotherapeutic agents is to impair cell division. The agents must then be internalized by cancer cells by phagocytosis or endocytosis. In the intracellular vesicles, endosomes and lysosomes, the drugs are subjected to low pH and enzymatic activity, potentially degrading the drug components or modifying drug activity [5].

Eventually, there is observed pumps on the cell membrane that can actively transport chemotherapeutic agents out of the cancer cells. Cancer cells with high expression of these efflux pumps may acquire resistance to the drugs [10].

Hence, there are many challenges and barriers preventing drugs to reach cancer cells, and strategies that aim to overcome these are developed or under developing [6].

## 2.2 Nanoparticles and drug delivery

Nanoparticles have gained attention in the field of drug delivery because of their ability to encapsulate medicine. Drugs confined to the nanoparticle are protected from clearance and degradation that otherwise can occur to free drug particles, and they are hindered from reaching healthy cells, potentially reducing unwanted adverse effects. In addition, by employing the EPR effect, the nanoparticles can be passively targeted to tumors, so that the delivery efficacy of therapeutic agents is increased. The most common nanoparticle materials include: lipids, proteins, carbon, metals and virus-based nanoparticles. Liposomes have been a leading nanomedicine system. They are self-assembling colloid structures composed of lipid bilayers around an aqueous compartment. Liposomes can therefore carry both hydrophilic and lipophilic drug molecules [5, 11].

Polymers are attractive nanoparticle materials because of their versatile structural and functional properties. A spherical polymer matrix composition with drugs distributed evenly throughout the matrix is called a nanosphere. Nanocapsules have a polymer shell separating the core from the environment. The drug can be located in the core or at the membrane. Usually, the drug is released by diffusion or degradation of the polymer, however, nanoparticles can also be developed to respond to environmental or external triggers [5, 2].

Nanoparticles used for drug delivery are evaluated by their ability to remain in the blood circulation for a long enough time, neither too long or too short, and their ability to overcome biological barriers and target specific cells and tissue. Their shape, size and surface characteristics influence these abilities. When used in cancer therapy, a proper design should be in accordance with current knowledge about tumor biology.

To avoid clearance by the renal filtration, the nanoparticle diameter must be larger than 10 nm. However, nanoparticles larger than 100-250 nm are desired in order to avoid leakage out of capillaries in normal tissue [12]. In addition, a higher drug load is enabled in larger nanoparticles. The upper limit is restrained by the transport rate in the interstitial tissue and the permeability of the tumor capillaries. It has been shown that particles larger than 400 nm are therapeutically inadequate because of the slow diffusion in the interstitium [5]. The cutoff size of the pores of the tumor vessels is between 400 and 600 nm [12]. A compromise must therefore be made between transport rate, drug load and tumor selectivity. In order to fully take advantage of the EPR effect, a diameter of around 150 nm has been considered ideal [13].

### Multifunctional nanoparticles

The surface of a nanoparticle can be modified to alter environmental interactions. It has been shown that covering the surface with PEG (polyethylene glycol) results in prolonged circulation time. The PEG creates a hydrophilic protective layer around the nanoparticles and shields it from opsonin adsorption and subsequent clearance by the RES [9, 14].

In addition, surface modifications of nanoparticles can be used to more actively distinguish tumor tissue from healthy tissue. Ligands added to the nanoparticle surface can recognize specific receptors on the endothelium cell membrane of tumor capillaries and increase the therapeutic effectiveness [15].

It is desired to be able to detect and track nanoparticles during initial research, animal studies and *in vivo* in patients. Such multifunctional nanoparticles can be obtained by an additional encapsulation of fluorophores and MR contrast agents. An illustration of a nanoparticle used in this thesis is shown in figure 2.1.

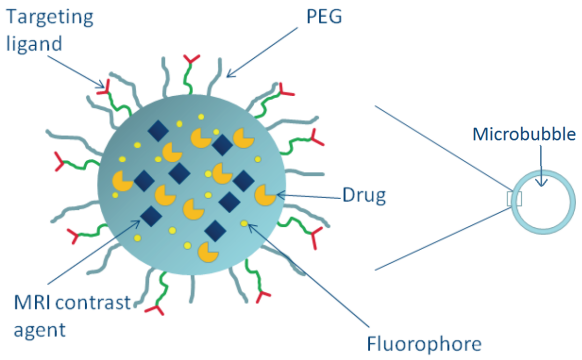


Figure 2.1: Schematic figure of a nanoparticle with fluorescent dye, MRI contrast agents, targeting ligands, drugs, a PEG-layer and a possible location of the nanoparticle in the shell of a microbubble. Adapted from a presentation of Yrr Mørch.

**Challenges and a new strategy**

The EPR effect can be used to passively target tumor tissues. However, the high interstitial pressure in the tumor limits the transport rate of nanoparticles to the cancer cells and a homogeneous delivery of drugs. It is also challenging to proper control drug release kinetics in the tumor. The use of ultrasound in combination with small micrometer-sized gas bubbles (microbubbles) has been proposed as a potential strategy to trigger the release of nanoparticles at an appropriate site and also to assist nanoparticles and drugs to overcome barriers in the tumor. The nanoparticles are then positioned in the interface between the gas and the surrounding liquid as shown in figure 2.1. Ultrasound and microbubbles are discussed in the following sections.

## 2.3 Ultrasound

Ultrasound is a term used for sound waves with frequency above the threshold for the human ear, around 20 kHz. High-frequency sound waves have a wide range of applications in different fields. Industrial usages include cleaning, mixing and sensor devices. In medical science, ultrasound is commonly used in diagnostic and imaging procedures and in non-invasive surgery. New promising therapeutic applications in drug delivery and gene therapy are under developing [16].

### 2.3.1 Ultrasound physics

Ultrasound is mechanical waves that propagate in a compressible medium. A vibrating source causes particles in the medium to displace, and regions form where the pressure and density are greater and less than the equilibrium values. These regions are formed in a fixed pattern, and the distance from one compression or rarefaction to the next is called the wavelength $\lambda$, as shown in figure 2.2. The particles oscillate parallel to the direction of the wave propagation with same period $T$ as the vibrating source. The frequency $f$ of the propagating wave is therefore equal to the frequency of the vibration, and the phase velocity $c$ is

$$c = \lambda f. \tag{2.1}$$

$c$ is called the speed of sound, and it varies in different mediums and with temperature. For water, $c \approx 1500$ m/s at 25 degrees [17]. The value is similar for soft tissues. The particle movement can also be perpendicular to the direction of wave propagation. This produces shear or transverse waves. In soft tissues, shear waves have a low phase velocity, are greatly attenuated and can thus be neglected [18].

If the sound source is a sinusoidally vibrating plane with frequency $f = 2\pi\omega$ and with dimensions of the plane larger than the wavelength, the generated acoustic pressure wave can be described as

$$p(x,t) = p_0 e^{-\alpha x} e^{i(\omega t - kx)}. \tag{2.2}$$

$p(x,t)$ is here the excess of the total pressure to the equilibrium pressure, $p_0$ is the amplitude at $x = 0$, and $k = \frac{2\pi}{\lambda}$ is the wave number. $\alpha$ is the attenuation coefficient and accounts for the transfer of energy from the wave to the medium, which mainly is through absorption and scattering processes. The attenuation coefficient is often measured in decibel per cm. The absorption is due to energy converted into heat because of frictional

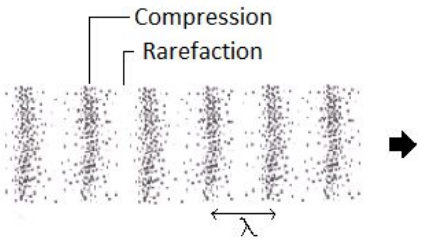


Figure 2.2: Schematic illustration of a longitudinal pressure wave. The particle movement is along the propagation direction of the wave. The wavelength $\lambda$ is indicated between two compression peaks.

forces that disrupt the periodic motion of the particles. Higher frequencies are shown to increase the absorption. Scattering is caused by inhomogeneities in the medium that is able to re-direct acoustic energy to areas outside the original propagation path. Water has low attenuation that can usually be neglected [19].

The pressure wave is accompanied by particle movements. When the pressure wave propagates in a medium, it exerts a force on the medium per unit volume that is equal to $\partial p(x,t)/\partial x$. As mass per unit volume is density $\rho$, Newton's second law follows with

$$\rho_0 \frac{\partial v(x,t)}{\partial t} = -\frac{\partial p(x,t)}{\partial x}. \tag{2.3}$$

$v(x,t)$ is here the velocity of the particles, which must not be confused with phase velocity of the wave.

The acoustic intensity represents the amount of work the traveling pressure wave does on the medium per unit area during one period. It is given by the time average of the product of $p(x,t)$ and $v(x,t)$ over a period $T = 1/f$. For a plane non-focused acoustic wave with $\alpha$ negligibly small, the acoustic intensity $I(x)$ is

$$I(x) = I_0 e^{-2\alpha x}, \tag{2.4}$$

where $I_0 = \frac{p_0^2}{2\rho c}$ is the intensity at $x = 0$ [19].

The ultrasound wave can be delivered continuously or in series of pulse repetition periods. When delivered in series, each period has a duration $T_0$ that must be longer than the period $T$ of a single cycle. This means that there are periods when ultrasound is transmitted ($T_t$) and when it is not ($T_0 - T_t$). The duty factor $DF$ is the fraction of time when the ultrasound is transmitted and is equal to $T_t/T_0$. The acoustic intensity is then reduced to $I_0 \cdot DF$ [11].

An ultrasound wave reflects and refracts when it passes an interface between two media. The result is a split of the wave. A refracted wave will continue in the new medium with a changed propagation angle, while a reflected wave will propagate in opposite direction in the initial medium. How the energy is shared between the two resulting waves is determined by the acoustic impedance of the media. The acoustic impedance $Z$ is defined as

$$Z = \rho \cdot c, \tag{2.5}$$

where $\rho$ is density of the medium and $c$ is the phase velocity of the wave. The fraction of energy possessed by the reflected wave is then

$$R = \left( \frac{Z_1 - Z_2}{Z_1 + Z_2} \right)^2, \tag{2.6}$$

where $Z_1$ and $Z_2$ is the impedance of the first and the second medium, respectively [18].

### 2.3.2 Transducers and beams

An ultrasound transducer is normally made of a plate of piezoelectric material with metal electrodes on each side. When voltage is applied between the electrodes, the material increases or decreases its thickness depending on the polarity of the voltage. An oscillating voltage source connected to the electrodes results in vibration of the plate thickness. If the transducer is in contact with a medium, e.g water or soft tissue, the medium will start to vibrate, and an ultrasound wave is created. In addition, the transducer can also receive ultrasound waves. An incoming wave makes the plate vibrate, and the piezoelectric effect generates a varying voltage between the electrodes that can be recorded as a signal [18].

The transducer tends to ring for some oscillations after the voltage source is removed. This ring-down is due to resonance in the thickness vibration, and it limits the minimum length of the ultrasound pulse. The ringing can be reduced by, e.g., using a thin plate between the transducer and the medium with a thickness of quarter of a wavelength and a stiffness that is between the stiffness of the plate and the tissue. The width of the distribution of frequencies in the pulse, the bandwidth, is inversely proportional to the pulse length. A large bandwidth requires a short pulse length [18].

#### Unfocused transducers

Ultrasound transducers can either be focused or unfocused. An unfocused transducer has a flat surface. The radiated beam from the transducer plate is generally divided into three regions, but with smooth transitions. In the farfield region, the beam expands with a fixed angle because of diffraction. The amplitude decreases as the distance to the central axis increases. The beam is said to be composed of side lobes surrounding a central main lobe, where the width of the main lobe can be defined where the amplitude has fallen with 12 dB from the central axis. A schematic figure of the ultrasound beam of a flat transducer is shown in figure 2.3.

The angle defining the expansion of the farfield region is found from

$$\Theta_{12dB} = k_{12dB} \frac{\lambda}{D}, \tag{2.7}$$

where $\lambda$ is the wavelength and $D$ is the transducer diameter. $k_{12dB} = 2$ is a number that accounts for the definition of the width.

The distance $z$ from the transducer surface to the farfield region for a plane and circular transducer is

$$z = \frac{D^2}{2\lambda}. \tag{2.8}$$

The shape of the farfield side lobes is dependent on the transmitted pulse length. Continuous waves cause the side lobes to appear with directions of zero amplitude, while with short pulsed waves, the zeros disappear.

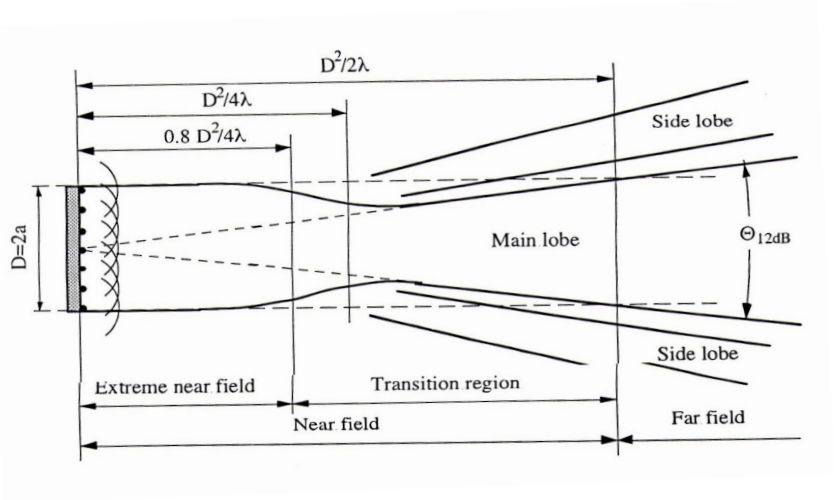


Figure 2.3: Schematic figure illustrating an ultrasonic beam from a flat transducer. The beam has a characteristic expanding farfield region composed of side lobes surrounding a main lobe. The nearfield consists of the extreme nearfield region with beam diameter at the size of the transducer diameter, and the transition region where the beam has a typical narrowing [18].

The extreme nearfield is defined where the beam has approximately equal diameter as the transducer and is found at distance $z < 0.4D^2/2\lambda$. The transition region is located between the extreme nearfield and the farfield. The characteristics of the transition region is that the beam tends to narrow before expanding in the farfield. This apparent focusing is called diffraction focusing [18].

#### Focused transducers

Focused transducers have a shape that represents a part of a spherical shell. An ultrasound beam of a focused transducer is shown in figure 2.4. While the geometrical focus is in the center of curvature of the spherical shell, the actual focus is slurred because of diffraction. For a focused transducer with diameter $D$ and radius of curvature $F$, the focal diameter becomes

$$D_F(12dB) = k_{12dB}\frac{\lambda}{D}F. \tag{2.9}$$

The width is here defined where the amplitude is reduced with 12 dB, and $k_{12dB}$ is the same as in equation 2.7.

The depth of focus is the length in the direction perpendicular to the transducer surface (z-direction) of the region where the amplitude of the beam is within X dB of the maximum amplitude around the focus. If X=1, the focal depth is $L_F(1dB) \approx 4\lambda(F/D)^2$ [18].

### 2.3.3 Imaging and contrast agents

Ultrasound imaging is a commonly used technique for a variety of medical investigations because of its low-cost and non-invasivness and accounts for up to 25 percent of all imaging worldwide [11]. The typically used frequency range is 2-10 MHz [18]. For intra-arterial imaging, frequencies up to 40 MHz is applied. Higher frequency gives better resolution,

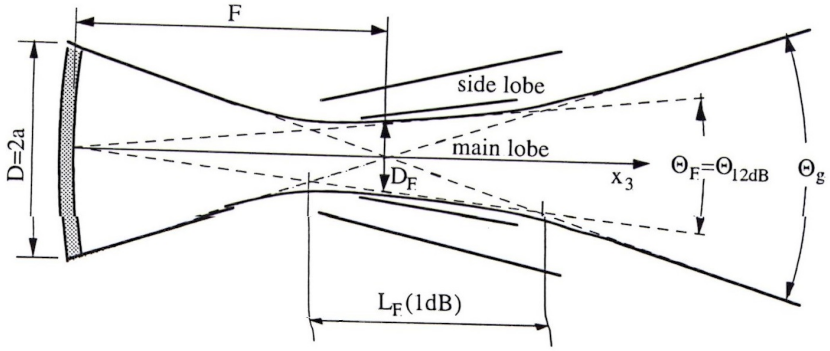


Figure 2.4: Schematic illustration of a focused beam with the transducer shaped as a part of a spherical shell. The focal diameter $D_F$ is indicated.

but increases at the same time the attenuation. The image is formed by scattering and reflection of the sound waves from inhomogeneities in the tissue. The echoes are interpreted in the scanner and used to form an image [18].

The signals returned from the tissue do not only contain the transmit frequency, but can also have other frequencies. Most important is the second harmonic at twice the transmit frequency. In harmonic imaging, the second harmonic component of the received echo is filtered out and used to form the image. The advantage of harmonic imaging include better spatial and contrast resolution, while a drawback is the low bandwidth required to prevent overlap of the fundamental and the harmonic.

A different harmonic imaging technique is called pulse inversion imaging. Instead of one pulse, two pulses with opposite signs of the amplitude are transmitted. The echoes of the pulses will be added, and the image is formed by the summed signal. If the target responds linearly, the received signal is canceled out. On the other hand, second harmonic components will add and give a received signal at twice the transmit frequency, whereas the fundamental is canceled. [20].

Harmonic imaging is beneficial and provides enhanced contrast if target tissue responds more non-linearly than surrounding tissue. A method of increasing the contrast is to inject ultrasound contrast agents. Such agents radiate generally larger amount of harmonics than tissue when exposed to ultrasound, and they are thus more easily perceived by harmonic imaging. The main purpose of ultrasound contrast agents is to increase the scatter of ultrasound from the blood. Normally, blood is a weak ultrasound scatter. Enhancing the contrast of the blood yields more information about the cardiovascular system, including vessels and the heart ventricles, that can simplify diagnosis. The ability of a contrast agent to scatter sound efficiently depends on its compressibility. In addition, a potential contrast agent must be smaller than 10 μm to pass through capillaries and should be larger than 1 μm to be confined to the circulatory system. Furthermore, the contrast agent has to be stable enough in the blood, so that organs of interest can be reached. But at the same time, it needs to be removed or degraded at an appropriate rate to avoid accumulation in the body [21, 22].

## 2.4 Microbubbles, ultrasound and drug delivery

### 2.4.1 Microbubbles

Microbubbles are currently the most attractive ultrasound contrast agent and have been in clinical use for more than two decades. Microbubbles are small gas bubbles with diameter 1-10 μm. Because of the gas core, microbubbles are highly compressible and scatter ultrasound waves efficiently compared to surrounding tissue and liquid. In addition, when microbubbles are driven at their resonance frequency, they have a strong increase in the scattering cross-section [23]. The resonant frequencies are normally within the same range as frequencies used in medical ultrasound imaging. Besides, microbubbles have shown promising effects when employed in drug delivery.

#### Evolution of microbubbles

Gas bubbles ability to act as ultrasound contrast agents was demonstrated in the 1968 by Gramiak and Shah [24]. It was shown that ultrasound backscattering greatly increased with addition of gas bubbles. This initiated the era of ultrasound contrast agents. However the first developed microbubbles were large and unstable, and they could not pass the capillaries and disappeared after only a few seconds [21]. The surface tension $\sigma$ of an uncoated gas bubble at micrometer-size is very large and causes the bubble to rapidly dissolve. The pressure difference across the bubble surface is known to be

$$\Delta p = \frac{2\sigma}{R}. \tag{2.10}$$

With a radius $R$ of the bubble less than 10 μm, $\Delta p$ becomes more than 0.1 MPa. It was therefore necessary to find methods to reduce or counter the effect of the surface tension.

It was soon discovered that human serum proteins could prolong circulation time of the gas bubbles. In 1994, the commercially available human albumin coated contrast agent Albunex (Molecular Biosystems, San Diego, CA) became approved for clinical use. Albumin improves the stability of the bubble by forming an elastic shell around the gas core that counters the effect of the surface tension [25].

More stable microbubbles were developed which replaced the air in the gas core with inert gases with higher molecular mass. E.g., Optison (GE Healthcare) contains octafluoropropan and a shell of albumin, and SonoVue (Bracco) has a core of hexafluoride and a coating of phospholipids. The advantages of using these types of gases are that they diffuse slower and are less soluble in blood, thus their stability is enhanced. Phospholipids work as surfactants and reduce the surface tension. Microbubbles with phospholipid coating are more flexible than albumin coated bubbles and can vibrate with larger amplitudes without cracking [25]. Phospholipid coated bubbles have therefore the last decade received most attention, but microbubbles coated with polymers and other surfactants and proteins are currently under development. Moreover, microbubbles are being tested for further functionalities.

#### Targeted and therapeutic microbubbles

Microbubbles can be used in molecular imaging to achieve enhanced contrast of specific tissues and cells during ultrasound imaging. This can be achieved by adding ligands to the microbubble surface that can recognize and bind to receptors of specific cells in targeted organs [25, 26].

Drugs can be attached to the microbubble by intermolecular forces, physical encapsulation or in a secondary carrier associated to the microbubble [21]. The microbubble acts as a drug carrier and restricts the medicine to leave blood vessels and affect normal cells. In contrast to free nanoparticles, microbubbles are confined to the circulatory system. Yet, the microbubbles have an advantage as a drug delivery vehicle because they are easily traced throughout the body by using low-intensity ultrasound. And furthermore, the drugs can be released by destroying the bubbles with high-intensity ultrasound at an appropriate target site. Physical phenomena associated with microbubbles oscillating in ultrasound field can also increase the transport rate of drugs in the interstitial tissue and enhance uptake of drugs by cells [27]. In this thesis, there is used a microbubble structure where drug-loaded nanoparticles are positioned in the interface between the gas and the liquid.

### 2.4.2 Physics of microbubbles in acoustic fields

#### Linear oscillation

Because of the high compressibility of microbubbles with respect to the surrounding aqueous medium, several responses are elicited when microbubbles are subjected to an acoustic field. In essence, an ultrasound wave causes microbubbles to oscillate; the bubble expands at low pressure, and contracts at high pressure. When the pressure amplitudes of the wave is low, the microbubbles oscillate with amplitudes small compared to the equilibrium radius. This is within the linear regime as the applied pressure relates linearly to the resulting bubble vibration. A linear oscillation is shown in figure 2.5a (left). The oscillations are stable, symmetric and with same frequency as the incident wave [27].

#### Nucleation

Ultrasound does not only affect already produced microbubbles, but can also initiate the production of new bubbles in the process of cavitation nucleation. When the pressure falls during the rarefaction phase, the solubility of gases solved in a liquid reduces. This can draw gas out of the liquid and form bubbles. In addition, if the temperature rises and the pressure falls under the vapor pressure, vapor bubbles can be formed. If the availability of surfactants and proteins in the liquid is limited, the life-time of these bubbles are generally low [23].

#### Non-linear oscillation

As the acoustic pressure is increased, a microbubble present in the acoustic field will oscillate with larger amplitudes. At some point, the bubble responds non-linearly. The amplitude at which non-linear effects occur, depends on the size, shell properties and materials. For example, microbubbles coated with phospholipids are observed to exhibit non-linear behavior at smaller amplitudes than polymer-coated bubbles [28, 29]. For a bubble population, the transition therefore appears gradually, as more and more bubbles are in the non-linear regime. Typical behaviors are non-spherical and non-symmetrical oscillations, e.g., expansions can be more pronounced than compressions [23]. In addition, the excitation frequency that results in maximum amplitude can become dependent on pressure, and the interactions between microbubbles and the surrounding medium and between each other become more important [27]. Importantly, the frequency spectrum of

the re-radiated acoustic field from the microbubble contains frequencies not only equal to the frequency $f_i$ of the transmitted ultrasound, but also at multiples and fractions of $f_i$, so-called harmonics [22]. Frequencies that are smaller than the transmitted frequency are called sub-harmonics, i.e., $1/2f_i$, $1/4f_i$, etc., while frequencies larger than $f_i$, but not multiplied by integers, are called ultra-harmonics, e.g. $3/2f_i$,$5/2f_i$ etc. The second harmonic is the most pronounced harmonic and can be observed at twice the transmit frequency. A non-linear oscillation and a typical frequency spectrum with higher harmonics are shown in figure 2.5a (right).

### Stable cavitation

When the microbubble is observed to respond with relatively large amplitudes, and often non-linear, yet stable oscillations, the behavior is called non-inertial or stable cavitation [30]. Figure 2.5b illustrates a characteristic stable cavitation with the associated frequency spectrum. The oscillations are controlled by a balance between the pressure of the core gas and the inertia of the surrounding liquid. Vibration of the microbubble-surface generates circulation of fluids and local swirling in the vicinity of the bubble. The phenomenon is called microstreaming and can be exploited in therapeutic applications, as described below. The bubbles avoid to dissolve and can continue to grow because of a process called rectified diffusion, where more vapors and gas diffuse into the bubbles during low pressure than the amount that diffuse out during elevated pressure [30].

### Inertial cavitation and bubble destruction

By further increasing the acoustic pressure, the oscillation amplitudes will grow. Eventually, the outward expansion will exceed a threshold. The pressure inside the bubble will become so low that it cannot support the inertia of the liquid, and the bubble will collapse abruptly and violently [23, 30]. The collapse may increase temperature and pressure locally. 5000 K temperature and 1000 atm pressure have been observed, but only confined to the center of the bubble [31]. The result is usually a breakage of the bubble into small fragments, which can undergo rectified diffusion, grow and eventually can collapse. During inertial cavitation and destruction, the energy of the radiated acoustic field from the microbubbles are distributed across a wide range of frequencies, as indicated in figure 2.5b (right). This leads to elevated noise level [23].

The likelihood that a inertial cavitation occurs depends on bubble size, shell properties and materials, and frequency. Generally, inertial cavitation happens more frequently at lower frequencies. The Mechanical Index (MI) accounts for the probability of inertial cavitation in a medium exposed to ultrasound with maximum negative pressure $p_{neg}$ in MPa and frequency $f$ in MHz,

$$MI = \frac{p_{neg}}{\sqrt{f}}. \tag{2.11}$$

For MI higher than 0.7, the probability of inertial cavitation is very high [30].

The acoustic destruction of microbubbles is applied in imaging techniques. For example, it can be used to quantify tissue perfusion and flow velocity by measuring the rate at which new bubbles are replenishing an image after initially destroying the bubbles with high-pressure ultrasound [32]. Destruction of microbubbles does not only occur due to large amplitude oscillation, but can also be caused by damage to the shell encapsulating the bubble and subsequent release of the trapped gas [22].

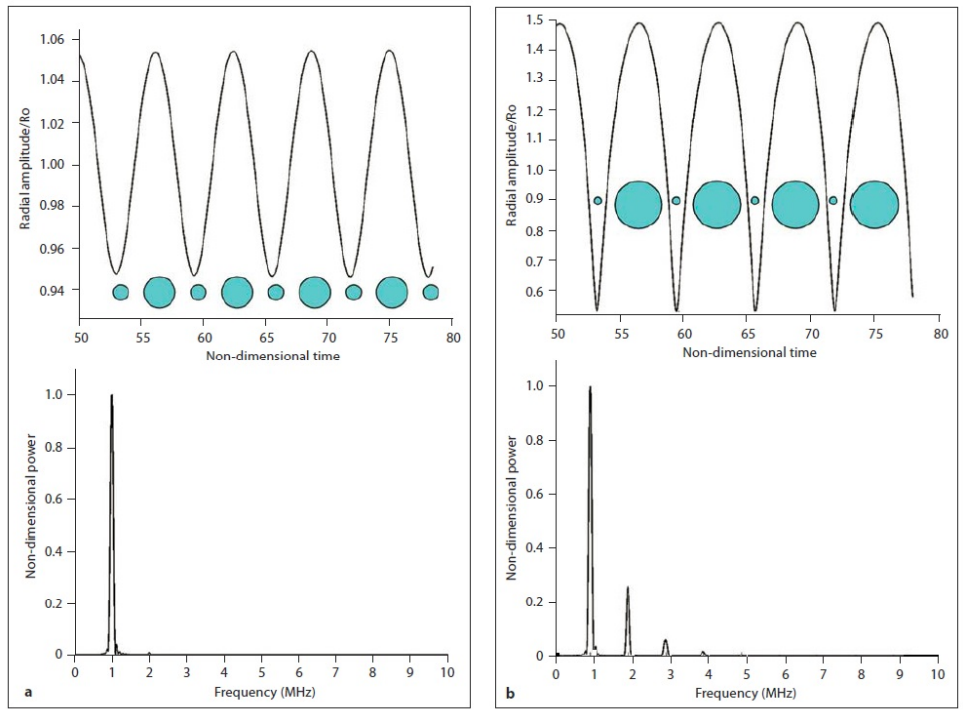


(a)

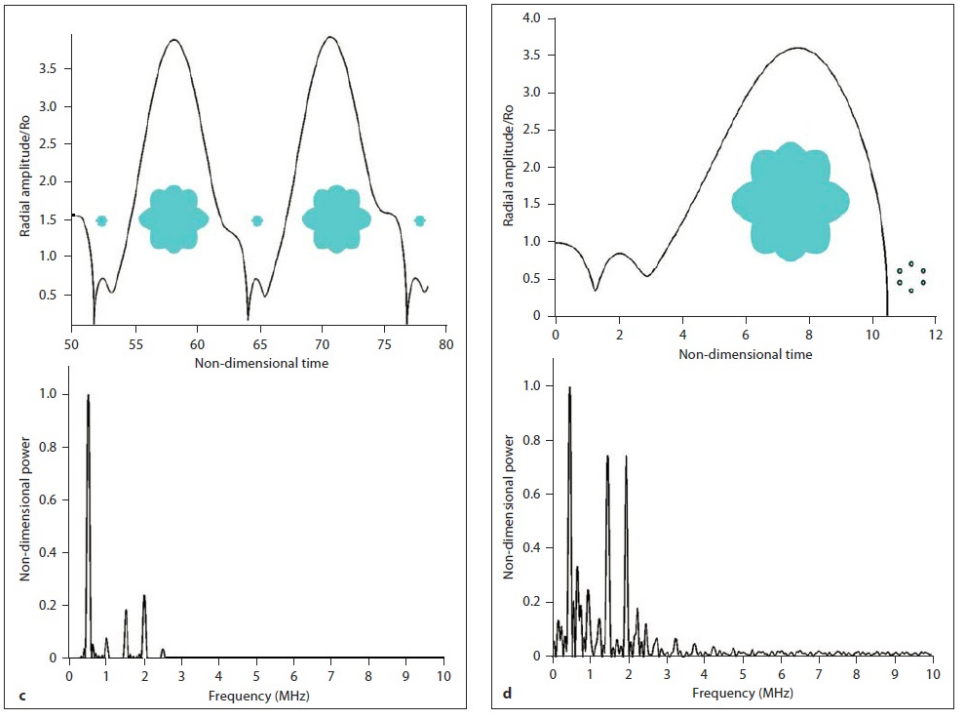


(b)

Figure 2.5: Figure showing different oscillation regimes: a) (left) linear oscillation, a) (right) non-linear oscillation, b) (left) stable caviation, b) (right) inertial cavitation. The upper graphs show how the relative radial amplitude oscillation differ between the regimes, and the lower part contains typical frequency spectra for the respective oscillation [23].

### 2.4.3 Effects of ultrasound on microbubbles with applications in drug delivery

Microbubbles intravenously injected into the body will be distributed in the circulatory system. Ultrasound can then be focused into the target tissue and release responses

that have been shown can improve drug delivery [33, 11]. Phenomena exhibited by microbubbles in ultrasound field can explain the enhanced delivery, still, the mechanisms are currently not fully understood.

### Cavitation

The effects that probably have most impact on drug delivery are those that are due to cavitation. The microstreaming effect produced by stable oscillating microbubbles gives rise to swirling and circulating flows that can impose large shear stresses. A cell membrane adjacent to a bubble can be damaged or be more permeable to therapeutic drugs. The process of creating transient pores in the cell membrane is called sonoporation, and the pores can facilitate influx of drugs into the cell and across capillary walls. Microstreaming can also assist drugs or nanoparticles that have been released by the microbubble to reach target cells more rapidly than diffusion [33, 11].

An inertial cavitation and collapse is important since it releases drugs or nanoparticles attached to the bubble. In addition, the energy can be released as a shock wave that can damage surrounding tissue and increase transport rate of the drugs and nanoparticles. If the collapse occurs near a rigid surface, asymmetry in the motion of the liquid can cause the bubble to generate a microjet of fluid towards the surface. If the surface is a cell membrane of an endothelium cell in a capillary, the impact of the jet can be sufficient to pierce the membrane and lyse the cell [33]. The damage of a capillary wall may increase the extravasation of drugs. An overview of cavitation effects that can be exploited in drug delivery are found in figure 2.6.

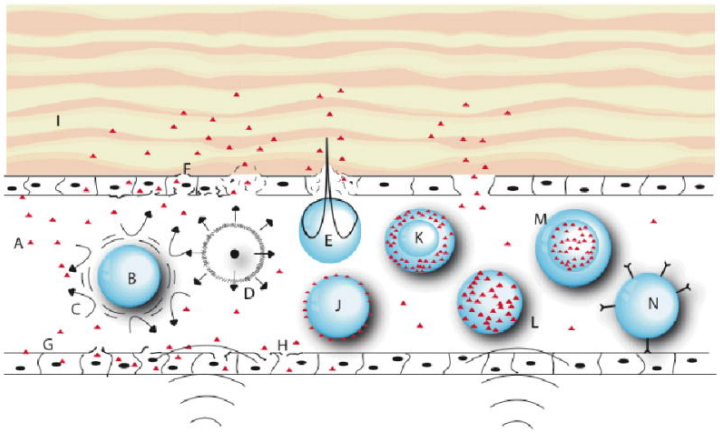


Figure 2.6: A schematic figure summarizing drug delivery related physical effects of ultrasound on microbubbles. (A) Released drugs or nanoparticles, (B) stable cavitation, (C) microstreaming, (D) inertial cavitation or collapse, (E) microjet penetrating an endothelial cell, (F) ruptured endothelial cell, (G) sonoporation, (H) damaged endothelial cell, (I) interstitial tissue, (J, K, L and M) different structures of microbubbles associated with drugs or secondary carriers, (N) microbubble with ligands that can attach to specific receptors [33].

### Acoustic radiation force

The momentum associated with a propagated wave can be transfered to the medium. This produces unidirectional movements of particles in the medium as if a force was acting on

them. The force is called the acoustic radiation force and results in streaming fluids that can increase drug transport rate [30]. Due to already high blood flows and small fluid reservoirs in the interstitium, the radiation force is maybe not an important effect [33].

#### Thermal effects

Absorbed energy from a propagated ultrasound wave in tissue causes hyperthermia. The percentage of energy that is absorbed from the wave increases with higher frequencies. Microbubbles can enhance the heating effect because they generate higher harmonics that are more easily absorbed, in addition, they dissipate energy as heat because of viscous processes. The higher temperature may damage tissue, activate drug delivery devices to release their substances and also reduce diffusion time of drugs in the interstitium [23]. Though, because of the continuous circulation of blood, thermal effects are thought to have limited function in ultrasound mediated drug delivery [33].

#### Chemical effects

Inertial cavitation results in large pressure and high temperature that is known to produce reactive chemical species, such as free radicals and hydrogen peroxide. These species can be harmful to cells and potentially increase permeability. For example, it has been shown that rat cardiomyoblast cells exhibited increased $Ca^{2+}$ influx after exposure to low-intensity ultrasound with SonoVue microbubbles [34]. Hydrogen peroxide was given the responsibility for the cause.

## 2.5 Bubble models

Bubble models are theoretical descriptions of an oscillating bubble. A model that correctly predicts the responses of a bubble to an acoustic field, provides valuable understanding, is helpful in the development of new contrast agents, and can lead to discovery of novel applications.

### 2.5.1 Linear bubble models

#### Rayleigh scatter model

Microbubbles are used as contrast agents because of their ability to scatter sound. Rayleigh developed a model that describes the scatter of sounds from objects much smaller than the wavelength, $\lambda$ [35]. Even though the model fails to predict microbubble responses, including resonance frequency and attenuation, it provides understanding of why bubbles scatter efficiently. Based on the model, an expression is found for the scattering cross section of a particle with radius $R$ and density $\rho$ embedded in a liquid with density $\rho_l$,

$$\sigma_s = 4\pi R^2 (KR)^4 \left( \left( \frac{K - K_l}{3K} \right)^2 + \frac{1}{3} \left( \frac{\rho - \rho_l}{2\rho + \rho_0} \right)^2 \right). \tag{2.12}$$

$k = 2\pi/\lambda$ is the wave number, and $K$ and $K_l$ are the bulk moduli of the particle and the liquid. The bulk modulus represents the volume stiffness of a material and is given by,

$$K = -V \frac{\Delta p}{\Delta V}, \tag{2.13}$$

where $\Delta V$ is the change is volume and $\Delta p$ is the change in pressure. The bulk modulus is large for materials where large pressure differences are necessary to change the volume. These materials have a low compressibilty. On the other side, if the bulk modulus is small, the material is highly compressible. E.g., gases have $K$ in the range of 4 - 6 orders of magnitude lower than liquids and solids [22]. Equation 2.12 shows that objects scatter strongly if $K \ll K_l$. This is true for gas-filled bubbles in fluids.

Another consequence Rayleigh's scatter model, is the existence of monopole and dipole scatter. When the bulk modulus differs between the particle and the surrounding medium, the particle in the sound field will oscillate in volume and radiate spherically symmetric. This is called monopole scatter. A difference between the density of the particle and the surrounding medium causes the particle to oscillate back and forth. This produces dipole scatter, and the direction of the radiation is perpendicular to the translatory motion of the particle [22].

### Linear oscillator

A different model is needed for prediction of the resonance frequency. Inspired by a mechanical oscillator with mass $m$, spring constant $s$ and damping $\zeta$, a harmonic oscillator model of the bubble can be developed with equation of motion for the oscillation written as,

$$m\ddot{R} + \zeta\dot{R} + sR = -4\pi R_0^2 p_i(t), \tag{2.14}$$

where $\dot{R}$ denotes the time derivative of $R$; $R_0$ is the equilibrium radius of the bubble; and $p_i(t)$ is the driving acoustic pressure. Because this is a linear model, it requires that the oscillation amplitude is small relative to the equilibrium radius. Only spherical bubbles are considered.

The oscillating bubble sets the surrounding liquid in motion, which gives rise to the inertia of the system. It can be shown that the effective mass of the oscillating bubble is $m = 4\pi R_0^3 \rho_l$, where $\rho_l$ is the density of the liquid. Similarly, the effective spring constant of the bubble depends on the gas pressure in the bubble. Using the polytropic gas law $pV^\kappa = constant$, and looking at the difference between the bubble surface pressure and the equilibrium pressure inside the bubble $p_{0g}$, it can further be shown that $s = 12\pi\kappa R_0 p_{0g}$. The effect of surface tension or a bubble shell is yet not included. The oscillation amplitude reduces with time due to various damping mechanisms: Viscosity of the liquid, thermal conduction between the gas and the liquid, and lose of energy as the bubble radiates. An estimation and discussion of damping is found in [22]. Simulation shows that the damping caused by liquid viscosity dominates for 1 μm diameter bubbles up to 50 MHz. For 5 μm diameter, viscous damping dominates at low frequency, while radiation damping becomes most important at frequencies above 3 MHz.

The effective spring constant and mass are sufficient to estimate the resonance frequency $f_0$ for a free bubble,

$$f_0 = \frac{1}{2\pi}\sqrt{\frac{s}{m}} = \frac{1}{2\pi R_0}\sqrt{\frac{3\kappa p_{0g}}{\rho_l}}. \tag{2.15}$$

Minnaert was the first to study the bubble oscillator model, and $f_0$ is therefore also called the Minnaert frequency [36].

For air-filled bubbles in water at standard pressures, $p_{0g}$ is approximately 100 kPa and $\rho_l = 1000$ kg/m$^3$. The value of $\kappa$ is in acoustics generally assumed to be the adiabatic gas

constant $\gamma$ ($\approx 1.4$ for air) because high frequency compression is regarded as adiabatic, that is, no heat transport is happening. However, at lower frequency, the heat transport is rapid enough to maintain a constant temperature in the bubble, and the oscillation is isothermal with $\kappa = 1$. At the intermediate frequency range, the value is between $\gamma$ and 1. What is a high and low frequencies depends on the bubble size.

### 2.5.2 Nonlinear bubble models

The linear bubble oscillation model does not hold when the amplitude becomes large. Several models have been developed that try predict the non-linear responses observed during bubble oscillation. Some important models are presented here.

#### Rayleigh-Plesset equation

The simplest non-linear equation of motion for a gas bubble is the Rayleigh-Plesset equation. In this model, the bubble is assumed to be spherical and surrounded by incompressible liquid of infinite extent. The incompressibility means that the bubble wall velocity has to be small compared to the speed of sound. It also leads to no terms accounting for energy loss by acoustic radiation of the bubble. This is satisfactory as long as the viscosity damping in the liquid surpasses the radiation damping, which it normally does as the product of frequency and radius $f \cdot R$ is larger than $0.1 \cdot \frac{c}{2\pi}$ [22].

The following equation resulted from work of Lord Rayleigh in 1917, who studied bubbles formed around ship propellers [37], and by Plesset in 1949, who included a driving acoustic field [38]:

$$\rho_l \left( \ddot{R}R + \frac{3}{2}\dot{R}^2 \right) = p_l - p_0 - p_i(t). \tag{2.16}$$

$\rho_l$ is the density of the liquid; R is the radius of the bubble; $\dot{R}$ and $\ddot{R}$ denotes here the first and second time derivative respectively; $p_0$ is here the atmospheric pressure; $p_i(t)$ is the driving pressure field; and $p_l$ is the pressure of the liquid at the bubble surface.

Several modifications of this basic equation have been done. Noltingk, Neppiras and Protsky extended the equation to include the effects of surface tension, gas inside the bubble and liquid viscosity [39]. All extensions are done by substituting $p_L$. With the use of the polytropic gas law,

$$\rho_l \left( \ddot{R}R + \frac{3}{2}\dot{R}^2 \right) = \left( p_0 + \frac{2\sigma}{R_0} \right) \left( 1 - \frac{3\kappa}{c}\dot{R} \right) \left( \frac{R}{R_0} \right)^{-3\kappa} - \frac{2\sigma}{R} - \frac{4\mu_l \dot{R}}{R} - p_0 - p_i(t). \tag{2.17}$$

where $\kappa$ is the polytropic gas exponent; $\mu_l$ is the viscosity of the surrounding liquid; $c$ is the speed of sound; $\sigma$ is the surface tension; and $R_0$ is the equilibrium radius.

#### The Church model

Church derived an equation for the radial dynamics of a bubble with a stabilizing shell in response to an acoustic field [40]. $R_1(t)$ and $R_2(t)$ are the inner and outer radii of the bubble shell, respectively. At equilibrium, the radii are $R_{01}$ and $R_{02}$. The surrounding medium is assumed to be a Newtonian incompressible liquid of infinite extent with shear viscosity $\mu_l$. The bubbles are enclosed by a shell of solid, incompressible and viscoelastic

material with frequency independent shear modulus $G$ and viscosity $\mu_s$. The following equation was obtained:

$$R_1\ddot{R}_1\left[1+\left(\frac{\rho_l-\rho_s}{\rho_s}\right)\frac{R_1}{R_2}\right]+\dot{R}_1^2\left[\frac{3}{2}+\left(\frac{\rho_l-\rho_s}{\rho_s}\right)\left(\frac{4R_2^3-R_1^3}{2R_2^3}\right)\frac{R_1}{R_2}\right]$$
$$=\frac{1}{\rho_s}\left[p_{0g}\left(\frac{R_{01}}{R_1}\right)^{3\kappa}-\frac{2\sigma_1}{R_1}-\frac{2\sigma_2}{R_2}-4\mu_l\frac{R_1^2\dot{R}_1}{R_2^3}-p_0-p_i(t)-4G\frac{V_s}{R_2^3}\left(1-\frac{R_{01}}{R_1}\right)-4\mu_s\frac{\dot{R}_1V_s}{R_1R_2^3}\right], \tag{2.18}$$

where $V_s=R_{02}^3-R_{01}^3=R_2^3-R_1^3$ is the volume of the shell and is constant because the shell is incompressible; $\sigma_1$ and $\sigma_2$ are the surface tensions of the gas-shell and shell-liquid interfaces, respectively; $p_{0g}$ is the equilibrium pressure inside the bubble; $p_0$ is the pressure of the surrounding liquid and is assumed to be equal to the atmospheric pressure; $p_i(t)$ the driving acoustic pressure.

Equation 2.18 considers only explicitly the damping that arises from viscosity. To include acoustic radiation damping, terms that account for the compressibility of the surrounding liquid must be added.

It is assumed that the surface tensions $\sigma_1$ and $\sigma_2$ are reduced by the shell, and they are therefore neglected. Grishenkov et al [41] tested and concluded that the contributions from the surface tensions were negligible.

It is further assumed that the equilibrium pressure inside the bubble is equal to the pressure of the surrounding liquid $p_{0g}=p_0$. The driving acoustic pressure is supposed to be sinusoidal, $p_i(t)=p_a\sin(\omega t)$.

Eventually, the amplitude of the bubble movement is assumed to be small. This simplifies equation 2.18 into a form of a linear harmonic oscillator equation with some additional non-linear terms.

Only the coefficients of the linear terms are of interest here, and they are as follows:

$$\omega_0=\left[\frac{1}{\alpha\rho_sR_{01}^2}\left(3\kappa p_{0g}+\frac{4V_sG}{R_{02}^3}\right)\right]^{\frac{1}{2}}, \tag{2.19}$$

$$\delta=\frac{4}{\alpha\rho_sR_{01}^2R_{02}^3}(\mu_lR_{01}^3+\mu_sV_s), \tag{2.20}$$

$$\alpha=\left[1+\left(\frac{\rho_l-\rho_s}{\rho_s}\right)\frac{R_{01}}{R_{02}}\right]. \tag{2.21}$$

### Collective bubble oscillations

The above equations obtained by Church are derived for the radial dynamics of a single bubble. When suspended bubbles are located in an acoustic field and acting as ultrasound contrast agents, only the collective bubble oscillations are interesting.

Commander and Prosperetti [42] derived and expressed the dispersion of a pressure wave propagating through a suspension of gas bubbles with elastic shells as

$$\left(\frac{c}{c_m}\right)^2=1+\frac{4\pi c^2\rho_l}{\alpha\rho_s}\int_0^\infty\frac{R_{01}f(R_{01})}{\omega_0^2-\omega^2+i\delta\omega}\,\mathrm{d}R_{01}, \tag{2.22}$$

where $f(R_{01})\mathrm{dR}_{01}$ is the number of bubbles per unit volume with inner radius between $R_{01}$ and $R_{01}+\mathrm{dR}_{01}$; $i$ is $\sqrt{-1}$; and $\omega_0$, $\delta$ and $\alpha$ are found in equations 2.19 - 2.21. $c_m$ is

the complex phase velocity of the wave propagating through the bubble suspension, while $c$ is the phase velocity of a wave propagating in the same medium without bubbles. The dispersion relation was derived under assumption of bubbles oscillating with small amplitudes. Whereas the Church model only accounts for viscous damping, acoustic radiation damping and thermal damping have been included in equation 2.22. Furthermore, it is assumed that the volume occupied by the bubbles is small compared to the total volume. The fraction of occupied volume is given by

$$\beta = \frac{4}{3}\pi R_{02}^3 n, \tag{2.23}$$

where $R_{02}$ is the radius of a bubble and $n$ is the number of bubbles with the specific radius $R_{02}$ per unit volume. In the derivation, terms of order $\beta^2$ were neglected with respect to terms of order $\beta$.

The wave number in the suspension is $k_m = \omega/c_m$. The wavenumber in equation 2.2 can then be replaced by $k_m$, so that

$$p(x,t) = p_0 e^{-\alpha x} e^{i(\omega t - k_m x)}. \tag{2.24}$$

If the attenuation caused by the medium is negligible, $\alpha = 0$. By setting $c/c_m = ck_m/\omega = u - iv$, equation 2.24 becomes

$$p(x,t) = p_0 e^{i(\omega t - \frac{\omega(u-iv)}{c}x)} = p_0 e^{\left(-\frac{\omega v}{c}x\right)} e^{\left(i\omega\left(t-\frac{u}{c}x\right)\right)}. \tag{2.25}$$

The final term shows that the bubble suspension introduces attenuation given by $\omega v/c$. The corresponding phase velocity is $c/u$.

### The Hoff model

The Hoff model is based on the Church model, but uses a different approach to calculate the attenuation [22, 43]. The shell is assumed to be small, but finite. If $R_{02} = R_{01} + t$, where $t$ is the shell thickness at equilibrium, and $t \ll R_{02}$, equation 2.18 can be simplified to an equation in outer radius $R = R_2(t)$:

$$\begin{aligned}\rho_l\left(R\ddot{R} + \frac{3}{2}\dot{R}^2\right) = p_0\left(\left(\frac{R_0}{R}\right)^{3\kappa} - 1\right) - p_i(t) \\ - 4\mu_l\frac{\dot{R}}{R} - 12\mu_s\frac{tR_0^2}{R^3}\frac{\dot{R}}{R} - 12G_s\frac{tR_0^2}{R^3}\left(1 - \frac{R_0}{R}\right).\end{aligned} \tag{2.26}$$

The surface tension has been neglected, and the pressure in the gas is set equal the pressure in the surrounding liquid, $p_{0g} = p_0$. Moreover, if the bubbles oscillate linearly, an analytical solution can be obtained by setting $R(t) = R_0(1 + x(t))$, where $|x(t)| \ll 1$. The result is a linear equation on an equivalent form as equation 2.14, that can further be Fourier transformed, and an equation for the radial displacement $\hat{x}(\omega)$ in the frequency domain is found:

$$\hat{x}(\omega) = \frac{1}{\Omega^2 - 1 - i\Omega\delta}\frac{\hat{p_i}(\omega)}{\rho_l\omega_0^2 R_0^2}, \tag{2.27}$$

where $\Omega = \omega/\omega_0$,

$$\omega_0^2 = \frac{1}{\rho_l R_0^2}\left(3\kappa p_0 + 12 G_s \frac{t}{R_0}\right), \tag{2.28}$$

and

$$\delta = \frac{4\mu_l}{\omega_0 \rho_l R_0^2} + \frac{12\mu_s t}{\omega_0 \rho_l R_0^3}. \tag{2.29}$$

The attenuation caused by a single bubble in a liquid can be written in terms of an extinction cross section $\sigma_e$, which is given as

$$\sigma_e(R,\omega) = \frac{P_A(R,\omega)}{I_i(\omega)}. \tag{2.30}$$

$P_A(R,\omega)$ is the power absorbed by the bubble, and $I_i(\omega)$ is the intensity of an incoming ultrasound field and is equal to $I_i(\omega) = \frac{|p_i(\omega)|^2}{2\rho_l c}$. The absorbed power can be calculated, and the result is $P_A(R,\omega) = \frac{1}{2} m \omega_0 \omega R_0^2 \delta |\hat{x}(\omega)|^2$, with $\hat{x}(\omega)$ found in equation 2.27. Hence, the extinction cross section becomes

$$\sigma_e(R,\omega) = 4\pi R_0^2 \frac{c\delta}{R_0\omega_0} \frac{\Omega^2}{(1-\Omega^2)^2 + \Omega^2\delta^2}, \tag{2.31}$$

where $c$ is the speed of sound in the liquid.

Finally, the attenuation $\alpha_b$ caused by a bubble population can be calculated by integrating $\sigma_e$ from all individual bubbles,

$$\alpha_b(\omega) = 10\log_{10}(e)\int_0^\infty \sigma_e(R,\omega) f(R) \mathrm{d}R. \tag{2.32}$$

$\alpha_b$ is measured in dB per unit length. $f(R)$dR is the number of bubbles per unit volume with radius between $R$ and $R + \mathrm{dR}$.

The Hoff model is a simplification of Church model and should only be used for bubbles with small shell thickness [44].

## 2.6 Atomic force microscopy

Atomic force microscopy (AFM) is an instrument used for imaging, measuring and manipulation of matter at nanometer- and micrometer-scale. Forces down to piconewtons can be applied and measured, which allows studies of the mechanics of biological systems, biomolecules and other materials.

An AFM instrument consists of a cantilever, a piezoelectric scanner, a feedback system and a detector system. AFM is based on the principle that attractive and repulsive forces from a sample cause the cantilever to deflect towards and away from the sample, respectively. A typical behavior of a cantilever with a tip during approaching and retracting is shown in figure 2.7. The cantilever can have or not have a tip, and it can be rectangular or v-shaped. A sharp tip, with a radius of the end at the order of nanometers, is required when high lateral resolution is desired [45].

The position of the cantilever relative to the sample is controlled by a piezoelectric scanner. Piezoelectric materials expand and contract when exposed to an applied voltage, and its high performance allows for a positioning of the sample relative to the cantilever

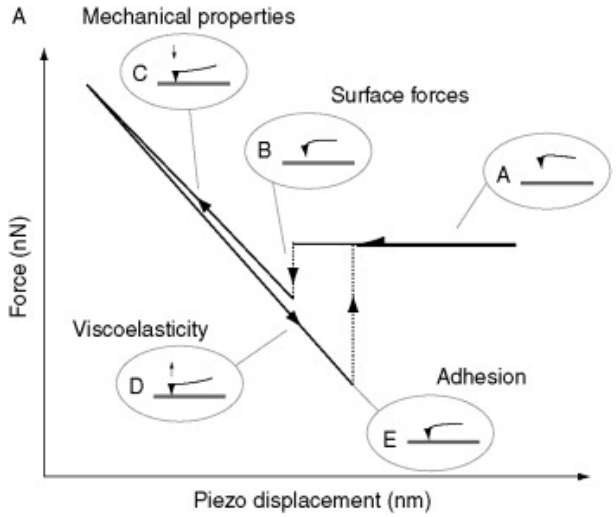


Figure 2.7: Typical force - displacement curve and the corresponding behavior of the cantilever during approaching and retracting. (A) cantilever approaches the surface, (B) attracting surface forces cause the cantilever tip to deflect, (C) when the cantilever tip is closer to the surface, repulsing forces cause the cantilever to deflect in the opposite direction. At the same time, if the surface material has lower Young's modulus $E$ than the cantilever tip, forces from the cantilever tip cause the surface material to deform, (D) viscous properties of the surface material results in a difference between the retracting curve and the approaching curve, (E) adhesion forces causes the cantilever to bend towards the surface. Adapted from [45, 46]

with resolution less than a nanometer. The scanner can operate decoupled in 3 dimensions, i.e., in x, y, and z-direction, by using independent electrodes in each direction [45]

The detector system comprises a laser and a photodiode. The laser beam points to the upper side of the cantilever, reflects and hits the photodiode. A deflection of the cantilever causes the laser to be reflected differently, and the position of the laser on the photodiode changes. This change of position, which is measured in volt, can be converted to deflection in nanometers by calibration of the cantilever sensitivity. In addition, the force causing the cantilever to bend is obtained from a measurement of the spring constant, $k$ of the cantilever. It is assumed that the cantilever follows Hooke's law and that the force is proportional to the deflection $d$, so that $F = d \cdot k$ [45]

A feedback system is used to obtain appropriate interaction between the sample and the cantilever. When used for imaging, different modes are possible. In contact mode, the tip is in contact with the surface, and repulsive forces are measured. Information about the topography of the sample is acquired as the tip is scanned across the sample. The feedback system can be ordered to keep the deflection of the cantilever constant. This is achieved by vertical movements of the piezoelectric scanner, and the movements yield topography information. A second feedback operation is to hold a constant height. The image will then result from the deflection. In the oscillating modes, the cantilever is set to oscillate near its resonance frequency. Forces from the surface of the sample on the tip will change the amplitude and frequency and give information about the surface characteristics. In tapping mode, the tip is partly in contact with the surface during the oscillation, while in non-contact mode, the tip is never in contact [45].

### Force measurements using AFM

When AFM is used to measure forces, the cantilever is moved vertically with respect to the sample. This is done by a ramping the piezoelectric scanner along the z-axis. The movements of the scanner and deflection of the cantilever yields force-distance curves. The speed of the scanner in z-direction is called loading rate, i.e., how fast the force is applied. Force-distance curves obtained at different loading rates can give information about binding kinetics and barriers between molecules. When a tipless cantilever is used to deform a sample, i.e., to compress it, the deformation $h$ of the sample is found by subtracting the cantilever deflection from the displacement of the piezoelectric scanner in z-direction $z$,

$$h = z - d. \tag{2.33}$$

Figure 2.8 shows a flat cantilever compressing a spherical sample. As the force acting on the cantilever is equal to the force acting on the sample (Newton's third law), the stiffness $k_s$ of the sample is found from

$$F = h \cdot k_s = d \cdot k, \tag{2.34}$$

which means that the $k_s$ is the gradient of a force-deformation curve [46].

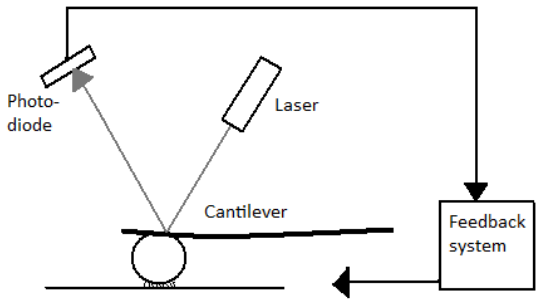


Figure 2.8: Schematic illustration of the principles of an AFM instrument with a tipless cantilever. The laser beam on the photodiode changes position when the cantilever deflects. The voltage from the photodiode can be converted to deflection in nanometer and used as an input in the feedback system [46].

## 2.7 Elastic compression theory

### Elasticity

A force exerted on a material can lead to deformation of the material. The relation between the force $F$ and the deformation $d$ is characteristic for the material. If the material is Hookean, the relation is expressed by the spring constant or stiffness:

$$F = k \cdot d. \tag{2.35}$$

Applied force per area is called stress $\sigma$, and deformation divided by the length of the material in the direction of applied force is called relative deformation or strain $\epsilon$. For a linear elastic material, the stress is proportional to the strain, and the relation is given by the material specific Young's modulus $E$:

$$\sigma = E\epsilon. \tag{2.36}$$

The linear relation is only valid for small deformations and forces and at short time scales. For an elastic material, the strain caused by the applied stress reverses when the stress is halted. A non-reversible deformation is referred to as plastic [17, 46].

Measurements of the Young's modulus of a sample material requires a system that can apply a known force and record the deformation. Because of mutual exertion of forces, the material compressing the sample material will also be deformed. The measured Young's modulus $E^*$ is thus reduced to

$$\frac{1}{E^*} = \frac{1-\nu_1^2}{E_1} + \frac{1-\nu_2^2}{E_2}, \tag{2.37}$$

where $E_1$ and $E_2$ are the Young's moduli of two materials [47]. $\nu_1$ and $\nu_2$ are the Poisson's ratios of the materials. A medium compressed in one direction will expand in the directions perpendicular to the direction of applied force. The ratio between strain in the compressed direction and the strain in axial direction is the Poisson's ratio. Most materials have a value between 0 and 0.5. Rubber has a value around 0.5, steel 0.29, polystyrene, 0.34 and lead 0.44 [48].

If a cantilever with Young's modulus $E_2$ is used to compress a microbubble with Young's modulus $E_1$, and $E_1 \ll E_2$, the second term in equation 2.37 can be neglected [46].

### Shear modulus

The shear modulus is an elasticity coefficient for a shearing force and is defined as the ratio of the shear stress to the shear strain [17]. If a force $F$ is applied parallel to a surface with area $A$ of a solid material, and an opposing force is acting on the opposite face, and the faces are separated by a distance $l$, the material will deform a length $\Delta x$. The shear modulus is then given by,

$$G = \frac{F/A}{\Delta x/l}. \tag{2.38}$$

The shear modulus of a microbubble shell is needed in bubble models used to calculate theoretical attenuation coefficients. For a homogeneous isotropic material, the relationship between the Young's modulus and the shear modulus is [17],

$$G = \frac{E}{2(1+\nu)}. \tag{2.39}$$

### Reissner theory

Because of the more complex geometry of the microbubble shell, equation 2.36 gives inaccurate estimation of the Young's modulus. Reissner derived and published in 1946 an analytical relationship between the force and relative deformation of a thin-shelled hollow microsphere that takes account of the geometric and material properties [49, 50, 46]. For a hollow microsphere with radius $R$, shell thickness $t$, Poisson's ratio $\nu$, force $F$ and relative deformation $\epsilon$, the Young's modulus is estimated to be

$$E = \frac{\sqrt{3(1-\nu^2)}}{8t^2}\frac{F}{\epsilon}. \tag{2.40}$$

During the derivation of the equation, the shell is assumed to be thin, elastic and isotropic, that is, uniform in all directions. The ratio of shell thickness to radius should be less than 1/20 [51]. Furthermore, the force is assumed to be applied point-like on the poles. Elsner *et al.* used finite element modeling to study how a large contact area and non-point-like forces influence the estimation of Young's modulus of polymeric shells. When compared with the Reissner theory, it was shown that the deviations between the two methods were insignificant at small deformations [52]. The Reissner theory has been applied by Glynos *et al.* for polymer microbubbles at the initial linear part of the force-deformation curve and was shown to be a good approximation [53, 51]. Though, when used for phospholipid microbubbles, the theory produced overestimations [54].

Fery *et al.* claim that Reissner theory only can be used for relative deformations up to a critical deformation $\epsilon_{crossover}$, which refers to a crossover from a linear deformation regime to a volume-constraint-dominated regime [55]:

$$\epsilon_{crossover} \approx \sqrt{\frac{t}{4\pi R}}. \tag{2.41}$$

# Chapter 3

# Materials and Methods

## 3.1 Nanoparticles and microbubbles

The nanoparticles and the microbubbles used in this work were synthesized and provided by SINTEF Materials and Chemistry. Two different nanoparticle batches are used in this thesis; the YM-44 and YM-73 nanoparticles.

The nanoparticles have been characterized by SINTEF. YM-44 nanoparticles have an average size 153 nm, which is measured by dynamic light scattering. The PDI is 0.08, and the zeta-potential is -19mV. PDI (Polydispersity Index) gives information about the size distribution. The zeta-potential is defined as the electric potential between a stationary layer of fluid attached to the nanoparticle and the dispersion medium. It represents the degree of repulsion between the particles.

YM-73 nanoparticles have an average diameter 153 nm, PDI 0.11 and zeta-potenital -15 mV.

The nanoparticles are produced by miniemulsion polymerization. A solution of a surfactant (sodium dodecyl sulfate) dissolved in 0.1 M HCl is mixed with the monomer phase (oil phase) containing the butyl-2-cyanoacrylate (BCA) monomer, a co-stabilizer and the fluorophores Nile Red and DiR. For the YM-44 batch, a crosslinker (EGDMA) and initiator (V65) is also added to the oil-phase. The only difference between the two batches is that YM-44 is crosslinked and YM-73 is not. The crosslinking prevents the nanoparticles from dissolving. The oil-in-water dispersion is then sonicated to form a nanoemulsion. The polymerization of BCA into poly(butyl cyanoacrylate) (PBCA) is initiated by adding the nanoemulsion mixture to a solution containing Jeffamine M-1000. Jeffamin M-1000 is a polyetheramine with approximately 20 ethylene oxide units and works both as a PEG and as an initiator. The nanodroplets polymerize at the interface between the two phases and forms nanocapsules. For the YM-44 batch, the crosslinking polymers also make a solid nanoparticle core. PBCA is biocompatible and biodegradable by bioerosion. The principles of the production are shown in figure 3.1.

Microbubbles are made with a shell of stabilizing nanoparticles. However, nanoparticles alone are not sufficient to give stable microbubbles, and a protein has to be added. The experimental work of this thesis involves use of microbubble with different sizes, nanoparticles and surfactant proteins. Bovine Serum Albumin (BSA) and casein are used as proteins. Casein is a common protein in mammalian milk.

A PBCA nanoparticle dispersion is mixed with the protein and water. An Ultra-Turrax (UT) is used to form air-filled microbubbles. The nanoparticles are positioning at

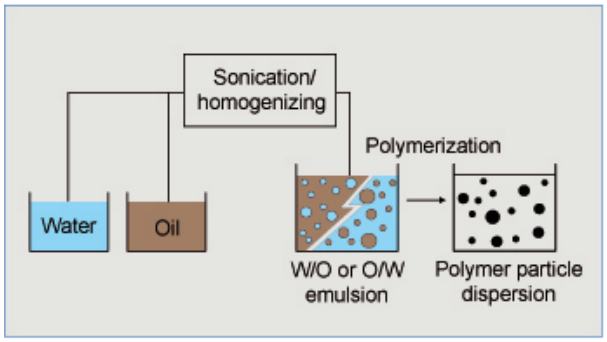


Figure 3.1: Illustration showing principles of nanoparticle production. Adapted from a presentation by Yrr Mørch.

the water-air interface, as illustrated in figure 3.2. The speed of the UT determines the average diameter of the microbubbles.

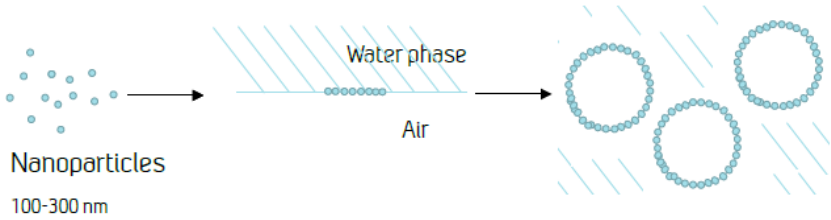


Figure 3.2: Illustration of the principles for making the microbubbles stabilized by nanoparticles. Adapted from a presentation by Yrr Mørch.

The microbubbles with the YM-44 batch were made with BSA and UT velocity 13500 rpm.

For the microbubbles with YM-73 and BSA, two different UT velocities were used. To make "large" microbubbles, 8000 rpm was used, and 24000 rpm was used to make "small" microbubbles.

The microbubbles with YM-73 batch and casein were made with UT velocity 16000 rpm.

Microbubbles stabilized by casein are observed to be larger and more spherical than those stabilized by BSA. The concentration of protein that resulted in highest concentration of microbubbles is 0.1 wt% for casein, and 0.5-1.0 wt% for BSA. This means that as less as 1/10 of the amount of protein is necessary when casein is used compared to BSA. Images of the microbubbles produced at different concentrations of proteins are acquired by SINTEF and shown in figure 3.3.

A commercial HEPS-Na/PFB microbubble is provided and analyzed in this thesis for comparison with the mircobubbles encapsulated with nanoparticles. The reported average diameter is 2 μm and the shell thickness is 2-3 nm.

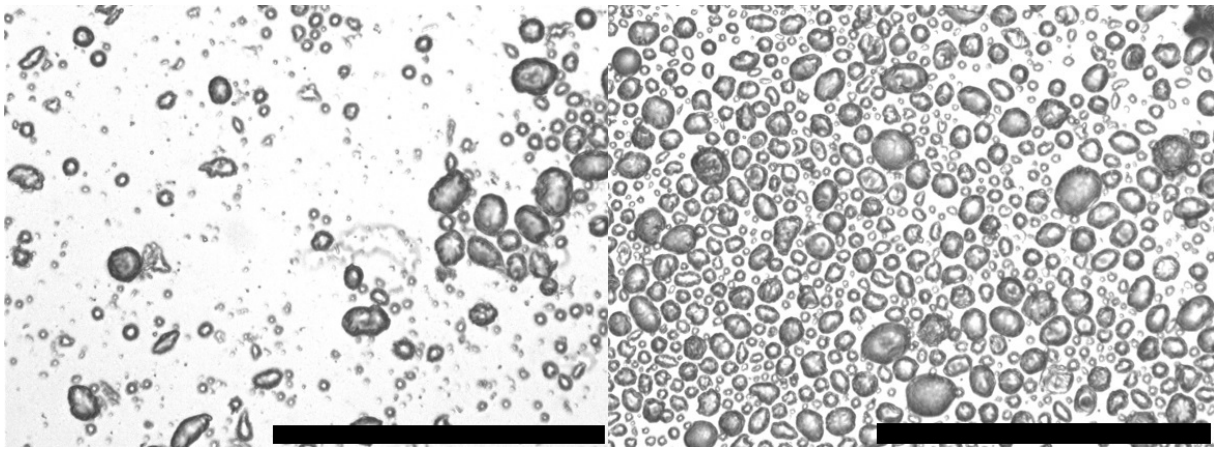

(a) BSA 0.1 wt%



(b) BSA 0.5 wt%

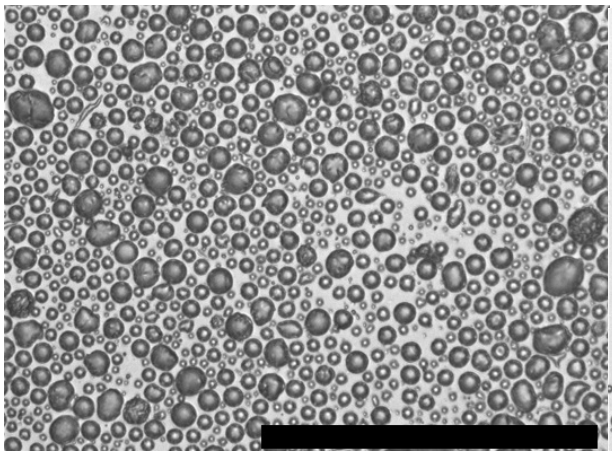

(c) Casein 0.1 wt%

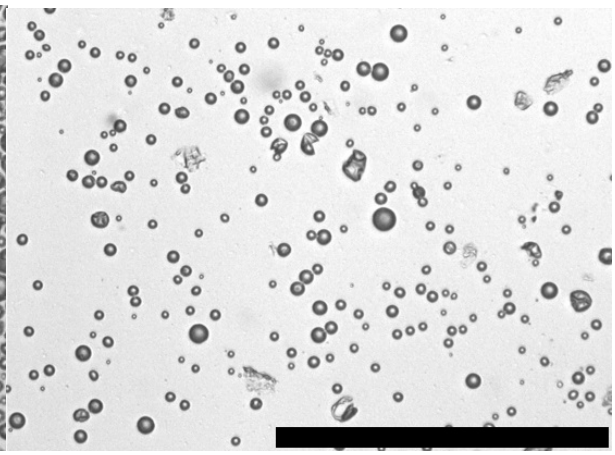

(d) Casein 0.5 wt%

Figure 3.3: Phase contrast images of BSA and casein microbubbles produced by different concentration of BSA and casein. The Ultra-Turrax velocity was 16000 rpm and the same for all microbubbles in these images. The scale bar is 100 μm.

## 3.2 Acoustic characterization of microbubbles

### 3.2.1 Water tank and sample chamber

A water tank and a sample chamber have been custom made at Mechanical Workshop, The Faculty of Natural Sciences and Technology, NTNU. The water tank is made of plexi-glass and has a opening in front to allow mounting of transducers. Figure 3.4 shows a sketch of the water tank seen from the side. Adapters enable use of transducers with different apertures. A second opening in the roof, as seen in the figure, is used for receive transducers. The 45° angle with respect to the transmit axis allows receiving of both monopole scattering, as well as dipole scattering.

The sample chamber is made of plexi-glass. Membranes made of mylar function as acoustic windows in front and in back, so that pressure waves can enter and leave with minimal attenuation and reflection. The water tank has a track that fits to the sample chamber and facilitates easy removal of the chamber. The track ensures that the sample chamber is always positioned equidistant from the transducers. The distance is chosen so that the maximum pressure of the transducer is obtained. Characterization of the transducers reveals that this distance should be 70 mm. The width of the sample chamber

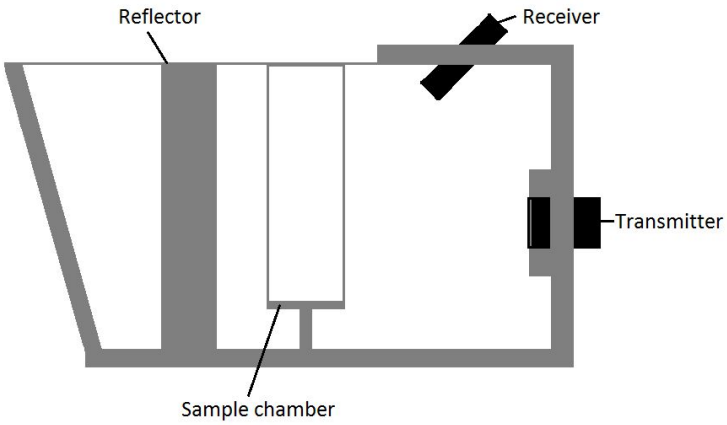


Figure 3.4: A sketch of the water tank viewed from the side. The transmit and receive transducers are mounted to the tank and directed towards the sample chamber. The reflector is positioned behind the sample chamber.

is determined by the beam profile. It is desired that the sample chamber is large enough to fit the transducer beam. For a focused transducer, the focus diameter $D_F$ defines the minimum chamber width, and it increases with smaller transducer diameter. The focused transducer with smallest aperture has a diameter of 19 mm and focus 70 mm. From equation 2.9, $D_F \simeq 11$ mm. For a flat transducer, the minimum chamber width is defined by the transducer diameter. The largest flat transducer has a diameter of 13 mm. The final chamber has width 30 mm, length 30 mm and height 80 mm, i.e, large enough dimensions to fit the beam of all transducers.

A 2.5 mm thick wall of plexi-glass can be placed in a second track located 27 mm behind the sample chamber track. This glass wall acts as a reflector during acoustic attenuation measurements. During backscatter measurements, the reflector wall is removed, and the tilted back wall prevents unwanted standing waves to build up.

The water tank is filled with degassed, deionized water. The degassing process is done by heating deionized water to boiling temperature and let it cool down.

### 3.2.2 Ultrasound transducers

#### Transducers

The transducers used in the experimental work of the thesis are listed in table 3.1.

#### Characterization of transducers

Characterization of the transducers is done at Department of Circulation and Medical Imaging, NTNU. The trandcucer is positioned in a water tank and excited by a pulser-receiver (Panametrics-NDT Model 5900PR, Waltham, MA, USA). A hydrophone (Onda HGL-0200, Onda Corporation, Sunnyvale, CA, USA) detects the pulses, and an oscilloscope (LeCroy Wavesurfer 44XS, Long Branch, NJ, USA) receives the signal. The

Table 3.1: Overview of the specifications of the transducers used in the experimental work.

| Type | Center freq. [MHz] | Aperture [inches(mm)] | focused/ flat | focus/ location of max intensity |
|---|---|---|---|---|
| Ultran WS100-1-P85 | 1 | 1.25"(32) | focused | 85 mm |
| Panametrics V381 | 3.5 | 0.75"(19) | focused | 70 mm |
| Panametrics V308 | 5 | 0.75"(19) | focused | 70 mm |
| Panametrics V309 | 5 | 0.5"(13) | flat | 70 mm |
| Panametrics V320 | 7.5 | 0.5"(13) | flat | 70 mm |
| Panametrics V311 | 10 | 0.5"(13) | flat | 70 mm |
| Panametrics V319 | 15 | 0.5"(13) | flat | 70 mm |

oscilloscope and the position of the hydrophone can be controlled and data acquired by a PC with the MATLAB program ProbeLab. A relationship between the applied voltage and the amplitude of the resulting pressure waves at different distances along the center axis is obtained. This information can be used to specify the amount of applied pressure during measurements of attenuation and backscattering, in addition, it has been used to localize the position of maximum intensity and hence an optimal location for the sample chamber in the water tank. The frequency response of the transducer is estimated by calculating the power density spectrum of the measured pulse at a pressure 20 kP and a distance ca. 13 mm between the probe and the hydrophone. The distance and pressure is kept low to avoid distortions.

### 3.2.3 Acoustic attenuation

Suspended microbubbles in an acoustic field absorb as well as scatter energy. The resulting attenuation of the ultrasound can be measured and used to obtain information about the microbubbles; not only about how they behave as a contrast agent upon insonification, but also about their viscoelastic properties.

#### System setup

The method used to measure the acoustic attenuation caused by microbubbles is based on work done by Hoff [22]. Measurements of attenuation require only one transducer that is positioned in the opening in the front of the water tank. The transducer works as a sender and a receiver. Ultrasound waves emitted from the transducer will be scattered and absorbed by microbubbles in the sound path, and a fraction of the ultrasound waves will be reflected by the reflector wall and returned to the transducer. By comparing the measurements of the received signals with and without microbubbles in the sample chamber, the attenuation caused by the microbubbles can be measured. The frequency response of the transducers and a possible effect of the sample chamber on the attenuation is compensated for by the nature of the experiment, because the reference signal only differs by the absence of microbubbles in the sound path.

A waveform generator (33500B Series Waveform Generator, Agilent Technologies, Penang, Malaysia) is connected to the transducer and excites it with pulses of 1 cycle and burst period 10 ms. The amplitude is set to 10 V for the 5 MHz, 7.5 MHz, 10 MHz and 15 MHz transducers and 3 V for the 3.5 MHz transducer. An oscilloscope (LeCroy

Waverunner LT262, Long Branch, NJ, USA) is connected to both the waveform generator and the transducer with a T connector. The waveform generator triggers the oscilloscope, and the oscilloscope registers pulses received in the transducer. The oscilloscope is then connected to a PC.

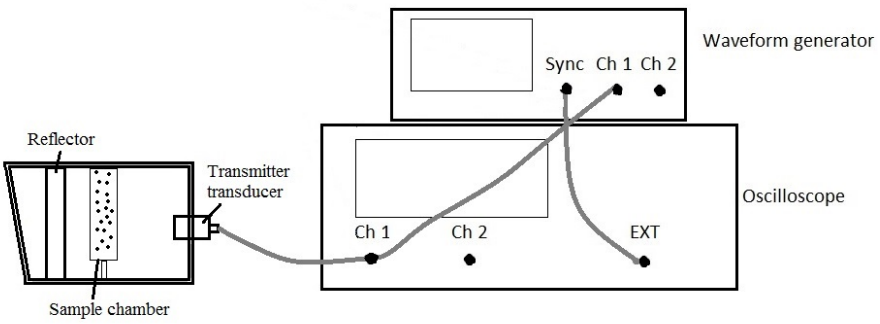


Figure 3.5: A sketch of the instruments and the connecting circuits used for acoustic attenuation measurements.

### Sample preparation

The sample chamber is filled with 50 ml degassed and deionized water, and an appropriate amount of a microbubble suspension is then pipetted into the chamber to make a desired concentration. The amount of added suspension varies between 30 - 100 µl. Different types of microbubbles are measured, and the concentration depends on the type. The concentration has been chosen so that the maximum measured attenuation is around 5 dB/cm. In addition, measurements are done with higher and lower concentration to ensure that the attenuation is proportional to the concentration, which indicates that the microbubble concentration is dilute enough to avoid microbubbles influencing each other. When doing measurements of one bubble type, it is important that approximately the same number of microbubbles are added every time, as the attenuation depends on the concentration. This is achieved by homogenizing the bubble suspension in the container by shaking it gently before pipetting, and also by rinsing the pipette tip surface before dispensing. The latter is done to avoid an unknown contribution from a significant amount of microbubbles observed attached to the outside of the tip.

### Measurements and data acquisition

The oscilloscope receives signals continuously. The pulse sent directly from the waveform generator is used as a time reference. The received signal that comes from the transducer and represents the pulse reflected from the reflector wall is identified by the time difference from the reference signal. With $c \approx 1500$ m/s, and sound path $\approx 20$ cm, the time difference is approximately $1.3 \cdot 10^{-4}$ s. The received pulses are digitized at sample rate 1 Gsa/s in the oscilloscope. 200 successive pulses are averaged to improve signal-to-noise ratio. The results are saved on a PC. A measurement of the filled sample chamber without added microbubbles becomes the reference. A new reference is found whenever the sample chamber is refilled or a new transducer is used. Measurements with microbubbles present are performed 5 minutes after the microbubbles have been added. Because the

microbubbles are buoyant and float up, and the attenuation therefore reduces with time, only one measurement is done of a sample to obtain reproducible results. The sample is then removed and the sample chamber rinsed with ethanol before a new sample is prepared and new measurements performed. 5 minutes are chosen so that the microbubbles are more homogeneously distributed in the sample chamber. From figure 4.7 in the results, at 5 minutes, the attenuation is observed to change minimal or actually increase compared to immediately after addition, indicating that this is a more appropriate time than immediately after. To get a spectrum over more frequencies, measurements are done with transducers with different center frequency. Typical pulses measured with the 5 MHz transducer with absence and presence of microbubbles in the sound path are shown in the figures 3.6a and 3.6b, respectively.

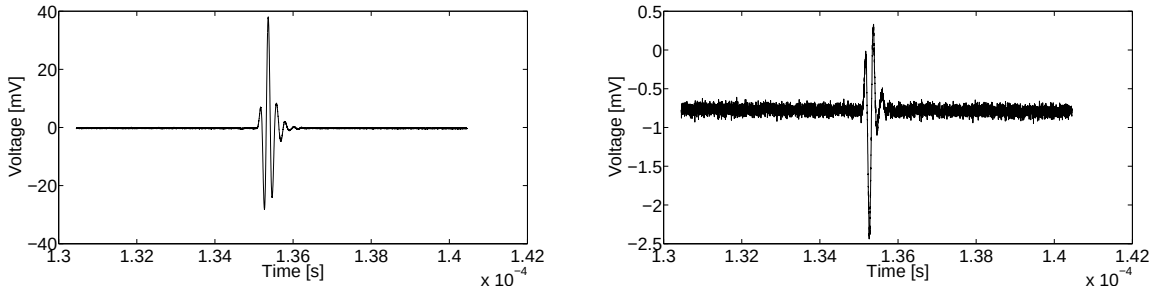


(a) (b)

Figure 3.6: (a) Received pulse with microbubbles in sound path. (b) Received pulse without microbubbles present.

### Data Analysis

The attenuation coefficients are calculated as a function of frequency in MATLAB (MathWorks, Natick, MA, USA). The fast forward transform (FFT) of the pulse and the corresponding reference pulse are calculated and converted to decibel (dB). The resulting power spectra, divided by the sound path length through the sample chamber $z$, are shown in figure 3.7. The normalized attenuation spectra $\alpha(\omega)$ are found by subtracting the power spectrum of the pulse attenuated by the microbubbles from the power spectrum of the reference:

$$\alpha(\omega) = \frac{1}{z} 20 \left( \log|\mathrm{FFT}\{x_{Ref}(t)\}| - \log|\mathrm{FFT}\{x_M(t)\}| \right) \tag{3.1}$$

Attenuation spectra obtained from different samples are averaged and plotted around the center frequency of the transducer with range limits defined where there is transition to unacceptable amount of noise. Averaged attenuation spectra obtained from transmit transducers with different center frequency are plotted together. Overlapping spectra from different transducers controls that attenuation measurements are independent on transducer characteristics.

### Theoretical calculations

The measured attenuation spectra can be compared with theoretical calculated attenuation spectra to determine values of parameters for elasticity and viscosity of the microbubble shell. A self-made MATLAB program computes the attenuation spectra using

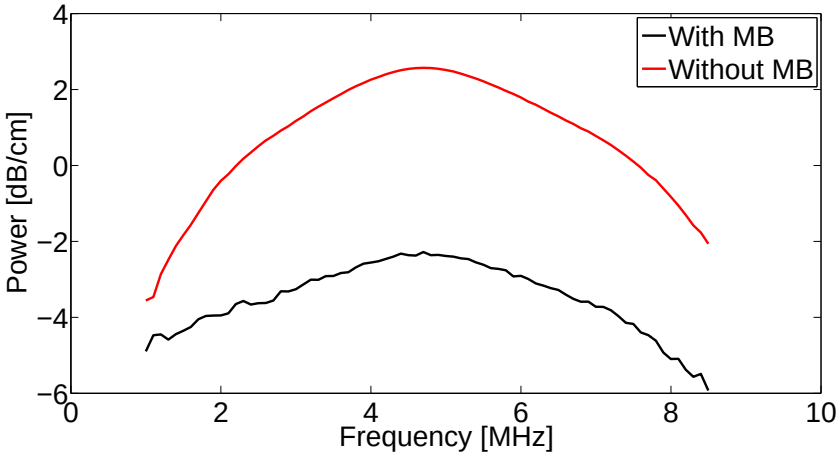


Figure 3.7: Power spectra in units of dB/cm of received pulses with and without microbubbles (MB) present in the sample chamber.

the Church and the Hoff model. The equations 2.19-2.21, that are obtained from the Church model, are inserted into equation 2.22. The number density $f(R_{01})$ is found from the size distribution measured by the Coulter Counter. $R_{01}$ is the inner radius of the bubble, i.e., the shell thickness subtracted from the radius of the bubble. The limits in the integral are 2 μm and 12 μm. Counts below 2 μm are assumed to be caused by nanoparticles and are not included. The attenuation can eventually be obtained from the first exponent in equation 2.25.

For the Hoff model, the attenuation is calculated from equation 2.32. $f(R)$ is also obtained from the size distribution and is the same as above. The difference is that $R$ here is the outer bubble radius. The limits of the integral are the same as for the Church model.

The calculated attenuation coefficients are plotted as a function of frequency. The resulting theoretical attenuation spectra are then fitted to the measured spectra by determining the values of the shear modulus and viscosity of the shell that minimize the summed squared difference between the spectra. These values represent estimates for the microbubble shell parameters.

### 3.2.4 Acoustic backscatter

Scattering performance of microbubbles is important in ultrasound imaging, as the image is formed by received echoes. The acoustic backscatter is measured by a method based on Hoff's thesis [22]. Two separate transducers are used. The transmit transducer is positioned in the front, while the transducer for receive is placed in the roof at 45 ° angle to the incident wave. The angle is selected so that both monopole, as well as dipole scatter can be measured. Transmitted ultrasound pulses cause the microbubbles in the pathway to oscillate and pulsate. Diverging waves are generated and radiate in all directions. A fraction of the backscattered waves is detected by the receive-transducer. This is the measured acoustic backscattering and provides information used to characterize the microbubbles acting as contrast agents.

### System setup

In contrast to the acoustic attenuation measurements, only a small fraction of the energy reaches the receive transducer. Amplification is therefore necessary to observe a signal. The setup is shown in figure 3.8. A waveform generator (33500B Series Waveform Generator, Agilent Technologies, Penang, Malaysia) produces sine wave pulses with 20 cycles that can be manually triggered. A 50 dB power amplifier (Model 2100L RF Power Amplifier, ENI, Rochester, N.Y, USA) amplifies the pulses from the waveform generator before they excites the transducer for transmit. The received signal is amplified 54 dB in a gain receiver with 1 MHz highpass filter and 50 MHz lowpass filter (Panametrics-NDT Model 5900PR, Waltham, MA, USA). RF output phase is 180 °, damping 50 Ω and energy 8 $\mu J$. An oscilloscope (LeCroy Waverunner LT262, Long Branch, NJ, USA) captures the RF traces. The oscilloscope is externally triggered by the waveform generator and the gain receiver. The digitized received signal is then saved on a computer and processed with MATLAB (MathWorks, Natick, MA, USA).

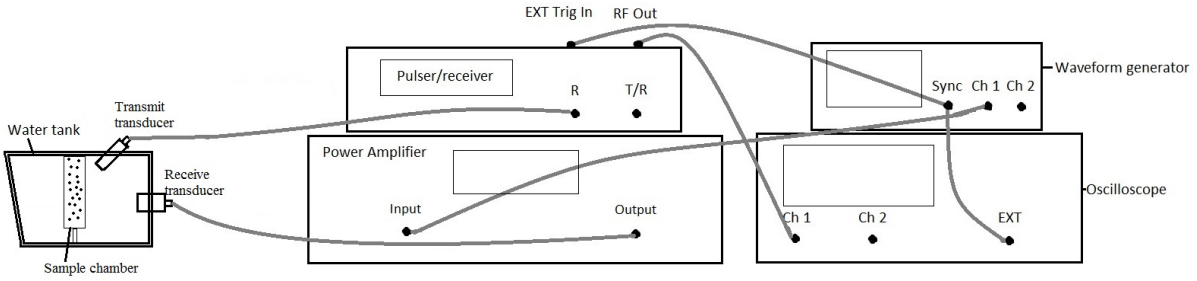


Figure 3.8: A sketch of the instruments and the connecting circuits used for measurements of backscattering.

### Sample preparation

The sample is prepared similarly as for acoustic attenuation in section 3.2.3. The same concentration is used. All measurements are done within 10-15 minutes after addition of microbubbles to the sample chamber, so that flotation effects are reduced.

### Data acquisition and analysis

One pulse at a time is transmitted from the transducer. The pulse generation is controlled manually from the waveform generator. The echo from the microbubbles is found in the received signal on the oscilloscope at a time determined by the speed of sound and the length of pathway. The sample rate of the oscilloscope is 500 Msa/s. The echo from a pulse is saved on a computer. No averaging is done. Thereafter, a new pulse is transmitted and an echo recorded. Voltages of the transmit pulses in the range 50 mV to 900 mV are applied. The voltage is then amplified with 50 dB$\approx$ 300 by the power amplifier. The backscatter from 12 different single transmit pulses with same voltage is measured and stored. The FFT of the signal $x$ is found with help of MATLAB to obtain the power density spectrum with power $X$ in dB,

$$X = 20\log|\mathrm{FFT}\{x\}|. \tag{3.2}$$

The frequency spectra from the 12 pulses are eventually averaged to improve signal-to-noise ratio. The pressure can then be changed, and new series of pulses can be measured.

The frequency spectra of the backscatter signal at different applied voltage, i.e. applied pressure, can inform about the stability of the bubble and at which pressure destruction occurs. Acoustic pressure is assumed to depend linearly on the voltage and can be obtained from transducer characterization.

### 3.2.5 Ultrasound imaging of microbubbles

An ultrasound scanner (Vivid 9, GE Health Care) with a 9L probe is applied to test the ability of microbubbles to give contrast and to determine the Mechanical Index (MI) at which they become destroyed. The microbubbles that are evaluated are coated with YM-73 nanoparticles and with either casein or BSA as surfactant proteins. The results from the imaging can inform about potential functional difference between the two proteins. A diluted microbubble suspension is passed through a tube in a phantom tissue, a material that tries to mimic human tissue imaging responses, and imaged with the pulse inversion technique by the ultrasound scanner. A suspension contains microbubbles with only one type of protein. The probe emits ultrasound at 3.6 MHz at receives at 7.2 MHz. The gain is changed so that the microbubbles can be imaged at different MI.

### 3.2.6 Coulter Counter

A Coulter Counter (Multisizer 3 Counter Coulter, Beckman Coulter, Brea, CA, USA) is used to obtain information about the microbubble concentration and size distribution. The instrument is based on the principle that particles suspended in an conducting liquid in an electric field causes disturbances to the electric field. The disturbance magnitude is proportional to the volume of the particle.

Microbubbles are suspended in a filtrated electrolyte solution of 0.05 M NaNO3. An aperture tube, consisting of a glass tube with a 50 μm aperture at its end, is placed in the suspension, and a vacuum pump draws the suspension through the aperture. Two electrodes are separated by the aperture and establish an electric field across the aperture. When particles are passing through the aperture, the particles displace their own volume of electrolyte solution and thus increases the impedance. The change in impedance is recorded as a pulse, and the pulse is proportional to the volume of the particle. A known volume (100 μl) is drawn into the aperture tube, and a count of the number of pulses yields the concentration of the microbubbles in the sample in addition to the size distribution. It is necessary that only one particle is restricted to the electric field at once to prevent coincidence measurements, i.e. several small particles are interpreted as one large. This is avoided by using a low concentration of particles, which here is 50 μl bubble solution per 30 ml electrolyte solution. 1.2 μm is the smallest particle diameter that can be detected with this aperture.

## 3.3 Compression of microbubbles with AFM Bioscope Catalyst

### System setup

Mechanical properties of microbubbles can be obtained by compressing a microbubble with a known force and measuring the resulting deformation. A tipless cantilever of an atomic force microscope (AFM) is applied to exert a force onto a microbubble fixed on a glass surface.

The instrument is a Bioscope Catalyst (Bruker, Billerica, MA, USA) located at Department of Physics, NTNU. The compression is done with tipless cantilevers from MicroMash type NSC12.

Integrated with the AFM is an inverted microscope, Zeiss Axio Observer D1. The sample is observed through a 40x/0.75 NA air-objective with an additional 1.6x lens. The filter set (74H) transmits excitation light at 480/30 nm and 565/25 nm and emitted light at 525/31 nm and 616/57 nm. Images can be acquired from either transmitted light or emitted light from Nile Red in the nanoparticles. Pictures are captured with an EMCCD-camera from Andor iXon (DU-897E). Instrument control and data acquisition is done by NanoScope software.

### Sample preparation

It is required that microbubbles are attached to a surface. The method used to fix bubbles on a glass surface has been established [56, 46] and is followed here.

A WillCo-dish (GWSt-5040) is coated with isopropanol for 1 minute, rinsed with distilled water and covered with 1 g/l branched polyethylenimine for 10-15 minutes. These polymers can immobilize microbubbles and make them stay fixed on the glass surface. A new 10 ml container is prepared and completely filled with distilled water and 5 µl microbubble suspension. The dish is then rinsed with distilled water 3 times and positioned inverted with the coated side down on top of the container with microbubble suspension. The procedure is illustrated in figure 3.9. As the microbubbles are observed to be buoyant, they will tend to float up and attach to the coated dish. The WillCo-dish is removed after 5-10 minutes and rapidly filled with sufficient amount of distilled water.

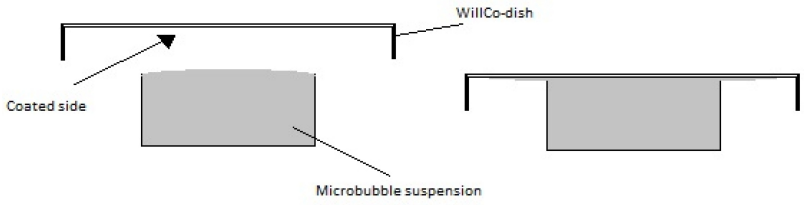


Figure 3.9: Schematic figure showing how the inverted dish was placed on top of the microbubble suspension.

### Localizing microbubbles and performing compression

The cantilever needs to be calibrated in order to determine the sensitivity and the spring constant. The spring constant is found from the Thermal Tune method. The deflection

sensitivity is found by pressing the cantilever on a hard surface.

The camera has to be cooled to −90° C. The dish is placed in the instrument, and bubbles localized by the microscope. Several bubbles are observed and potential bubbles are selected according to some criteria; circular shape, contains air, homogeneous shell thickness and not attached to other bubbles. Bubbles with different sizes are chosen. An image is captured of the bubble before compression.

During measurements, it is important that the cantilever is positioned with the microbubble entirely below the cantilever, and with the microbubble as close to the cantilever edge as possible. Figure 3.10 shows a captured image of a microbubble positioned below the rectangular cantilever. The compression is done with the Z closed loop kept ON. The scan rate of the z-piezo is approximately 2 μm/s for all measurements. 1024 samples are recorded.

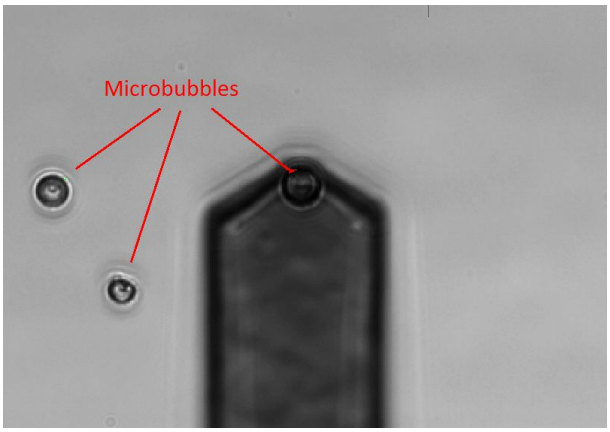


Figure 3.10: Image captured of a microbubble positioned below the cantilever just before compression.

### Data analysis

The diameter of the microbubbles is estimated by measuring the diameter in pixels in the images. The image is calibrated, so that the size of a pixel in nanometer is known. The diameter is then converted from pixels to micrometer.

The outcome of the measurements are force curves. The zero-point of the x-axis is where the maximum force is applied. The curves therefore give the relationship between the force and the distance to the position of maximum applied force. An example of a typical force-separation curve is found in figure 3.11. Only the approaching curve is analyzed. The deflection of the cantilever is measured and converted to force as the cantilever approaches and retracts from the microbubble. The deformation of a microbubble, $h$, begins at the contact point, where the value of the force first start to change, at approximately 0.35 μm separation in the figure. It is defined after inspection of different force curves, as where the force between two consecutive data points changes with more than 0.5 nN. The zero-point of the deformation is at the contact point, and the values of the deformation is found by subtracting the separation values from the value of separation at this position. A relative deformation, $\epsilon$, is obtained by dividing $h$ with the diameter $D$.

Reissner theory is employed to estimate the Young's modulus of the microbubble shell. Reissner theory is a linear model. It assumes that the microbubble shell is elastic and that there is a linear relationship between the force and the deformation. This is true

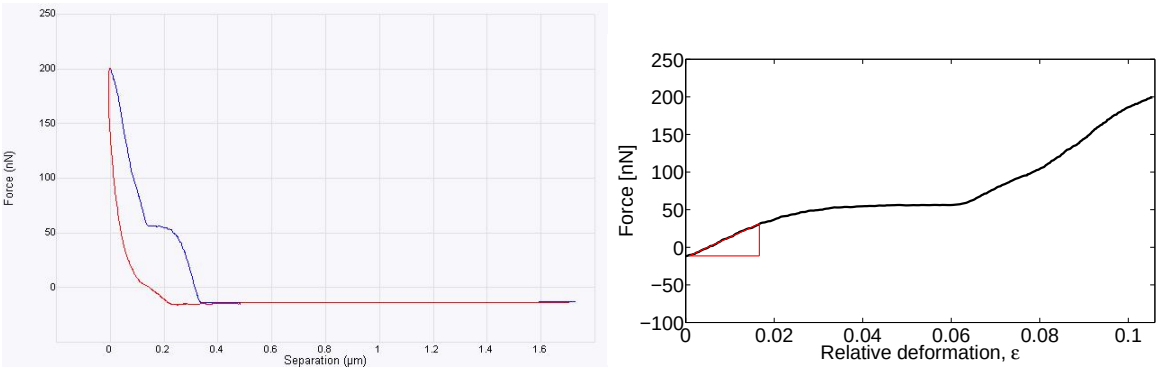


(a) Force-separation

(b) Force-relative deformation, $\epsilon = \frac{h}{D}$

Figure 3.11: Example of a force-separation curve and a force-relative deformation curve. In a), the blue curve is the approaching curve, while the red curve is the retracting curve. In b), the red triangle indicates the gradient obtained by linear regression fit.

only for some parts of the force curve. To acquire the gradient required in the equation for Young's modulus, a linear regression fit is applied in the initial linear region of the force-relative deformation curve. The region is defined to be the part of the curve with $\epsilon < 0.1$ where the longest linear fit with coefficient of determination $R^2$ above 0.995 can be achieved. The linear region and the regression is done by a program written in MATLAB.

Only the first or the second acquired force curve of a microbubble is considered, as further compressions potentially can destroy or damage the microbubble. Some microbubbles are compressed several times, and 8 force curves of these microbubbles are analyzed, so that the effect of multiple compressions can be investigated.

Statistical uncertainty is taken to be one standard deviation of the measured data set.

# Chapter 4

# Results

## 4.1 Size distribution

The size distribution of the microbubble batches used in measurements of acoustic attenuation are shown in figure 4.1. The distributions are determined from a Coulter Counter that generates histograms showing the number of counted pulses at a specific particle size interval. The counted pulses provide the number of microbubbles per 1 ml microbubble suspension. There is assumed to be no coincidence measurements, and only counts above 2 μm are included. The distribution of a batch is formed by averaging the distribution of three samples of that batch. The measured microbubbles are all stabilized by YM-73 nanoparticles. Two batches contain BSA as a surfactant protein and have either "large" or "small" microbubbles because they are generated with Ultra-Turrax velocity 8 000 rpm and 24 000 rpm, respectively. The third batch contain casein as a surfactant protein and is made with 16 000 rpm.

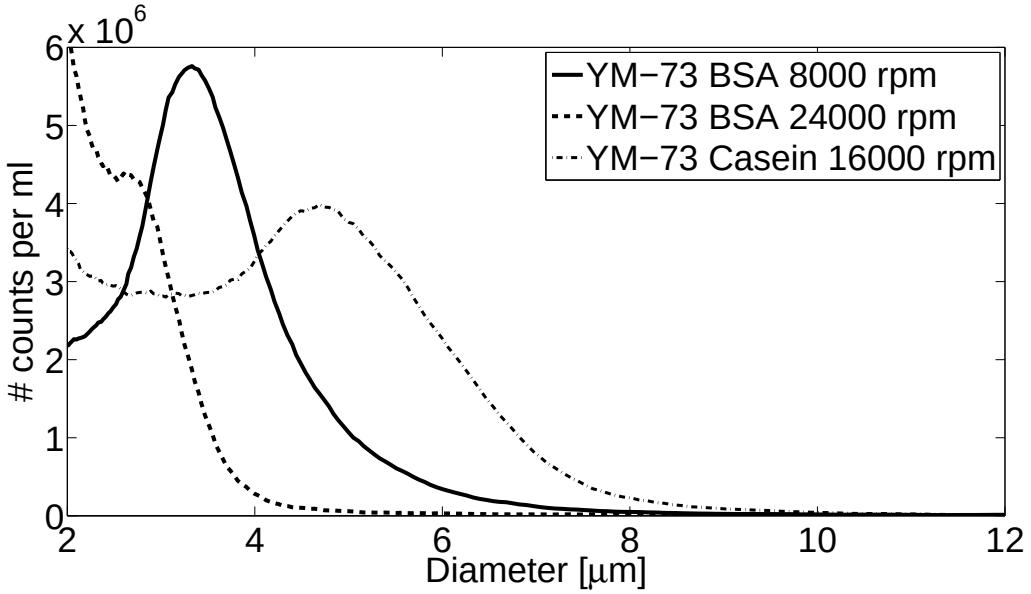


Figure 4.1: Size distribution of three microbubble batches stabilized by YM-73 nanoparticles and surfactant proteins.

Casein microbubbles have the largest average diameter with a maximum around 4.7 μm. The large BSA-microbubbles have a peak at ca. 3.3 μm, while the distribution of

the small BSA-microbubbles has a miniature peak at approximately 2.7 µm. All distributions are asymmetric and do not approach zero at the left side. Instead, the number of counts seem to increase at lower particle size. This is particularly evident for the smaller microbubbles, which have almost no reduce after the peak.

Table 4.1 lists the total number of counts per ml and the average volume fraction occupied by microbubbles with diameter above 2 µm for each microbubble batch. According to the results, the microbubbles occupy a considerable amount of the volume, approximately 6-19 % for the small and large BSA microbubbles, respectively.

Figure 4.2a shows the continuation of the distributions below 2 µm particle diameter. In addition, a suspension with only YM-73 nanoparticles are measured for comparison. All the microbubbles have distributions with a second peak at sizes between 1.2 and 1.3 µm. However, the number of counts for these peaks are almost 2 orders of magnitude higher than the peaks in figure 4.1. The differences are emphasized in the log plot in figure 4.2b. Interestingly, the distribution of the nanoparticle suspension does not coincide with the other peaks, but has a maximum at around 1.65 µm.

Eventually, a pure electrolyte solution is measured to control for artifacts (figure 4.2c). The number of counts are negligible compared to when the microbubbles or nanoparticles are present.

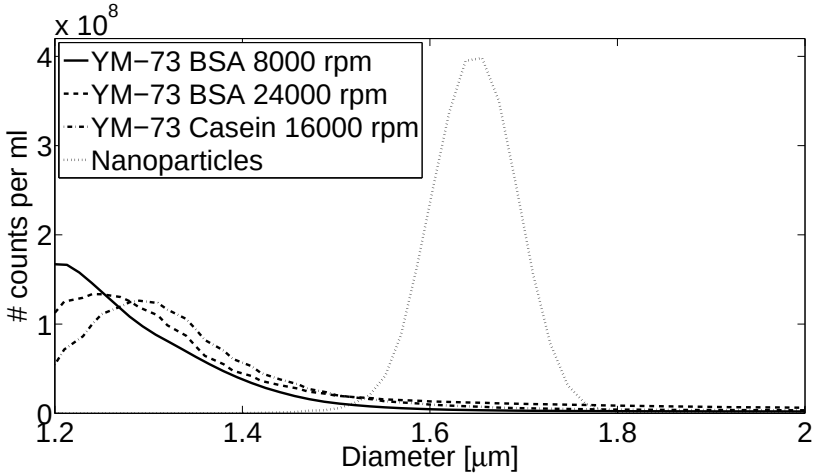


(a) Size distributions of the three microbubble batches and of YM-73 nanoparticles at particle sizes lower than 2 µm. Be aware that the counts are at the order of $10^8$.

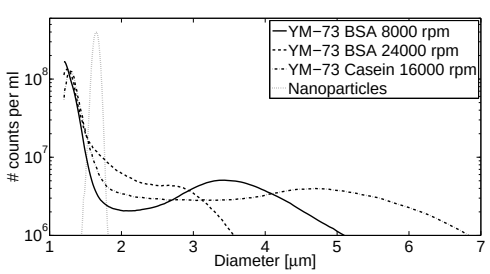


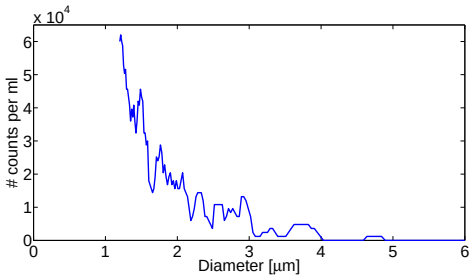


(b) Log plots of the number of counts as function of particle diameter.

(c) Measurements of pure electrolyte solution.

Figure 4.2

Table 4.1: Total number of microbubbles per ml and the average microbubble volume fraction obtained from the size distribution in figure 4.1 for the casein and the large and small BSA microbubbles.

| Batch | Total counts | Volume fraction |
|---|---|---|
| BSA, 8000 rpm | $3.9 \cdot 10^8$ | 0.059 |
| BSA, 24000 rpm | $11 \cdot 10^8$ | 0.185 |
| Casein, 16000 rpm | $4.3 \cdot 10^8$ | 0.083 |

## 4.2 Characterization of transducers

Information about transducer characteristics is important in the design process of the water tank and sample chamber to obtain appropriate dimensions. During the acoustic backscattering experiments, it is also necessary to have estimations for the frequency response of the receive transducers and the acoustic pressure for the transmit transducers. Results from transducer characteristics required in this thesis are presented below.

### Frequency response of receiving transducers

The frequency response of the receive transducers is estimated. The flat 5 MHz and 15 MHz transducers are excited by pulses and the transmitted pulses measured by a hydrophone. The resulting spectra are plotted in figure 4.3 and is used as an estimate for the frequency response of the transducers.

0 dB is defined to be at 1 and 10 MHz for the 5 MHz transducer and at 5 and 25 MHz for the 15 MHz transducer.

### Acoustic pressure

To be able to determine the applied acoustic pressure, a relationship between the pressure and applied voltage is found. A hydrophone is used to measure the pressure of the acoustic field from the focused 1 MHz and 3.5 MHz transducers and the flat 5MHz transducer at different distances between the probe and the hydrophone. The applied voltage is 300 mV in addition to a 50 dB power amplifier. The resulting scans are presented in figure 4.4. All transducers have their maximum intensity at approximately 70 mm. The water tank is therefore designed so that the distance between the transmit probe and the center of the sample chamber is 70 mm. The approximate acoustic pressures at this distance are listed in table 4.2. As expected, the flat 5 transducer shows less variations in transmitted pressure amplitude along its axis.

Table 4.2: Approximate acoustic pressure at 70 mm distance from the transducer. Voltage 300 mV with 50 dB gain is applied.

| Transducer | Center frequency | Pressure [kPa] |
|---|---|---|
| Ultran WS100-1 | 1 MHz | 170 |
| Panametrics V381 | 3.5 MHz | 520 |
| Panametrics V309 | 5 MHz | 135 |

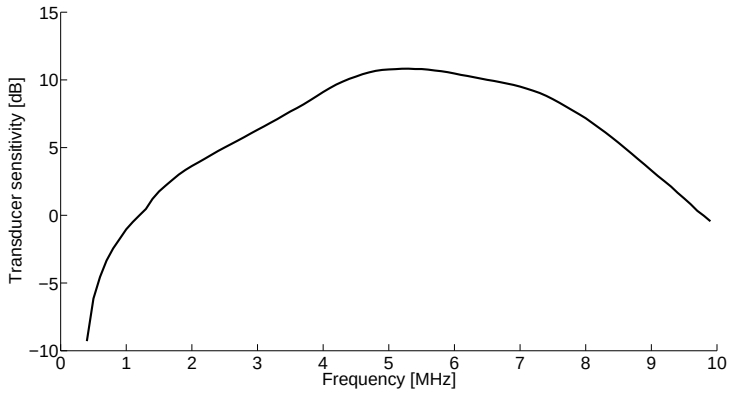


(a) 5 MHz

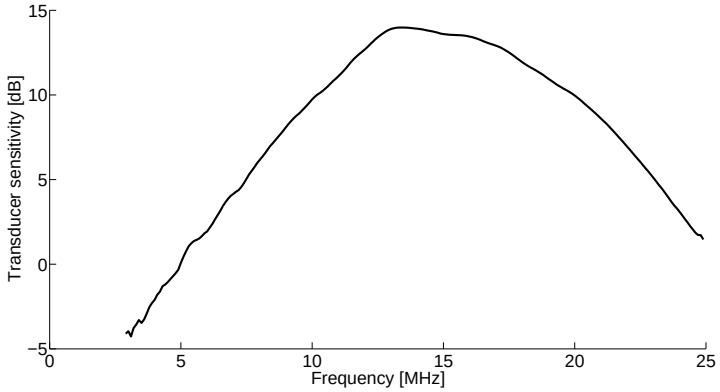


(b) 15 MHz

Figure 4.3: The frequency response of the transducers with center frequency (a) 5 MHz and (b) 15 MHz.

## 4.3 Acoustic attenuation

### 4.3.1 Acoustic attenuation spectra

Acoustic attenuation measurements are performed, and the acquired attenuation spectra are plotted in figure 4.5. The attenuation is measured with transducers with different center frequency. An acquired attenuation curve of a transducer consists of measurements from several samples that are averaged. The error bars represent one standard deviation of the samples at a specific frequency. The measurements are done 5 minutes after addition of microbubbles to the sample chamber, and the concentration of microbubbles in a sample is chosen so that maximum attenuation is around 5 dB.

The attenuation caused by a population of large YM-73 BSA microbubbles (figure 4.5a) is measured with transducers with center frequency 3.5 MHz, 5 MHz, 7.5 MHz and 10 MHz. For the 5 MHz transducer, 7 different samples are measured, and the obtained attenuation curves are averaged. The attenuation curves for the other transducers are each formed by averaging the curves from 4 different samples. The curves obtained by the different transducers overlap, that is, they are within one standard deviation, at all overlapping frequencies except in a region around 2.8 MHz. There is a maximum attenuation at 5.0 MHz.

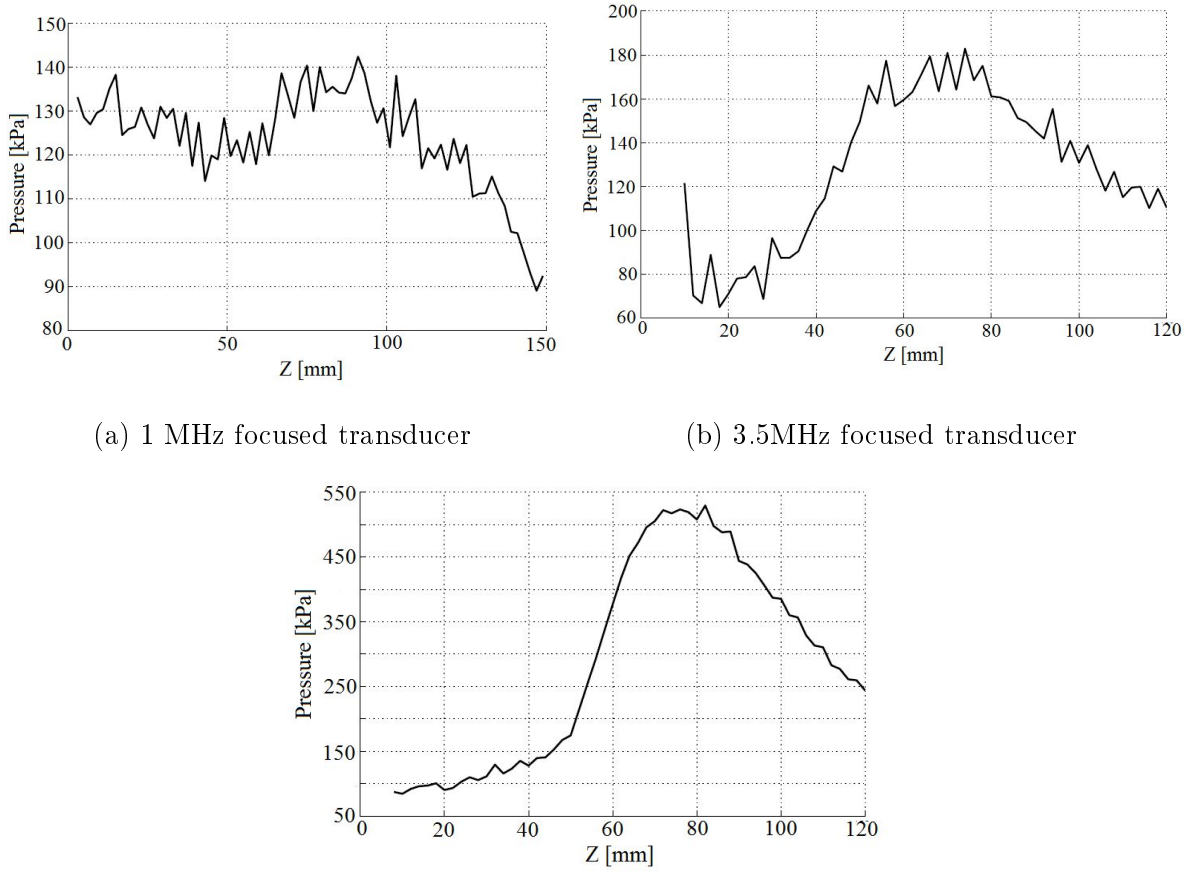


(a) 1 MHz focused transducer

(b) 3.5MHz focused transducer

(c) 5MHz flat transducer

Figure 4.4: Acoustic pressure measured by a hydrophone along the z-axis of transducers with center frequency (a) 1 MHz, (b) 3.5 MHz and (c) 5 MHz.

Figure 4.5b shows the attenuation curve for the smaller microbubbles stabilized by YM-73 and BSA. Curves from 6 different samples are averaged for the 15 MHz transducer, while 3 different samples are used with the 5 and 10 MHz transducers. There is significant overlap between the curves for the 5 MHz, 10 MHz and 15 MHz transducers. The maximum is at approximately 14 MHz, which is substantially higher than for the larger microbubbles. The shape of the curve is also different. Whereas for the larger YM-73 microbubbles, the slope of the curve is steep at low frequency, the slope for the smaller microbubbles is gentle.

The casein microbubbles are measured with a 5MHz transducer (figure 4.5c). 5 different samples are averaged and used to produce the attenuation curve. A maximum is observed at approximately 7 MHz. This is higher than for the large BSA microbubbles.

In figure 4.5d, the attenuation spectra without error bars are plotted together, so that the differences between the microbubble batches are accentuated. Evidently, reducing the microbubble size or changing BSA to casein, both shift the maximum to at higher frequency.

For comparison, the attenuation of a commercial microbubble is measured and shown in figure 4.5e. The 15 MHz transducer is used, and the measurements from 6 different samples are averaged. There appears to be a maximum around 19 MHz, which is higher than for the small YM-73 microbubbles.

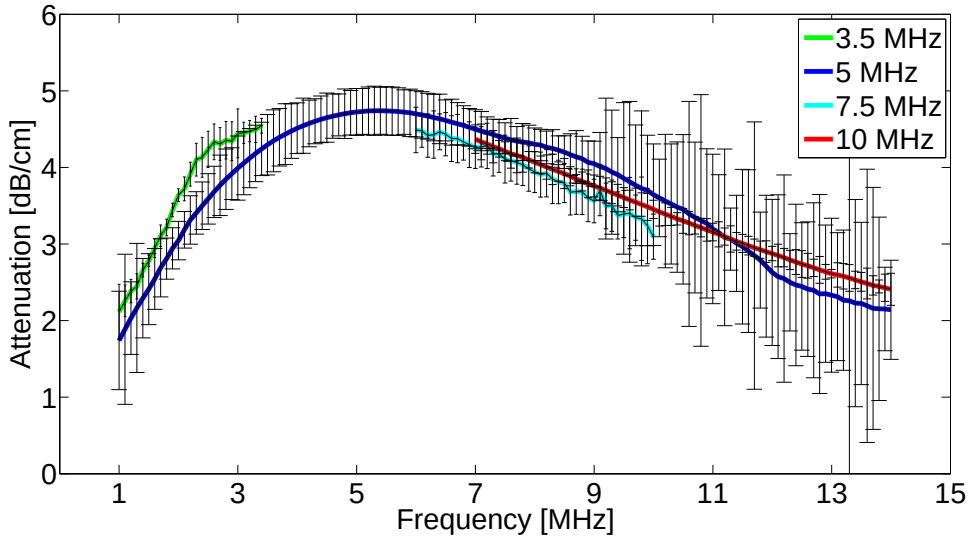


(a) YM-73 BSA large

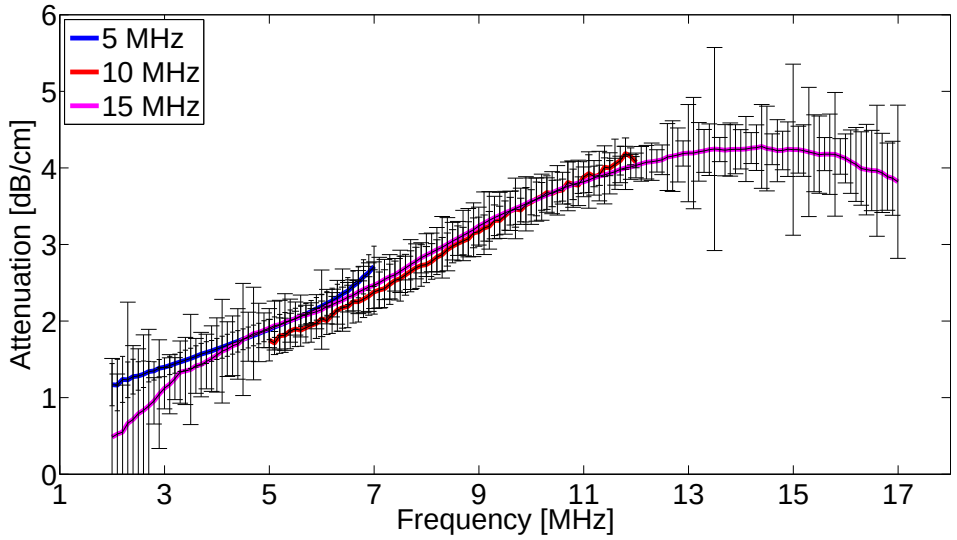


(b) YM-73 BSA small

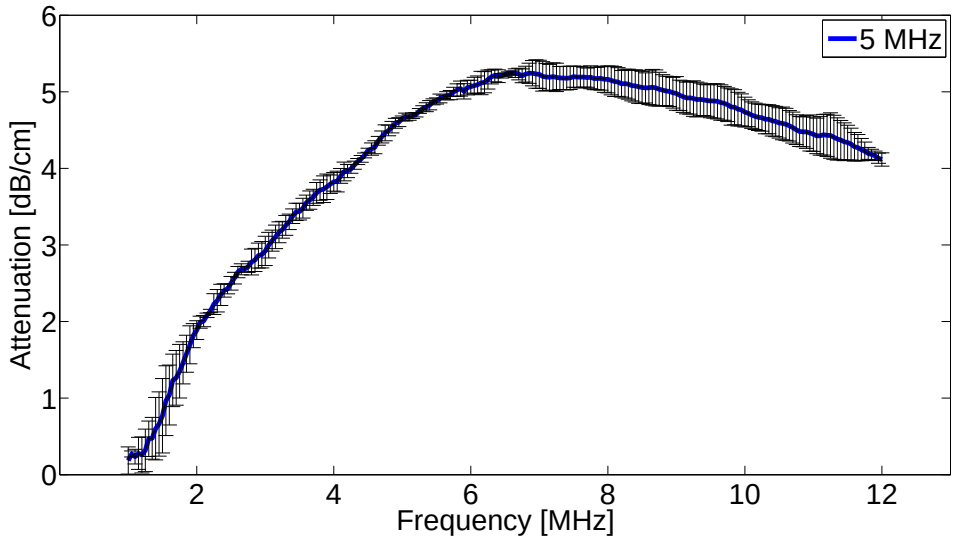


(c) YM-73 Casein

Figure 4.5

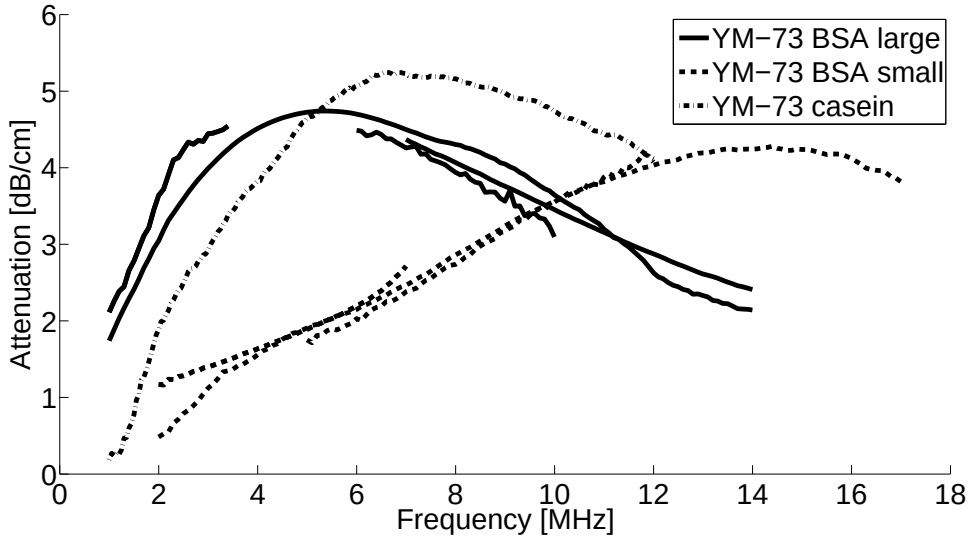


(d) All YM-73 microbubbles

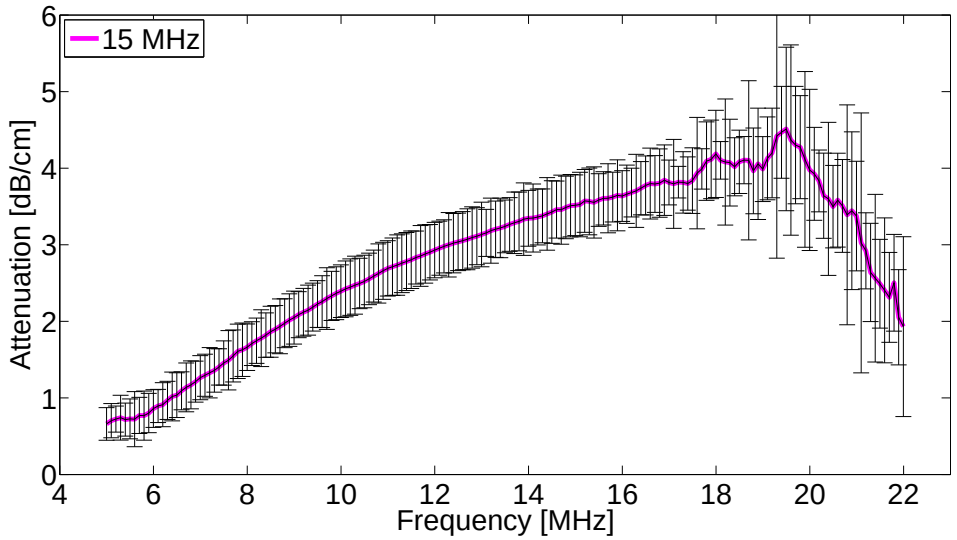


(e) HEPS-Na/PFB Microbubbles

Figure 4.5: Measured attenuation in dB/cm as a function of frequency for three different YM-73 microbubbles and a HEPS-Na/PFB microbubble. Pulses of 1 cycle and burst period 10 ms are transmitted by different transducers. The center frequency of the transducers used for the respective microbubble batch is shown in the plot legend. Each attenuation curve obtained by a transducer is an average of attenuation curves obtained from several samples. The error bars represent one standard deviation. For the large BSA microbubbles, 7 samples are measured with the 5 MHz transducer, and 4 samples are measured with the other transducers. For the small BSA microbubbles, curves from 6 samples are averaged for the 15 MHz transducer, while 3 samples are measured with the 5 and 10 MHz transducers. 5 samples are used with the 5 MHz transducer for the casein microbubbles, and with the 15 MHz transducer for the commercial microbubbles, the attenuation curves from 6 samples are averaged.

### 4.3.2 Theoretical predictions and shell parameters

Theoretical acoustic attenuation spectra are calculated from bubble models. The theoretical spectra can be fitted to the experimental spectra by selecting appropriate values for the shear modulus of the shell, $G_s$, and for the viscosity of the shell, $\mu_s$, in the models. The parameter values that best fits the calculated curve to the measured curve, represent estimations of the parameter values for the viscoelasticity of the microbubble shell.

#### Church model

Church model is used to calculate theoretical attenuation spectra for the three YM-73 microbubbles. Estimations for the values of the shear modulus $G_s$ and the viscosity $\mu_s$ is done by adjusting their values in order to minimize the summed square difference between the theoretical and experimental curves. The values of $G_s$ and $\mu_s$ are then increased and reduced around the estimated values, and the largest and lowest values that still cause the calculated curves to be within the error bars of the measured curves, i.e., within one standard deviation, are taken to be the uncertainty limits of $G_s$ and $\mu_s$. The results are found in table 4.4. Figure 4.6 contains plot of the attenuation spectra acquired from measurements and calculation using Church model and the estimated shell parameter values.

The shell thickness is not measured here. Estimations in a project work concluded with a thickness of 1-2 nanoparticle layers [57]. In this thesis, the shell thickness is assumed to be 150 nm, corresponding to a single layer of nanoparticles. Table 4.5 shows obtained values with different assumptions for the shell thickness. The assumed values of the other necessary parameters are found in table 4.3. The compressions of the microbubbles are supposed to be adiabatic, i.e., the polytropic constant, $\kappa$ is 1.4. The density of the microbubble shell is not known. Though, the density of PBCA is approximately 1200 kg/m$^3$ [58] and is here an estimation for the shell density.

Table 4.3: Parameters and their assumed values used in the models.

| Parameter | Value |
|---|---|
| Density of shell, $\rho_l$ | 1200 kg/m$^3$ |
| Density of water, $\rho_s$ | 1000 kg/m$^3$ |
| Viscosity of water, $\mu_l$ | $8.9 \cdot 10^{-4}$ Ns/m$^2$ |
| Equilibrium gas pressure, $p_{0g}$ | 103 kPa |
| Polytropic constant, $\kappa$ | 1.4 |

It was realized that a constant multiplied with the concentration of microbubbles reduced the summed square error and improved the fit, which is apparent in figure 4.6, where the green curve is the best fitted calculated curve using $constant = 1$, and the red curve is the best fitted calculated curve using the optimal constant. The effect of introducing this constant is most pronounced for the casein bubbles, and least for the smaller BSA bubbles. The origin of this constant appears to be use of a too large volume fraction occupied by the bubbles that is not taken into account by the model, as discussed later. The results in table 4.4 are found with the constants that give the best fit, i.e., minimize the summed square error. The effect of improving the fit done by this constant multiplied with concentration could not be compensated for by adjusting other parameters, including shell thickness. With use of this constant, the calculated attenuation spectra (colored

red) can be fitted reasonable well to the measured spectra and within the error bars at most frequencies.

Table 4.4: Values of the shear modulus $G_s$ and the viscosity $\mu_s$ of the shells of three different batches of microbubbles encapsulated by YM-73 nanoparticles. The shell thickness is assumed to be $t = 150$ nm, and values of the other parameters are found in table 4.3. The optimal values of the constant multiplied with the concentration in the calculations are included.

| Microbubble batch | Shear modulus, $G_s$ [MPa] | Viscosity, $\mu_s$ [Ns/m$^2$] | Const. |
|---|---|---|---|
| YM-73 BSA large | $7.4 \pm 1.1$ | $0.46 \pm 0.03$ | 2.8 |
| YM-73 BSA small | $14.4 \pm 2.5$ | $0.25 \pm 0.03$ | 1.5 |
| YM-73 casein | $30.7 \pm 2.8$ | $1.29 \pm 0.06$ | 3.0 |

The calculations show that the YM-73 casein microbubbles are estimated to have the largest values of shear modulus and viscosity. Replacing BSA with casein seems to increase the shear modulus and viscosity. From the estimations, the small YM-73 BSA microbubbles have a shear modulus that is approximately a factor 2 higher than the larger BSA microbubbles, whereas the value for viscosity is almost a factor 2 lower. As a consequence, both the shear modulus and the viscosity of the shell appear to depend on the microbubble diameter.

### Comparing Church and Hoff model at different shell thickness

The values of the shear modulus and the viscosity for the shell of the large YM-73 BSA microbubbles are estimated by applying the Hoff model as well as the Church model. Theoretical attenuation spectra are calculated in both models and fitted to the experimental spectra by selecting appropriate values of the parameters. The results are presented in table 4.5. The concentration is multiplied with the same constant as above, and using a different model has no influence on the optimal value of the constant. The thickness is varied between 15 nm and 300 nm in order to investigate the effect of shell thickness on the results. At thickness 15 nm, there is negligible difference between the results obtained by the models. The difference is larger at 150 nm and significant at 300 nm thickness. The result of increasing the thickness seems to be a lowering of the estimated values of both shear modulus and viscosity.

Table 4.5: Values of the shear modulus $G_s$ and the viscosity $\mu_s$ for the shell of the large microbubble stabilized by YM-73 nanoparticles and BSA using Church model and Hoff model with different values of the thickness. The constant is 2.8.

| Thickness | Model | Shear modulus, $G_s$ [MPa] | Viscosity, $\mu_s$ [Ns/m$^2$] |
|---|---|---|---|
| 15 nm | Church | $90 \pm 12$ | $5.2 \pm 0.6$ |
| | Hoff | $90 \pm 12$ | $5.3 \pm 0.6$ |
| 150 nm | Church | $7.4 \pm 1.1$ | $0.46 \pm 0.03$ |
| | Hoff | $8.5 \pm 2.0$ | $0.53 \pm 0.03$ |
| 300 nm | Church | $3.4 \pm 0.6$ | $0.18 \pm 0.02$ |
| | Hoff | $4.5 \pm 0.5$ | $0.27 \pm 0.02$ |

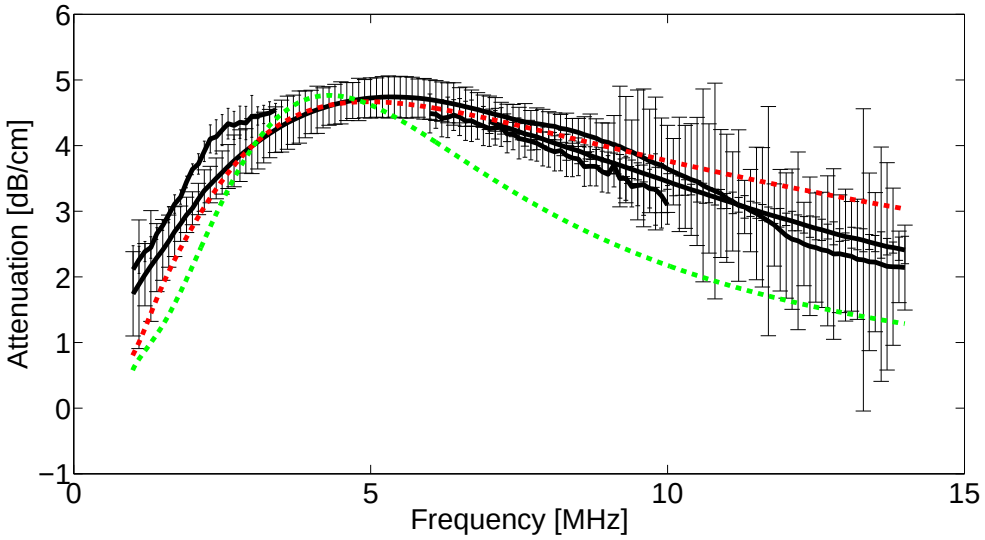


(a) YM-73 BSA large

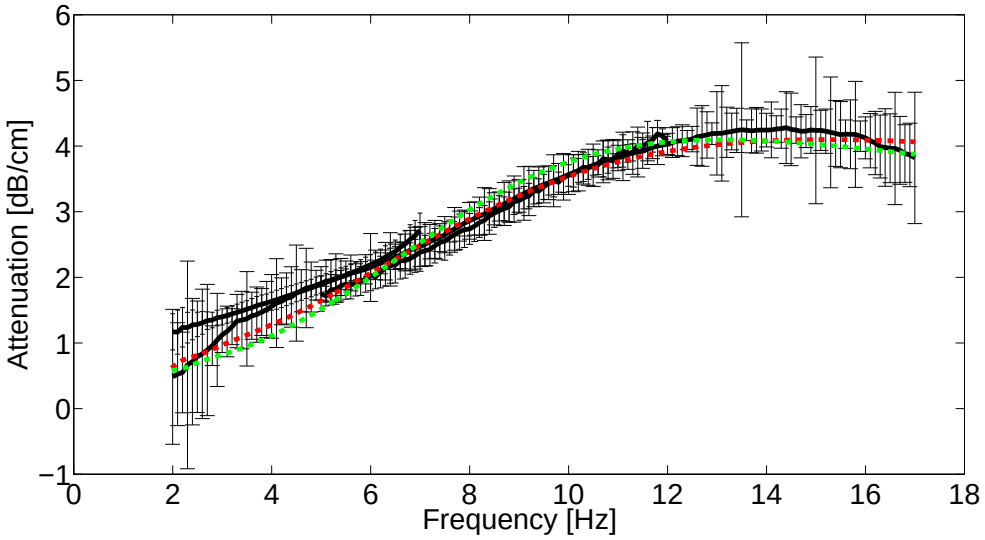


(b) YM-73 BSA small

Figure 4.6

### 4.3.3 Time dependent acoustic attenuation

The buoyancy of the YM-73 microbubbles is tested by measurements of the acoustic attenuation at fixed time intervals after the addition of microbubbles. The measurements are done immediately after addition and every 5 minutes up to 20 minutes. Pulses are not transmitted between the measurements to ensure that the reduction is not caused by long-term ultraound exposure of the microbubbles. Samples with large and small BSA microbubbels are analyzed. The attenuation coefficient is observed to reduce as the time increases, but the buoyancy rate depends on the microbubble size. In addition, the reduction of attenuation seems to increase after more time.

The attenuation spectra measured from a sample containing large YM-73 BSA microbubbles are shown in figure 4.7a. There is first a small increase of the attenuation, indicating that the mixture was not initially homogeneous. Thereafter, a gradually diminution of the attenuation continues. At 20 minutes, the reduction at center frequency is

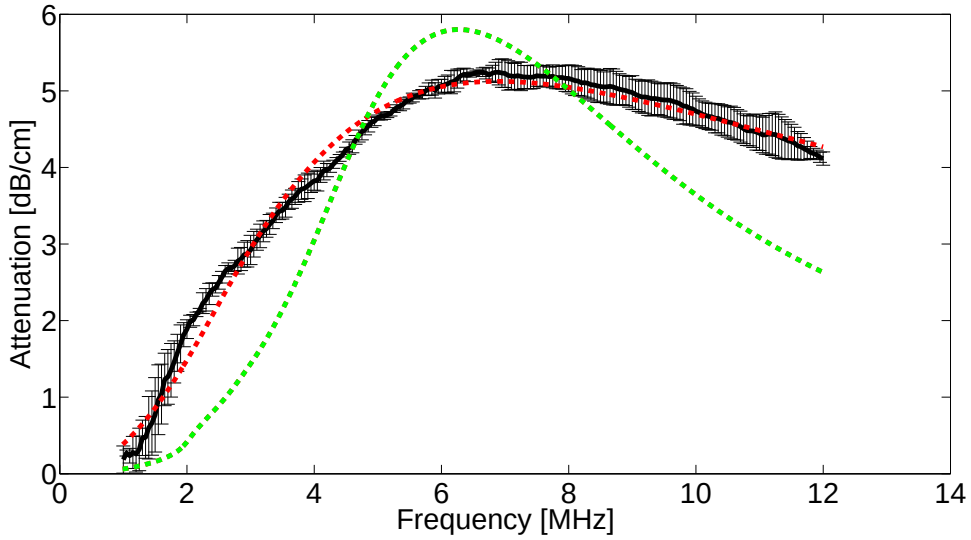


(c) YM-73 casein

Figure 4.6: The calculated attenuation spectra using constant equal to 1 (dashed, green lines) and the optimal constant (dashed, red lines) are plotted along with the measured attenuation spectra (black lines) from figure 4.5. The constant refers here to a constant that is multiplied to the concentration. The fits are done by selecting appropriate values for the viscoelastic parameters of the shell that minimize the summed square difference between the measured and calculated attenuation curve.

approximately 2 dB/cm. An estimated decrease of attenuation per minute is then 0.1 dB/cm/min. The resonance frequency increases as the time passes, clearly visible at 20 minutes. Because larger bubbles have lower resonance frequency, the fraction of small bubbles have increased. This indicates that larger bubbles are more buoyant and float up faster. After the 20 minutes measurement, the sample is stirred with a pipette, and a new measurement is done. There is an evident increase in the attenuation and reduction of the resonance frequency, but still not to the level at 0 minutes.

The latter statement is confirmed in figure 4.7b. There is a lower reduction of attenuation, less than 0.5 dB/cm at the center frequency the first 20 minutes. A small displacement of the curves towards higher frequency at larger times can be noticed. A measurement is also done after 60 minutes and shows a reduction of ca. 1 dB/cm. An estimated attenuation decrease per minute is 0.02 dB/cm/min.

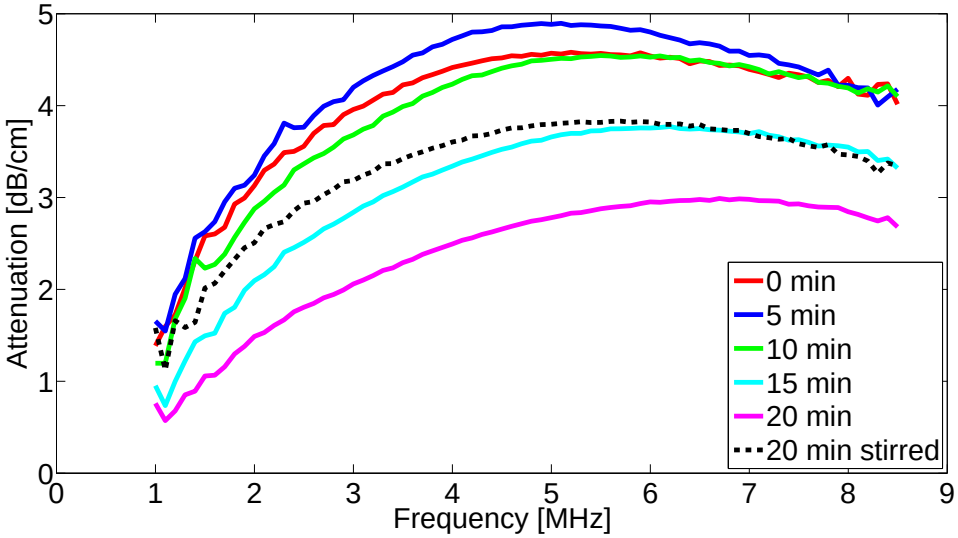


(a) YM-73 BSA large

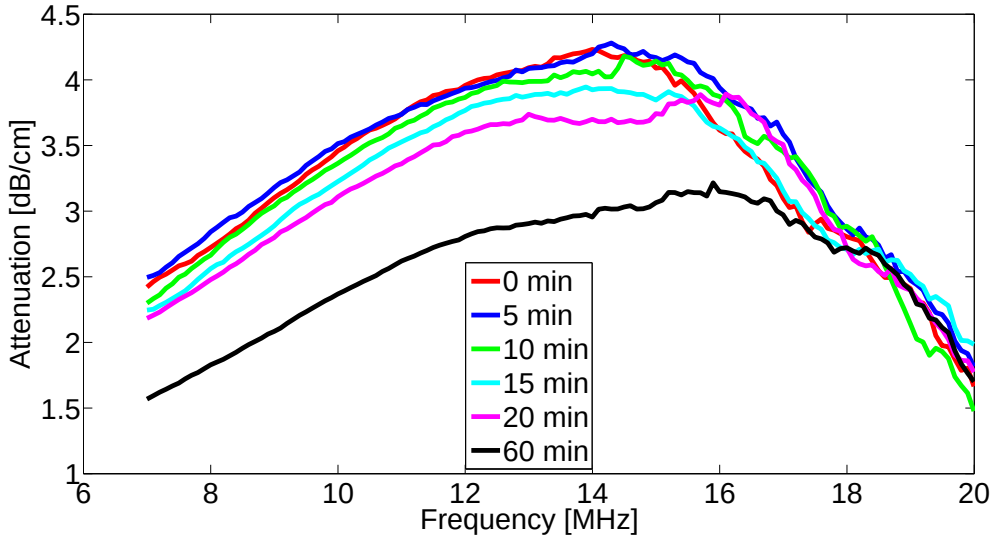


(b) YM-73 BSA small

Figure 4.7: Attenuation spectra of YM-73 microbubbles with (a) larger average diameter (b) smaller average diameter measured every 5 minutes after addition of microbubbles. Red: 0 minutes, blue: 5 minutes, green: 10 minutes, cyan: 15 minutes, magenta: 20 minutes, black: (a) stirred sample, (b) 60 minutes.

## 4.4 Acoustic backscatter

Microbubbles located in an acoustic field are shown to oscillate non-linearly when a large enough pressure is applied [22]. A pronounced effect of this phenomenon is the production of higher harmonics. Measurements of acoustic backscattering at different driving pressures give insight into the non-linear microbubble oscillation, which is not apparent in acoustic attenuation measurements. Three different batches of the nanoparticle-coated microbubbles provided by SINTEF are tested in order to compare how differences in size and different stabilizing proteins affect the backscattering and generation of higher harmonics. In addition, backscattering of a commercial contrast microbubble is measured for comparison.

Microbubble destruction is important both in various medical imaging techniques and in drug delivery. The driving pressure at which destruction takes place is observed as a characteristic change in the receiving spectra with higher noise level and disappearing harmonics.

Single pulses of 20 sine cycles are transmitted into the sample containing the suspended microbubbles of a batch. The power spectral density of the echo generated by a pulse is found, and the spectra from 12 pulses are averaged. Each pulse is separated by at least 2 seconds to reduce correlation effects. Measurements are done at different applied voltages, i.e., different driving pressures. A conversion from voltage to pressure is possible by assuming that the pressure increases linearly with the voltage. The pressure is measured at a specific voltage during the characterization of the transmit transducers. See figure 4.4 and table 4.2. A driving pressure amplitude in the range 5 kPa to 510 kPa is applied.

Three different transmit transducers are used in the experiments: A focused 1 MHz, a focused 3.5 MHz and a flat 5 MHz. The flat 5 MHz transducer is used for receive with both the focused 1 MHz and the focused 3.5 MHz transducer as transmitters. A flat 15 MHz transducer is used for receive with the flat 5 MHz transducer as a transmitter.

In contrast to the attenuation measurements, the measured backscatter spectra depends on the receiving transducer characteristics. The received spectra must therefore be corrected by compensating for the frequency response of the receiving transducer. The frequency response of the flat 5 MHz and the flat 15 MHz transducers are shown in figure 4.3.

### 4.4.1 Higher harmonics and destruction

Two different batches of microbubbles coated and stabilized by YM-73 nanoparticles and Bovine Serum Albumin (BSA) are tested. They were produced with different ultra-turrax velocity, resulting in different average diameter. The size distributions are measured by Coulter Counter and can be found in figure 4.1.

Figure 4.8 shows the corrected spectra received by the flat 5 MHz transducer from ultrasound pulses emitted by the focused 1 MHz transducer for the large YM-73 BSA batch. The applied pressure is specified in each figure. The frequency range is 1 to 10 MHz.

The corresponding spectra for the batch with smaller average diameter are plotted in figure 4.9.

The third batch to be compared is a microbubble stabilized by YM-73 nanoparticles and casein. The size distribution is shown in figure 4.1. Figure 4.10 contains the received

spectra obtained when transmitting with a focused 1 MHz transducer and receiving with a flat 5 MHz transducer.

The Mechanical Index, the ratio between the pressure amplitude and the square root of the transmit frequency, can be easily calculated for 1 MHz pulses and is written in the caption of each figure.

There are several remarks to these spectra. For the YM-73 BSA batch with larger average diameter, at the lowest acoustic pressure applied, only a peak at 1 MHz can be observed. The bubbles oscillate linearly and radiate with the driving frequency. When the pressure is increased to 15 kPa, more energy is radiated and the peak height rises. Linear oscillations dominate, but a small second harmonic peak can be glimpsed. As the driving pressure reaches 30 kPa, higher harmonics, included the fifth, are visible. The second harmonic is about 15 dB lower than the fundamental. The oscillations are now in the non-linear regime. At 60 kPa, peaks at still higher harmonics emerge. At least 9 harmonics can be counted. Higher pressure increases the power, but more at the harmonics than at the fundamental. At 170 kPa, the background noise has risen considerably. Smaller peaks between the harmonics, possible ultraharmonics, can be perceived. As the pressure further increases, the height of the peaks with respect to the background noise reduces. With an applied driving pressure of 510 kPa, all peaks are destroyed, with exception of a barely recognized fundamental and second harmonic. Apparently, the microbubbles start to collapse at 170 kPa, corresponding to $MI = 0.17$, and almost all of them are destructed at 510 kPa ($MI = 0.51$).

Similar observations can be seen for the batch with smaller average diameter. As with the larger average diameter batch, only the fundamental at 1 MHz is clearly visible at 5 kPa and 15 kPa. At 30 and 60 kPa, higher harmonics are emerging, but the number of peaks is less than for the batch with larger average diameter. At the higher applied driving pressure, 340 and 510 kPa, there is an pronounced difference between the batches. The batch with smaller diameter bubbles have higher peaks with respect to the noise level, and all the peaks are still perceptible even at 510 kPa. The amount of destruction is therefore presumingly less.

The microbubbles with casein as surfactant protein oscillate linearly at 5 kPa with a single peak at the fundamental. This is similar to the BSA microbubble. At 15 kPa, more peaks are observed. Unexpectedly, at 30 kPa, the received power is reduced, and the number of harmonics is not higher at 60 kPa. These observations are in contrast to the microbubble stabilized by BSA, where the fundamental dominates at 15 kPa, and 6-9 harmonics are noticeable at 60 kPa. It is thus possible that the batch containing casein produces harmonics at lower pressures. At 90 kPa, the appearance of the spectra is again similar. Compared to the large BSA microbubbles, the casein microbubbles become more noisy at 170 kPa ($MI = 0.17$). The highest harmonics are destroyed, and potential ultraharmonics are more pronounced. The difference continues at 230 kPa ($MI = 0.23$). At 340 kPa ($MI = 0.34$), there is evidently large destruction. The same degree of destruction is seen with the BSA microbubbles first at 510 kPa. It is therefore likely that microbubbles with casein are destroyed at lower pressures than those with BSA.

For comparison, backscattering is measured of a sample of a commercial HEPS-Na/PFB microbubble. The power density spectra are shown in figure 4.11. Already

at 5 kPa, peaks at the second and third harmonic are present. Higher harmonics (up to six or seven) emerge at 15 kPa, while at 30 kPa, the noise level increases more than the power of the peaks. Further enhancement of the pressure results in increase of power of the higher harmonics with only small changes in the fundamental. At 90 kPa, several harmonics (at least nine) are clearly observable, and ultraharmonics become visible. The noise level starts to increase and rises further as the pressure amplitude gets higher. At 510 kPa, various harmonics have disappeared. The most distinct characteristic of this microbubble compared to the microbubbles stabilized by polymeric YM-73 nanoparticles, appears from these results to be a lower pressure threshold for the initiation of radiation containing higher harmonics.

Backscatter spectra from large and small YM-73 BSA microbubbles are also received with a 15 MHz transducer after transmitting with a 5 MHz transducer. The obtained spectra are shown in figure 4.12. These measurements are performed to observe if ultrasound transmitted with frequency closer to the resonance frequency may induce destruction at lower mechanical index. The pressure amplitudes are 170 kPa ($MI = 0.08$), 340 kPa, ($MI = 0.15$) and 510 kPa ($MI = 0.23$).

There are similarities between the spectra from the large and the small microbubbles. For both batches, three harmonics are already present at 170 kPa, and the fourth harmonic emerge at 340 kPa. Increasing the pressure enhances the power of the higher harmonics more than the fundamental. The noise level increases with larger pressure, but there is no evidents for mayor destruction at 510 kPa. The ratio between the power at the higher harmonics and at the fundamental is somewhat higher for the large compared to the small BSA microbubbles.

**Subharmonics and ultraharmonics**

In order to better detect potential subharmonics and ultraharmonics, the transmit frequency is changed to 3.5 MHz. Backcsattering is received with the flat 5 MHz from samples with microbubbles stabilized by YM-73 nanoparticles and the proteins BSA and casein. Spectra in figure 4.13 show the received scattering from the large BSA microbubbles and casein microbubbles.

At 10 kPa, both batches display a peak only at the driving frequency $f_i$, 3.5 MHz. Increasing the pressure to 90 kPa and 170 kPa, the fundamental grows, and the second harmonic starts to get visible. For the casein microbubbles, some peaks seem to appear at various other frequencies, including the subharmonic at 1.75 MHz (1/2 $f_i$). These peaks have, however, vanished at 520 kPa. No significant differences are observable between the batches at 520 kPa pressure amplitude. At 1040 kPa, both the BSA as well as the casein microbubles radiate subharmonic at 1.75 MHz (1/2 $f_i$). In addition, ultraharmonic at 5.25 MHz (3/2 $f_i$) has emerged. The peaks in the received spectrum from microbubbles stabilized by casein appear more pronounced and with higher power. By further enhancing the pressure to 1560 kPa, the spectrum of the batch with casein proteins loses its subharmonics and ultraharmonics as the noise level continues to increase. This is in difference to the spectrum from BSA-stabilized microbubbles. The noise level is lower, and various peaks are perceptible. Including the suharmonic 1/2 $f_i$ and the ultraharmonic 3/2 $f_i$, two ultraharmonics at approximately 4.4 MHz (possibly 5/4 $f_i$) and 8.75 MHz (5/2 $f_i$) have emerged.

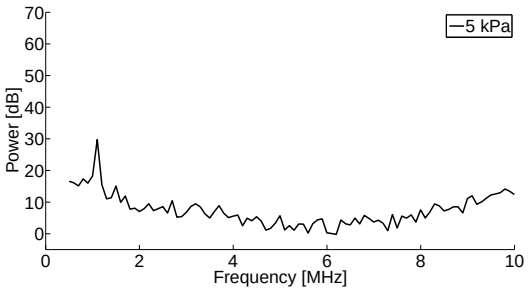


(a) 5 kPa, $MI = 0.005$

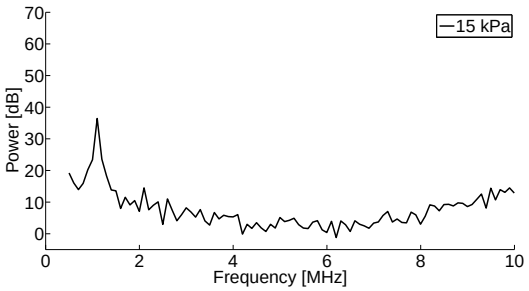


(b) 15 kPa, $MI = 0.015$

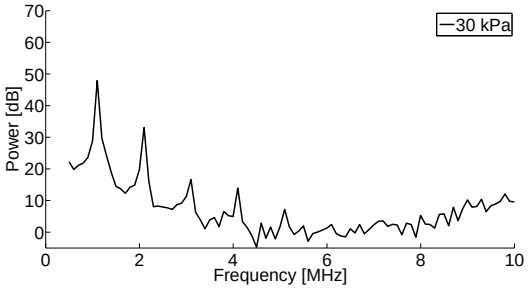


(c) 30 kPa, $MI = 0.03$

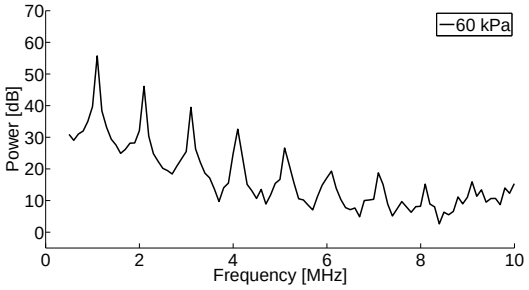


(d) 60 kPa, $MI = 0.06$

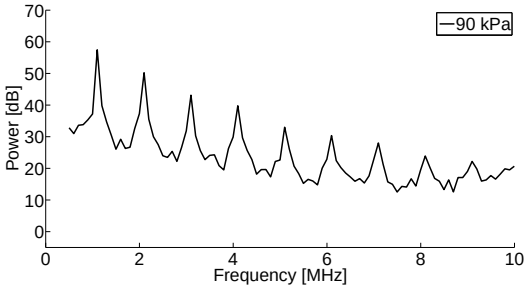


(e) 90 kPa, $MI = 0.09$

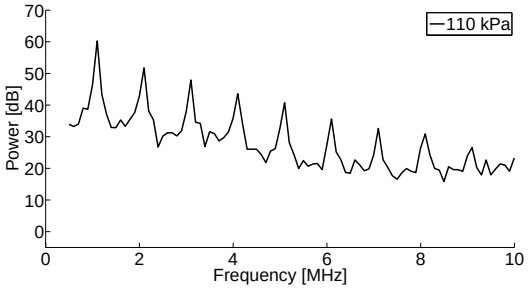


(f) 110 kPa, $MI = 0.11$

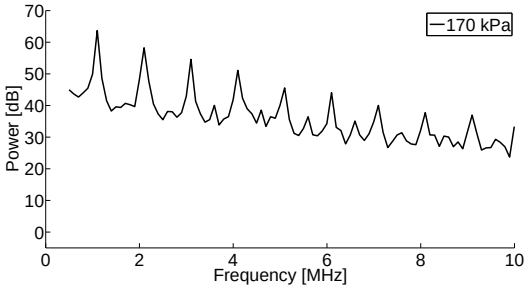


(g) 170 kPa, $MI = 0.17$

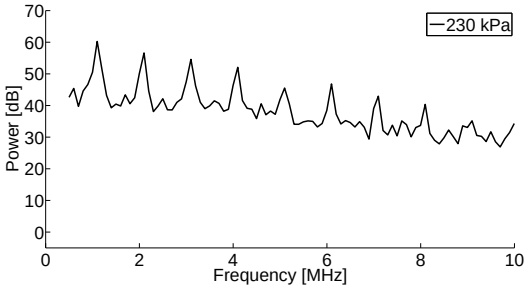


(h) 230 kPa, $MI = 0.23$

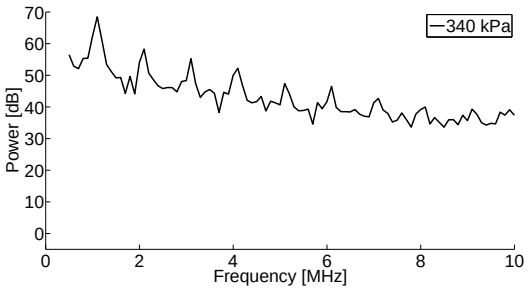


(i) 340 kPa, $MI = 0.34$

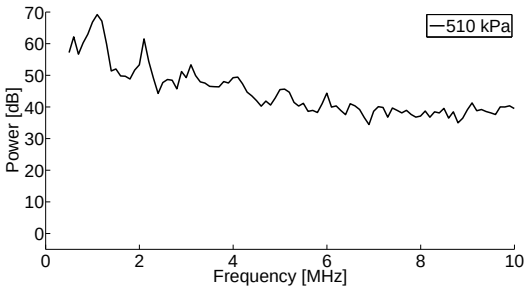


(j) 510 kPa, $MI = 0.51$

Figure 4.8: Scattering spectra received by a 5 MHz transducer for large YM-73 BSA microbubbles. Ultrasound pulses, each consisting of 20 sine cycles, are transmitted by a 1 MHz transducer at acoustic pressures in the range 5-510 kPa. Each plotted spectrum is an average of the spectra obtained from 12 successive single pulses sent at time intervals 2-5 seconds.

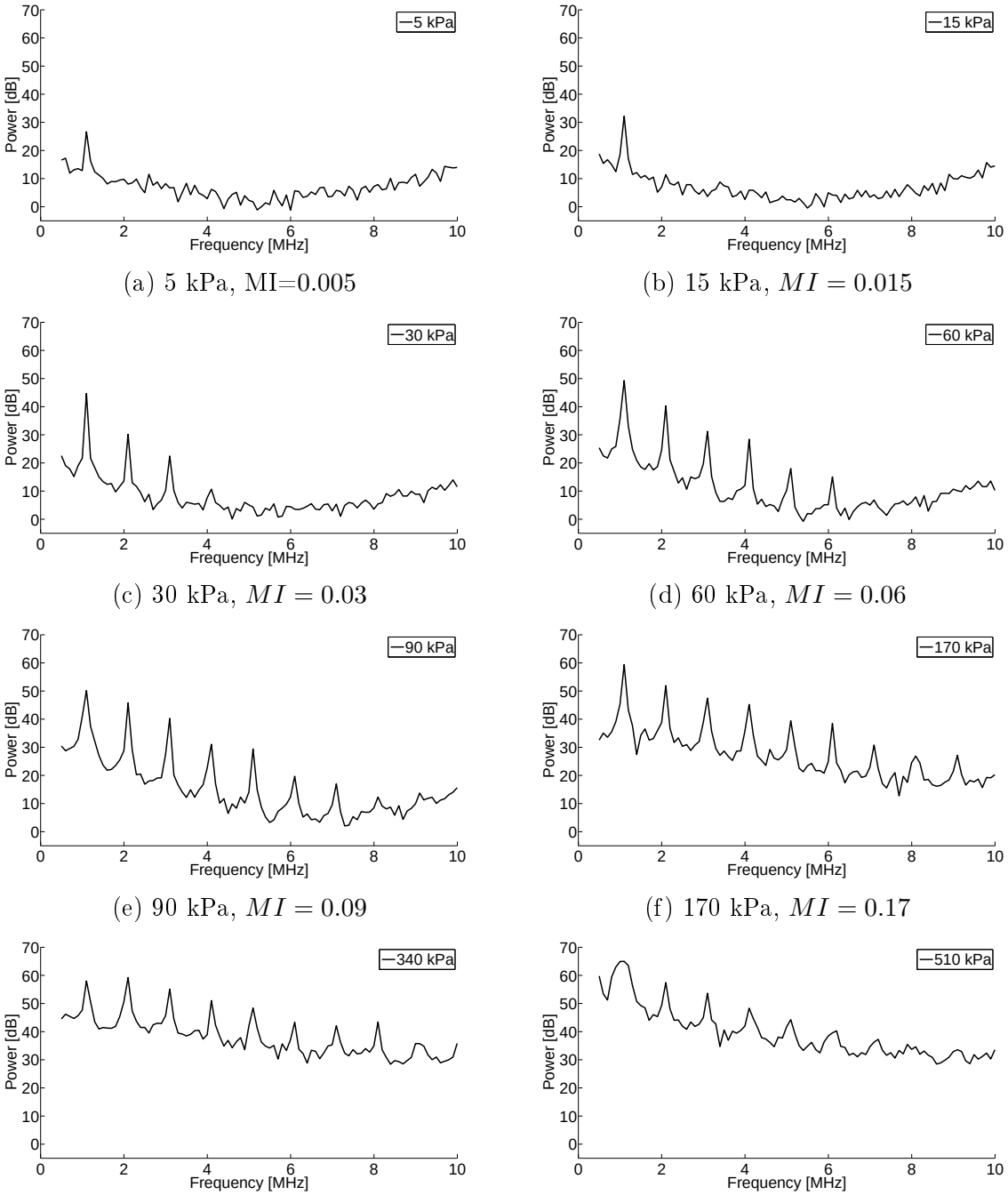


(a) 5 kPa, MI=0.005

(b) 15 kPa, $MI = 0.015$

(c) 30 kPa, $MI = 0.03$

(d) 60 kPa, $MI = 0.06$

(e) 90 kPa, $MI = 0.09$

(f) 170 kPa, $MI = 0.17$

(g) 340 kPa, $MI = 0.34$

(h) 510 kPa, $MI = 0.51$

Figure 4.9: Scattering spectra received by a 5 MHz transducer for small YM-73 BSA microbubbles. Ultrasound pulses, each consisting of 20 sine cycles, are transmitted by a 1 MHz transducer at acoustic pressures in the range 5-510 kPa. Each plotted spectrum is an average of the spectra obtained from 12 successive single pulses sent at time intervals 2-5 seconds. No measurements are done at 110 and 230 kPa.

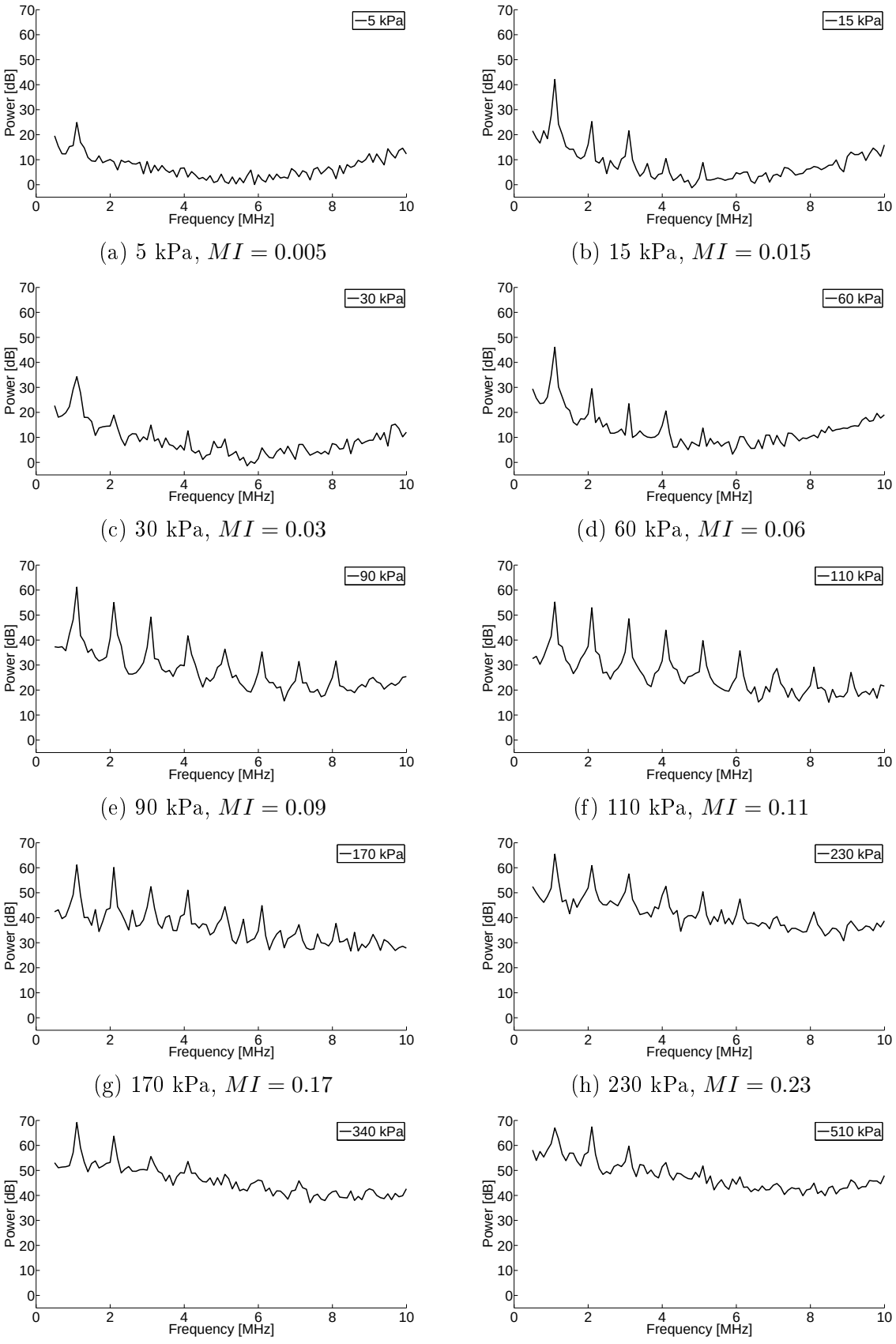


(a) 5 kPa, $MI = 0.005$

(b) 15 kPa, $MI = 0.015$

(c) 30 kPa, $MI = 0.03$

(d) 60 kPa, $MI = 0.06$

(e) 90 kPa, $MI = 0.09$

(f) 110 kPa, $MI = 0.11$

(g) 170 kPa, $MI = 0.17$

(h) 230 kPa, $MI = 0.23$

(i) 340 kPa, $MI = 0.34$

(j) 510 kPa, $MI = 0.51$

Figure 4.10: Scattering spectra received by a 5 MHz transducer for YM-73 casein microbubbles. Ultrasound pulses, each consisting of 20 sine cycles, are transmitted by a 1 MHz transducer at acoustic pressures in the range 5-510 kPa. Each plotted spectrum is an average of the spectra obtained from 12 successive single pulses sent at time intervals 2-5 seconds.

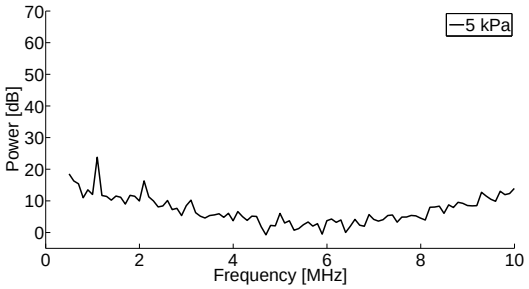


(a) 5 kPa, $MI = 0.005$

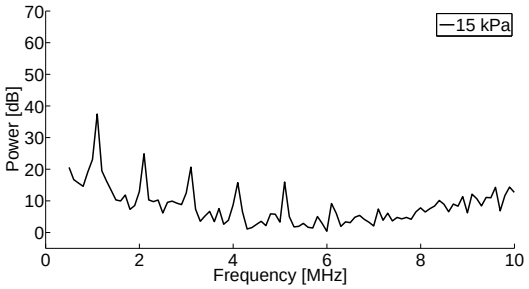


(b) 15 kPa, $MI = 0.015$

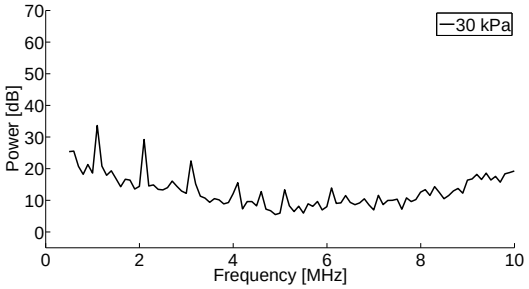


(c) 30 kPa, $MI = 0.03$

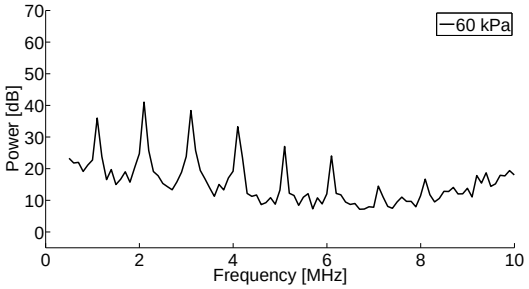


(d) 60 kPa, $MI = 0.06$

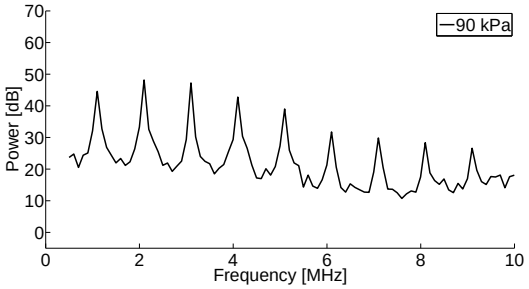


(e) 90 kPa, $MI = 0.09$

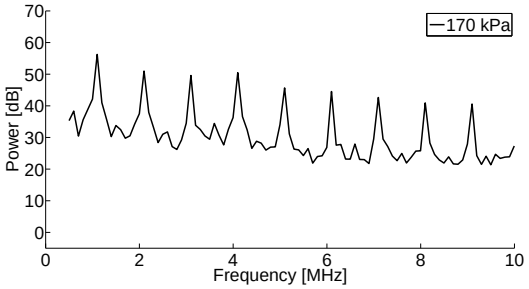


(f) 170 kPa, $MI = 0.17$

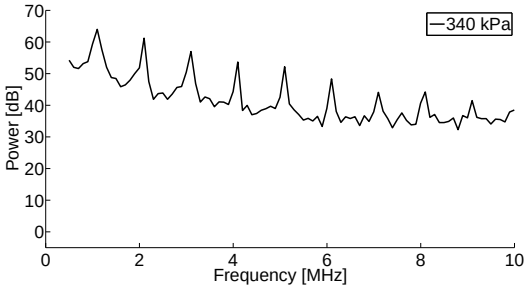


(g) 340 kPa, $MI = 0.34$

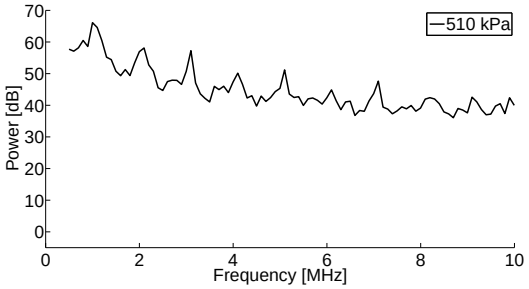


(h) 510 kPa, $MI = 0.51$

Figure 4.11: Scattering spectra received by a 5 MHz transducer for a suspension of HEPS-Na/PFB microbubbles. Ultrasound pulses, each consisting of 20 sine cycles, are transmitted by a 1 MHz transducer at acoustic pressures in the range 5-510 kPa. Each plotted spectrum is an average of the spectra obtained from 12 successive single pulses sent at time intervals 2-5 seconds. There are no measurements at 110 and 230 kPa.

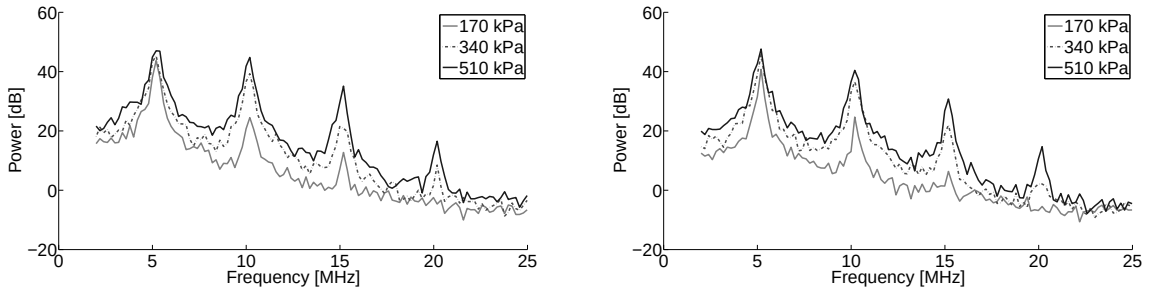


(a) YM-73 BSA large (b) YM-73 BSA small

Figure 4.12: Scattering spectra received by a 5 MHz transducer for (a) large and (b) small YM-73 BSA microbubbles. Ultrasound pulses, each consisting of 20 sine cycles, are transmitted by a 5 MHz transducer at acoustic pressures in the range 170-510 kPa. Each plotted spectrum is an average of the spectra obtained from 12 successive single pulses.

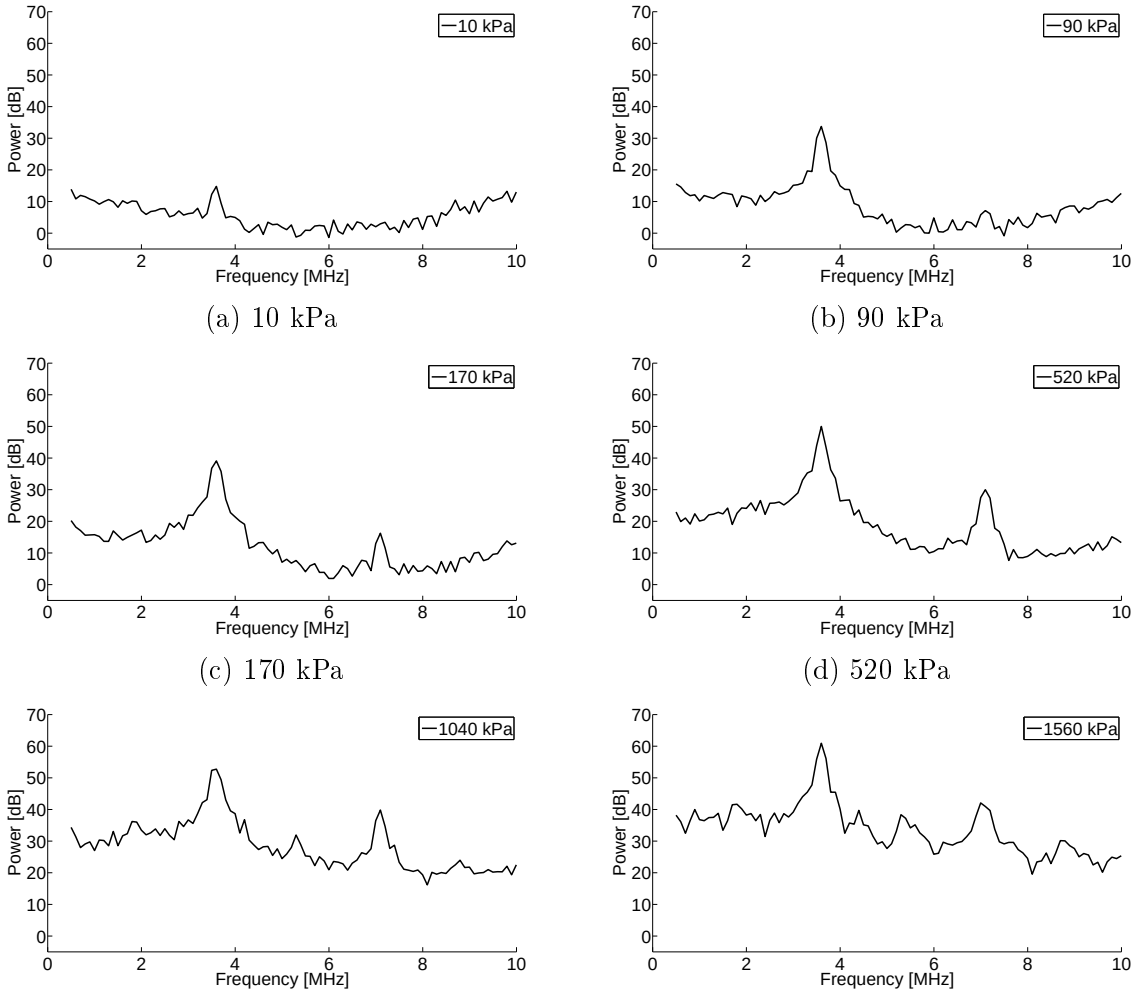


(a) 10 kPa (b) 90 kPa

(c) 170 kPa (d) 520 kPa

(e) 1040 kPa (f) 1560 kPa

Figure 4.13

## 4.5 Ultrasound imaging of microbubbles

Ultrasound imaging of two different YM-73 microbubbles, stabilized by either casein and BSA proteins, can provide insight into functional properties given by the protein. Images

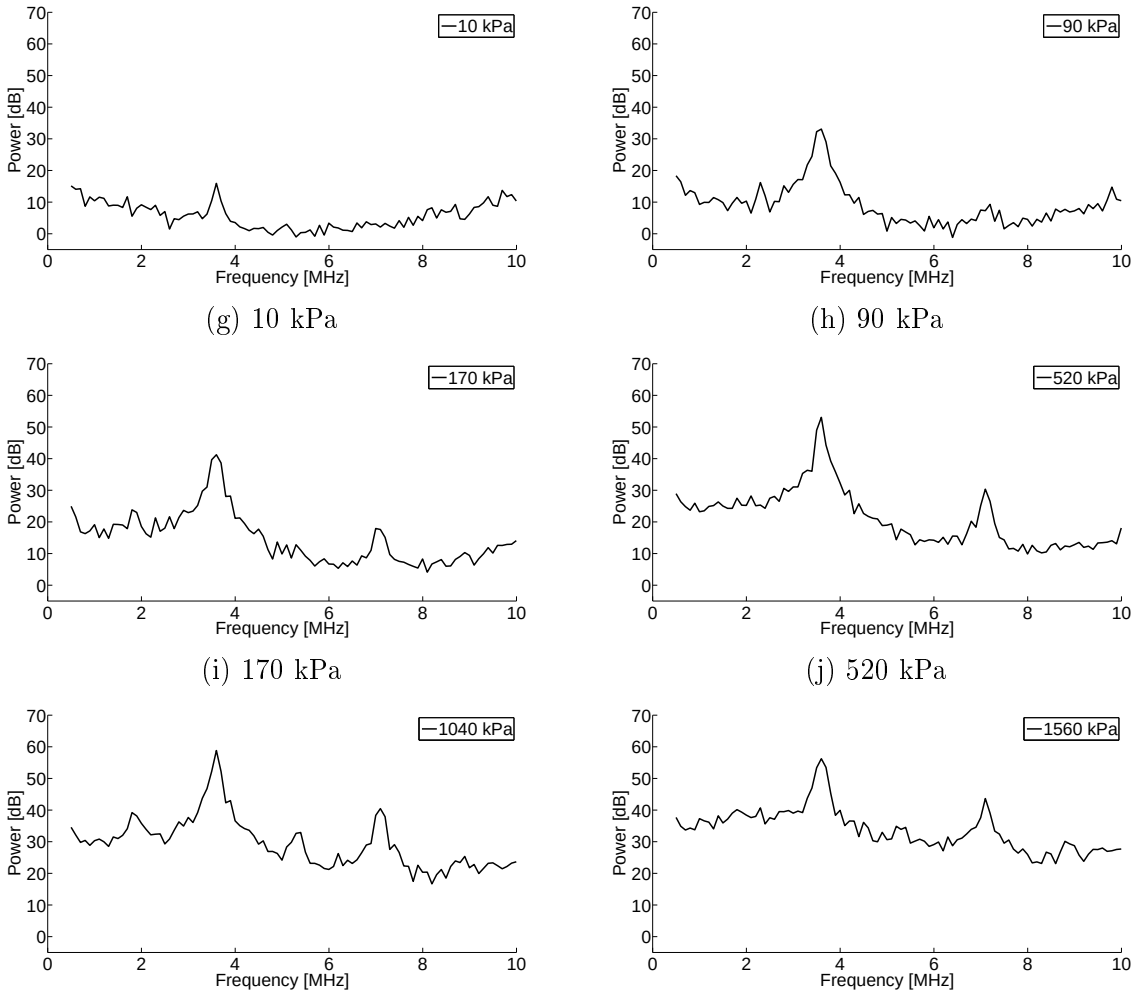


(g) 10 kPa (h) 90 kPa

(i) 170 kPa (j) 520 kPa

(k) 1040 kPa (l) 1560 kPa

Figure 4.13: Scattering spectra received by a 5 MHz transducer for (a)-(f) large YM-73 BSA microbubbles and (g)-(l) YM-73 casein microbubbles. Ultrasound pulses, each consisting of 20 sine cycles, are transmitted by a 3.5 MHz transducer at acoustic pressures in the range 10-1560 kPa. Each plotted spectrum is an average of the spectra obtained from 12 successive single pulses sent at time intervals 2-5 seconds.

of the microbubbles with BSA and casein are shown in figure 4.14 and figure 4.15, respectively. The transmit frequency is 3.6 MHz, and the receive frequency is 7.2 MHz. The images are shown with inverted colors for better contrast.

Black spots located between the two black lines in the middle represent microbubbles. Microbubbles with both type of proteins are visible at MI 0.05, but bubbles with casein appear to scatter more strongly. Unfortunately, a higher concentration of casein microbubbles has been added, making comparison more inconvenient. The number of BSA microbubbles are merely constant up to MI 0.15. At MI 0.18, there is a small reduction. This indicates that destruction has begun. At MI 0.23, more bubbles are lost, and at MI 0.33, the destruction seems to be almost complete. For the casein microbubbles, a reduction of black spots can be observed from MI 0.16 to MI 0.18. At MI 0.23, a significant larger fraction of casein microbubbles are vanished, compared to the fraction of lost BSA microbubbles at same MI. Figure 4.15 includes an image of MI 0.20 instead of MI 0.33 because the destruction appears to initiate at lower MI for microbubbles with

casein protein.

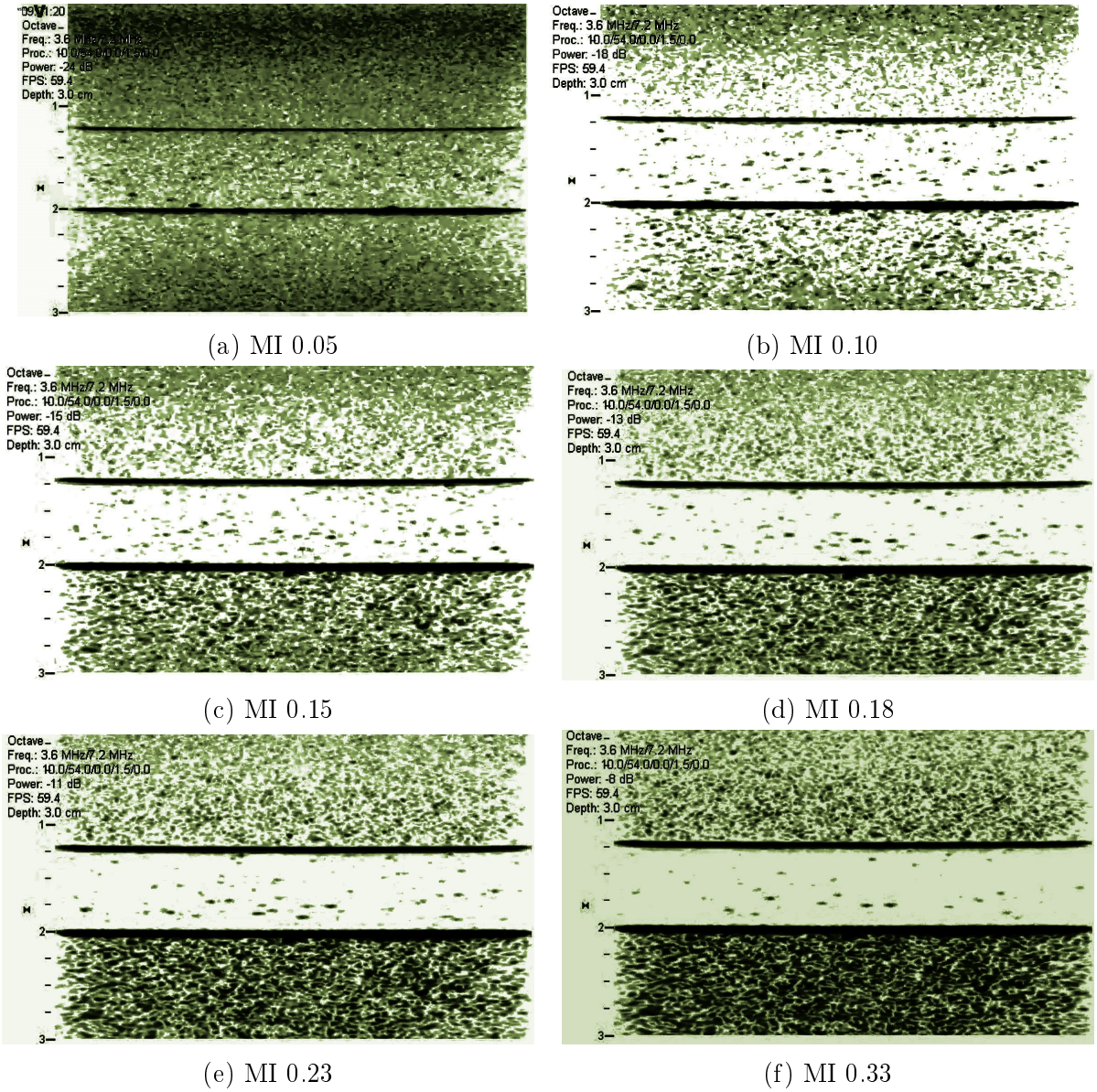


(a) MI 0.05

(b) MI 0.10

(c) MI 0.15

(d) MI 0.18

(e) MI 0.23

(f) MI 0.33

Figure 4.14: Ultrasound images acquired by pulse inversion imaging of YM-73 BSA microbubbles flowing through a pipe in a phantom tissue. The images are acquired at different applied pressure, and each image is labeled with the corresponding Mechanical Index (MI)

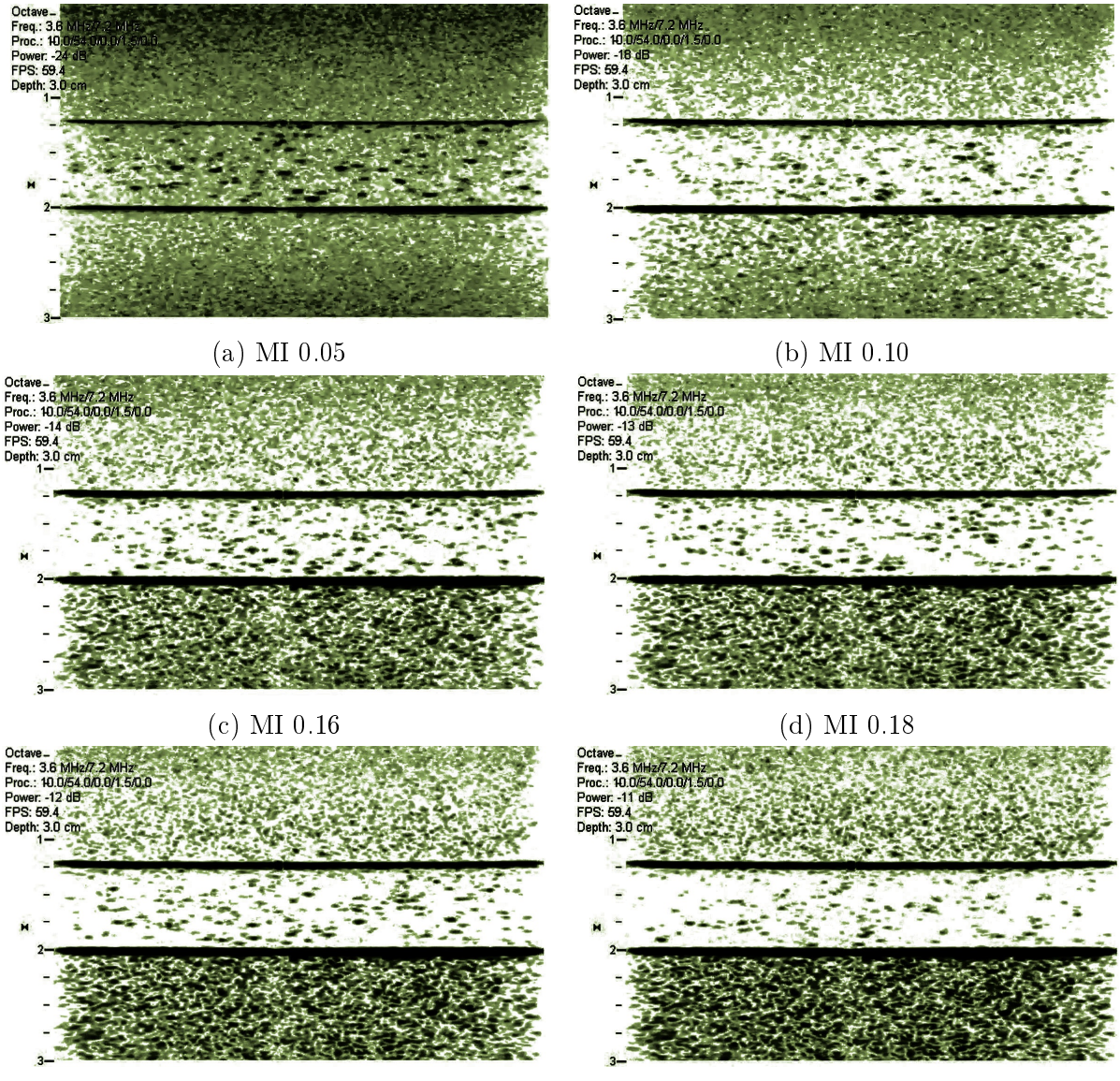


(a) MI 0.05 (b) MI 0.10

(c) MI 0.16 (d) MI 0.18

(e) MI 0.20 (f) MI 0.23

Figure 4.15: Ultrasound images acquired by pulse inversion imaging of YM-73 casein microbubbles flowing through a pipe in a phantom tissue. The images are acquired at different applied pressure, and each image is labeled with the corresponding Mechanical Index (MI).

## 4.6 Mechanical properties of microbubbles using AFM

A second approach to study and characterize the microbubbles is to perform compression with atomic force microcopy (AFM). Three different batches of microbubbles provided by SINTEF are characterized. They differ in the nanoparticle type and the stabilizing protein. One is stabilized by YM-44 nanoparticles and BSA, and the two others are both stabilized by YM-73 nanoparticles and either BSA or casein.

### 4.6.1 Immobilized microbubbles

It is required that the microbubbles are fixed to the surface. The method applied to immobilize microbubbles were successful, and bubbles were observed to be attached for several hours. Typical immobilized microbubbles from the three batches are shown in figure 4.16. The images 4.16a, 4.16b and 4.16c are formed by the emitted light from the fluorophore Nile Red encapsulated in YM-44- nanoparticles. 4.16d, 4.16e and 4.16f show images of YM-73 BSA microbubbles. These images are acquired by transmitted light and have a different focus. The white centers indicate gas cores. 4.16d includes the cantilever. Images 4.16h, 4.16g and 4.16i are of microbubbles stabilized by YM-73 and casein. These bubbles are imaged by a newer microscope, and the images appear less blurred. Different sizes are easily recognized.

### 4.6.2 Estimation of the Young's modulus of the microbubble shell

The compression of the microbubbles results in force-deformation curves, with representative curves presented in the next section. The initial linear region of the curve is determined, and the slope of the curve in this region is used in calculation of the Young's modulus of the microbubble shell with the Reissner theory.

The Reissner theory requires estimation of various parameters. The diameter of the microbubbles are obtained from images taken of each bubble before compression. The number of pixels per micrometer is known, and the bubble diameter is measured in pixels and converted to micrometer. The thickness cannot be determined from the images, as the resolution is too low. Common estimations are 1-2 nanoparticle layers. In this work, the thickness $t = 150$ nm is used, corresponding to approximately one layer of nanoparticles. The shell thickness is further assumed to be constant and independent of the bubble diameter. The Poisson's ratio has not been measured and is assumed to be $\nu = 0.4$, which is a value used by Schmidt *et al.*. for microbubbles coated with a different type of PBCA nanoparticles [58].

Compressions are done on 18-23 microbubbles for each batch. Some bubbles are compressed several times. Because of the possibility that the microbubble is damaged during compression, it was decided that the Young's modulus should only be calculated from the first or the second obtained force-curve. The YM-44 microbubbles are compressed with cantilevers having measured spring constant 1.06 N/m and 1.95 N/m. Cantilevers with measured spring constant 2.08 N/m and 1.26 N/m are used for the YM-73 BSA microbubbles, while for the YM-73 casein microbubbles, the spring constant of the cantilever is measured to be 2.42 N/m.

Figure 4.17 shows a scatter plot of the calculated Young's modulus using Reissner theory of each compressed microbubble from the three batches. There is a wide range of values, still they are restricted to the same order of magnitude. A correlation between the Young's modulus and the bubble diameter is noticeable. A linear regression is performed

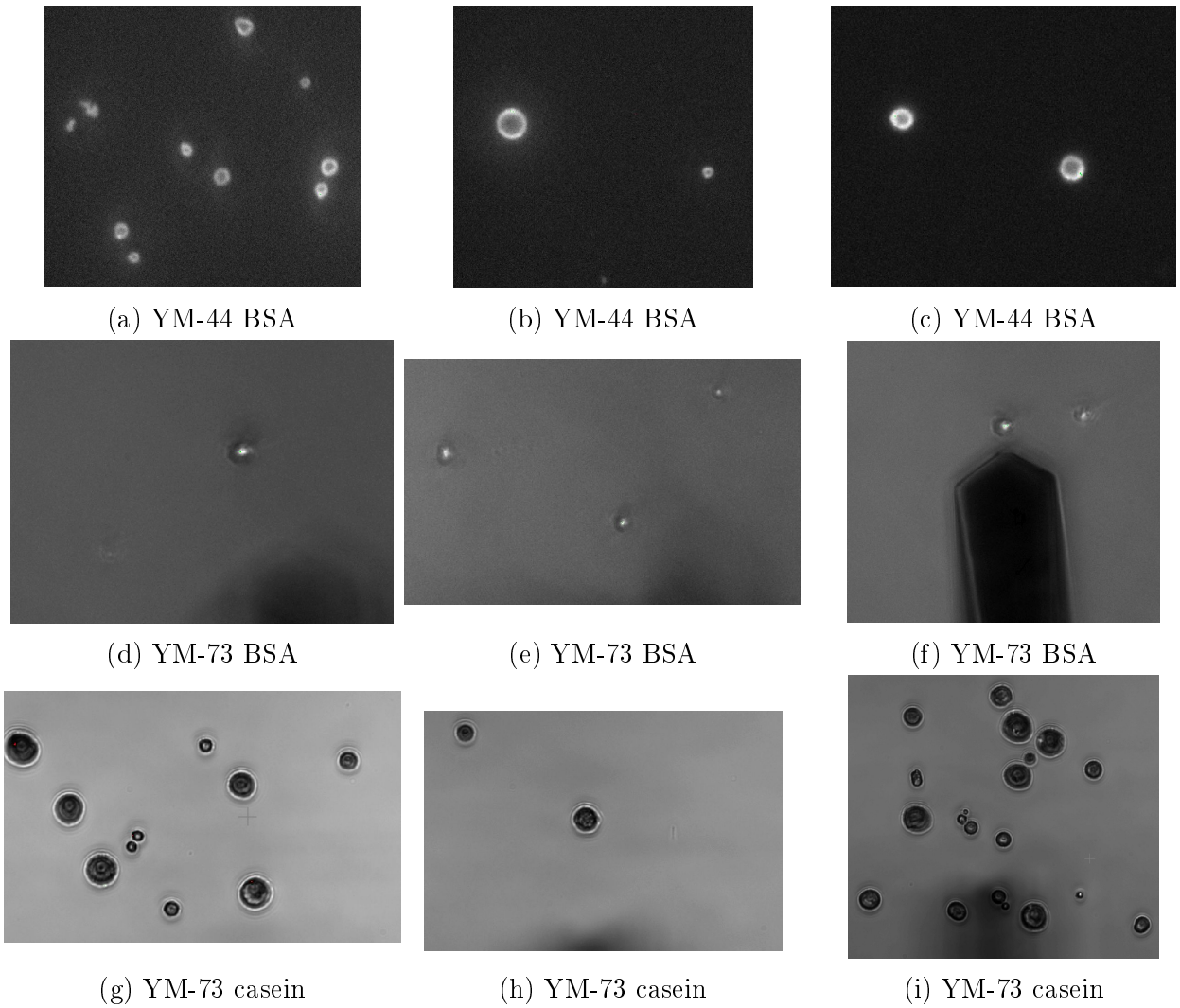

(a) YM-44 BSA (b) YM-44 BSA (c) YM-44 BSA

(d) YM-73 BSA (e) YM-73 BSA (f) YM-73 BSA

(g) YM-73 casein (h) YM-73 casein (i) YM-73 casein

Figure 4.16: Typical images of microbubbles taken by the microscope mounted to the AFM Bioscope.

and shown in figure 4.18. A t-test of the slope is done to investigate whether there is a significant linear relationship with 95 % confidence. The null hypothesis is that there is no dependence, i.e, the slope $\beta = 0$, and the alternative hypothesis that $\beta > 0$.

### YM-44 BSA

The microbubbles stabilized by YM-44 and BSA have Young's modulus of the shell in the range 10-37 MPa. The average value is $22 \pm 7.6$ MPa. The average bubble diameter is $3.9 \pm 1.3$ μm. A linear regression gives an estimated linear equation $E = 1.2D + 17$. $E$ is the Young's modulus in MPa, and $D$ is the diameter in μm. The t-test reveals a p-value of 0.38. This is larger than 0.05 and the null hypothesis cannot be rejected. Hence, there is no significant linear relationship.

### YM-73 BSA

The Young's modulus of the shell of YM-73 BSA microbubbles are in the range 7-35 MPa. The average value is $15 \pm 7.8$ MPa. The average bubble diameter is $5.6 \pm 1.3$ μm.

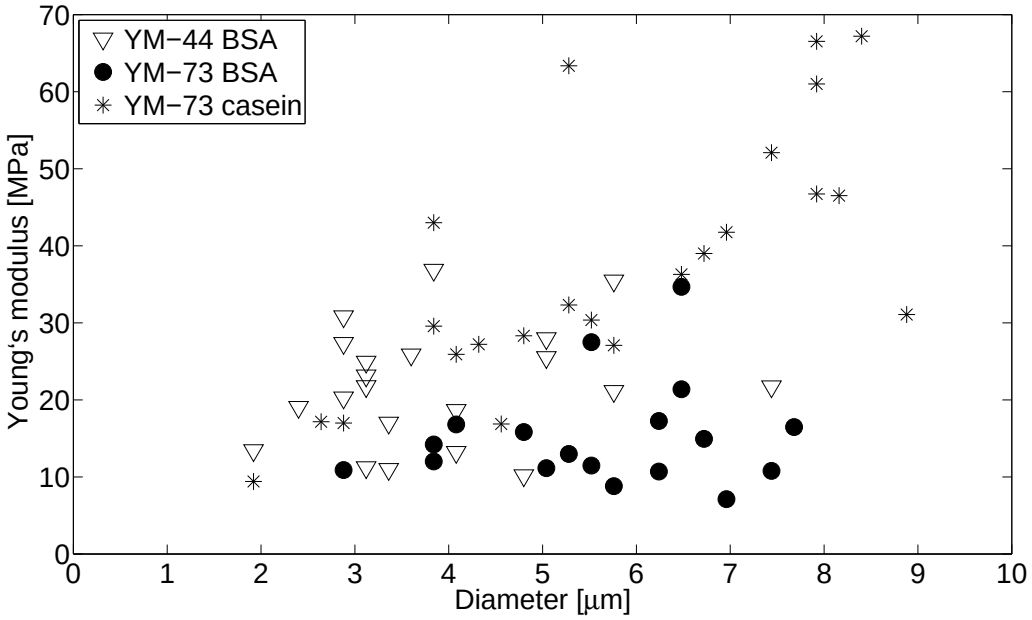


Figure 4.17: The estimated Young's modulus of the microbubble shell obtained by Reissner theory of microbubbles from the batch with YM-44 nanoparticles and BSA (triangles), YM-73 nanoparticles and BSA (solid spheres), YM-73 nanoparticles and casein (stars).

The equation obtained by linear regression is $E = 0.7D + 11$. A t-test of the slope is performed, and the p-value is 0.58. There is no significant linear relationship with 95 % confidence.

### YM-73 casein

The range 9-67 MPa is observed for the Young's modulus of the shell of YM-73 casein microbubbles. The average value is 37±17 MPa. The average bubble diameter is 5.7±2.0 µm. Linear regression gives an estimated linear equation $E = 6.0D + 3.0$. A t-test of the slope results in p-value 0.000078. As this is smaller than 0.05, the null hypothesis can be rejected, and there is a significant linear relationship with more than 95 % confidence.

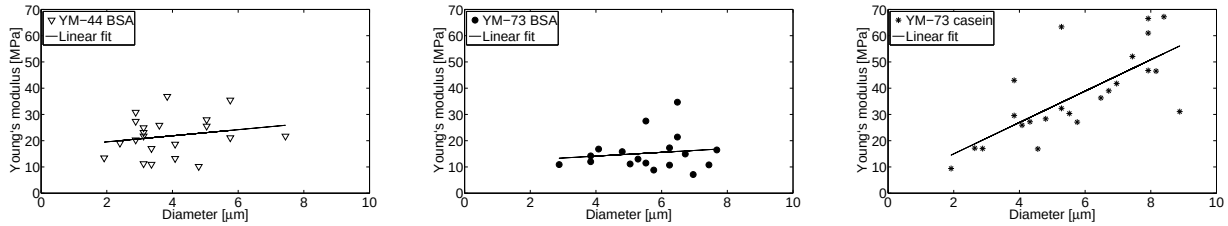


(a) YM-44 BSA (b) YM-73 BSA (c) YM-73 casein

Figure 4.18: Scatter plots of the estimated Young's modulus of the shell of each compressed microbubble from a batch. A linear regression is performed, and the linear fit plotted.

### 4.6.3 Behavior of microbubbles during compression

Representative force curves obtained by the first compression of a microbubble are given in figures 4.19, 4.20 and 4.21. The first column shows force versus the separation between the cantilever and the position of maximum force. The blue curve is the approaching curve, while the red is the retracting curve. The second column shows force as a function of relative deformation. The linear regions used in the calculation of the Young's moduli are included. The force curves from four different microbubbles from each batch are shown.

There is a large variety between the curves, but some general characteristics can be observed. The force-separation curves consist of an part with no measured force changes where the cantilever is approaching the bubble. When contact is achieved, an initial non-linear part is seen. This part can be relatively large, as in figure 4.20e and 4.19c, or smaller as in figure 4.19a. Thereafter follows the linear regime. A region is here assumed to be linear if the coefficient of determination $R^2$ is above 0.995. The length and the slope of the linear region varies greatly, also for microbubbles of the same batch. The next part is the non-linear part with irregular behavior and abrupt breaks. This happens for most of the microbubbles around 50-100 nN applied load. However, the curve in the figure 4.19a remains approximately linear up to 300 nN. The non-linear part consists of a plateau phase where small or no amount of force is necessary to cause further deformation. Eventually and abruptly, the slope increases. The approaching and retracting curves do not overlap. This hysteresis is observed for all bubbles, but increases with higher load, comparing figure 4.20a with 4.20g.

For the batch containing microbubbles with shells of YM-73 and casein, the amount of applied force necessary to cause a relative deformation of 0.15 is in the range 300-450 nN. The microbubbles stabilized by BSA and either YM-73 or YM-44 can be deformed to this fraction already at 100 nN (figure 4.19g and figure 4.20c).

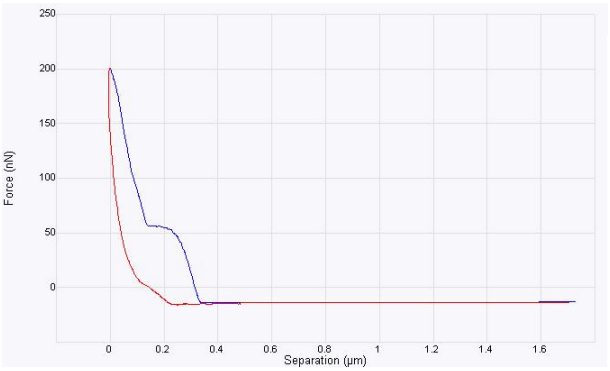


(a) Force-separation

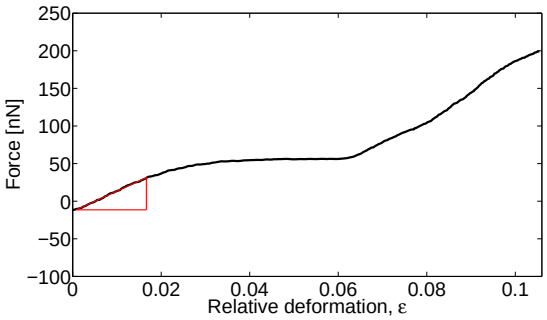


(b) Force-relative deformation

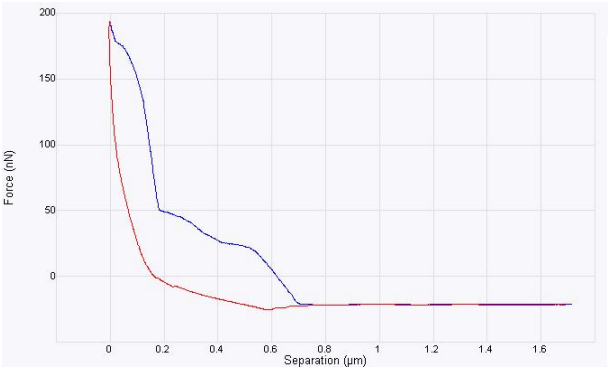


(c) Force-separation

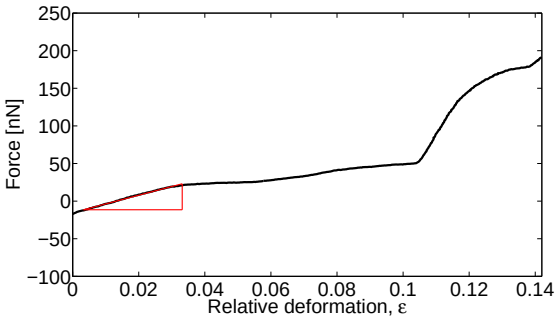


(d) Force-relative deformation

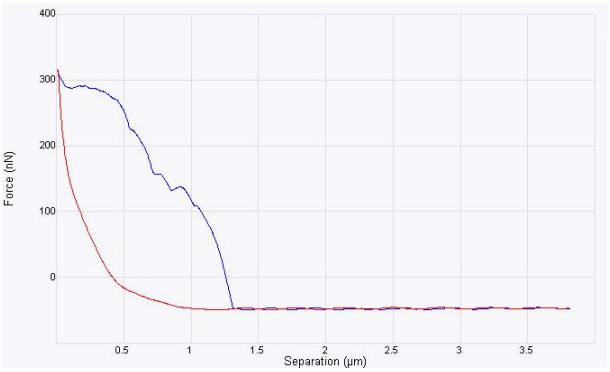


(e) Force-separation

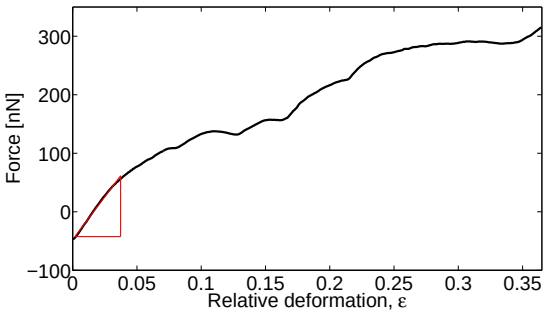


(f) Force-relative deformation

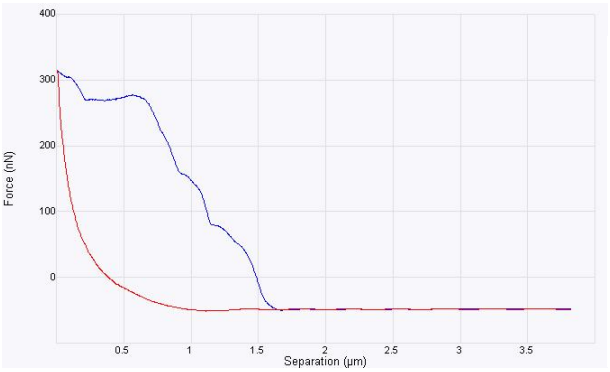


(g) Force-separation

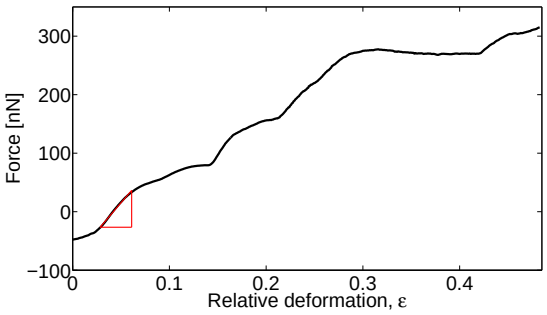


(h) Force-relative deformation

Figure 4.19: Force-separation curves and force-relative deformation curves obtained from a selection of compressed microbubbles stabilized by YM-44 and BSA

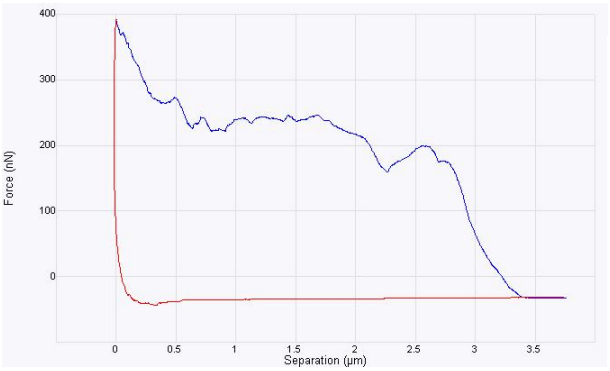


(a) Force-separation

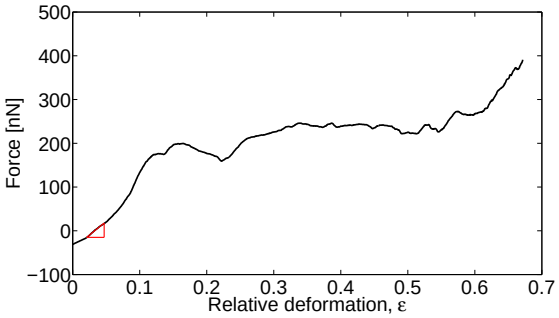


(b) Force-relative deformation

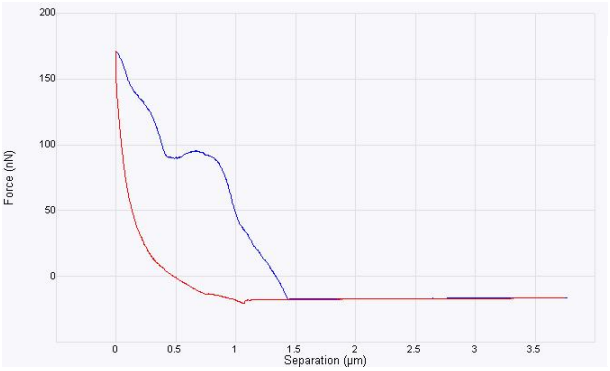


(c) Force-separation

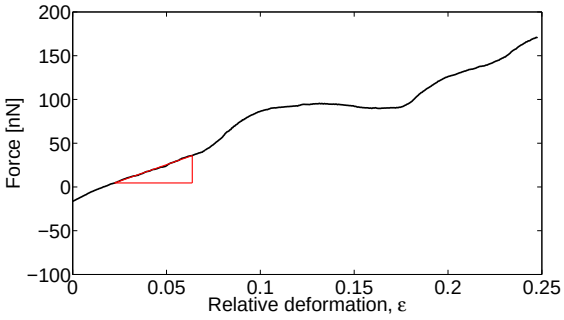


(d) Force-relative deformation

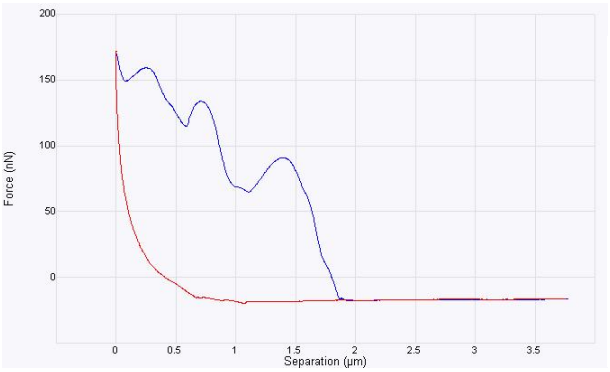


(e) Force-separation

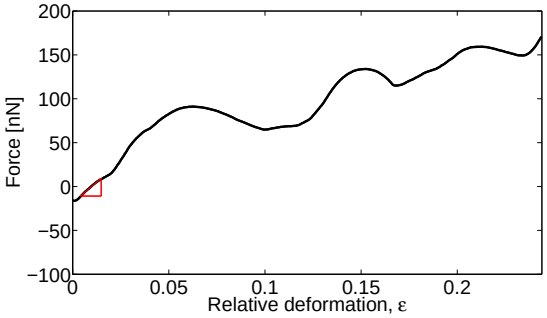


(f) Force-relative deformation

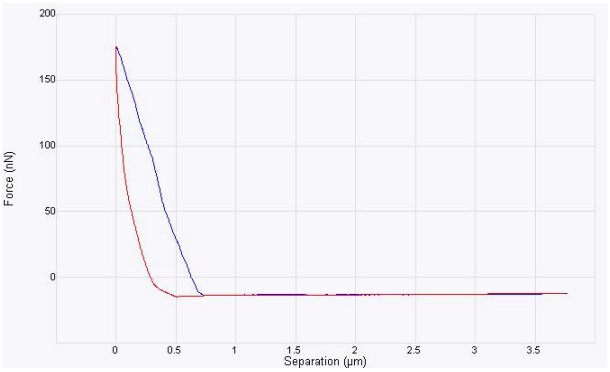


(g) Force-separation

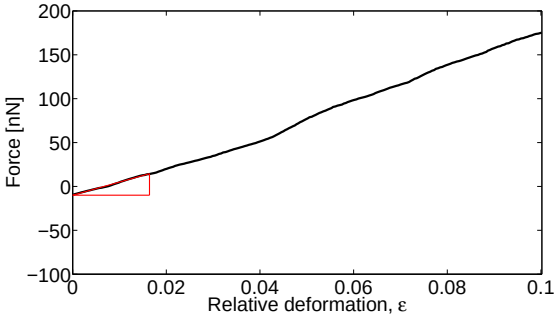


(h) Force-relative deformation

Figure 4.20: Force-separation curves and force-relative deformation curves obtained from a selection of compressed microbubbles stabilized by YM-73 and BSA

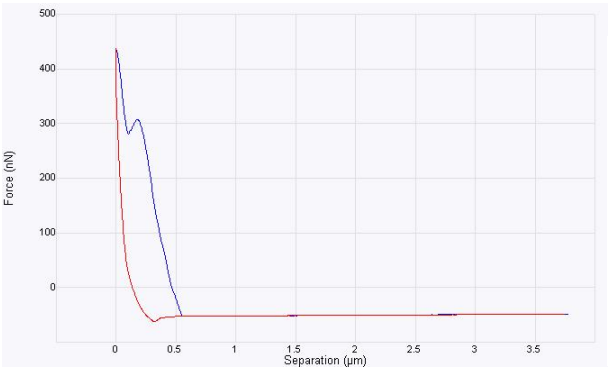


(a) Force-separation

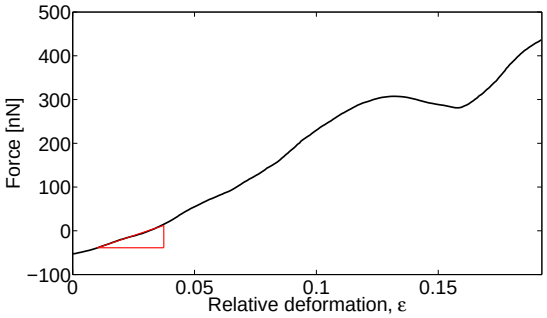


(b) Force-relative deformation

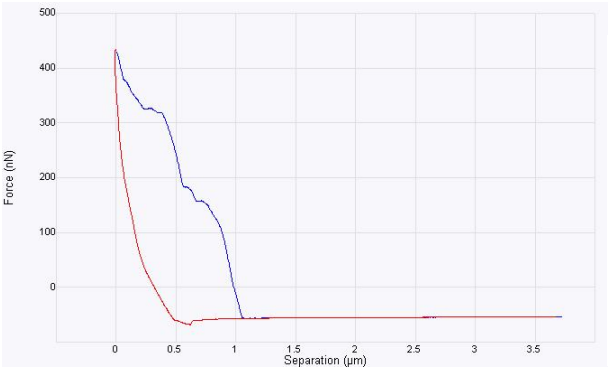


(c) Force-separation

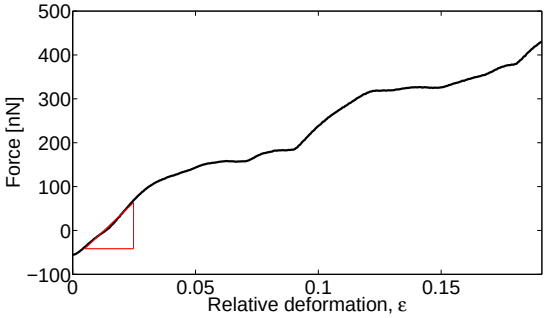


(d) Force-relative deformation

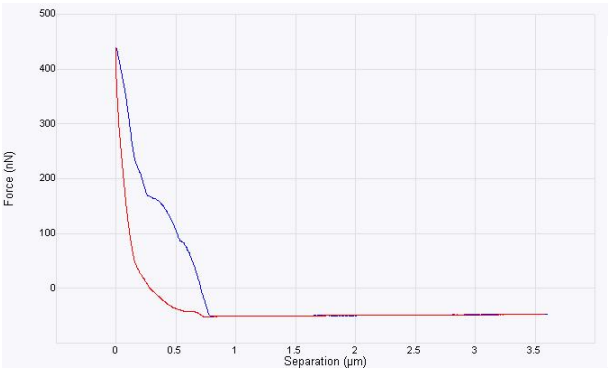


(e) Force-separation

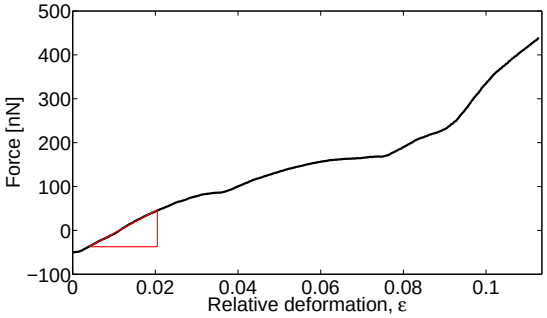


(f) Force-relative deformation

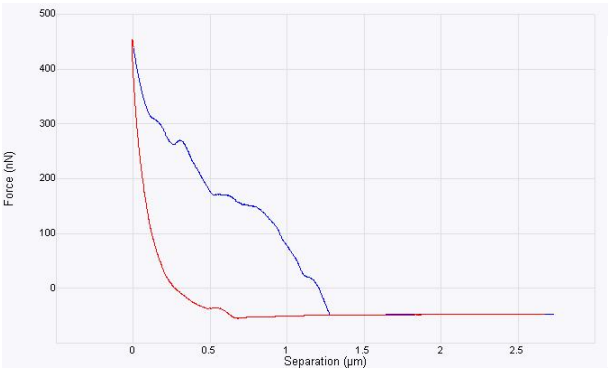


(g) Force-separation

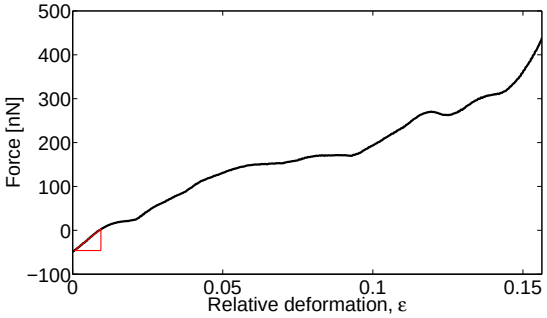


(h) Force-relative deformation

Figure 4.21: Force-separation curves and force-relative deformation curves obtained from a selection of compressed microbubbles stabilized by YM-73 and casein.

### 4.6.4 Multiple compressions

Five of the microbubbles stabilized by YM-73 nanoparticles and casein are compressed several times, so that the effect of multiple compressions on the force-relative deformation curve can be determined. Figure 4.22 shows the force-relative deformation curves obtained by 8 successive compressions of each microbubble. The force curves seem to converge as the number of compressions increases. The force curves from the first and the second compression, and in figure 4.22e also the third compression, tend to differ substantially from the other curves. While there is little deviation in figure 4.22a, considerable differences are seen in figure 4.22b and 4.22e.

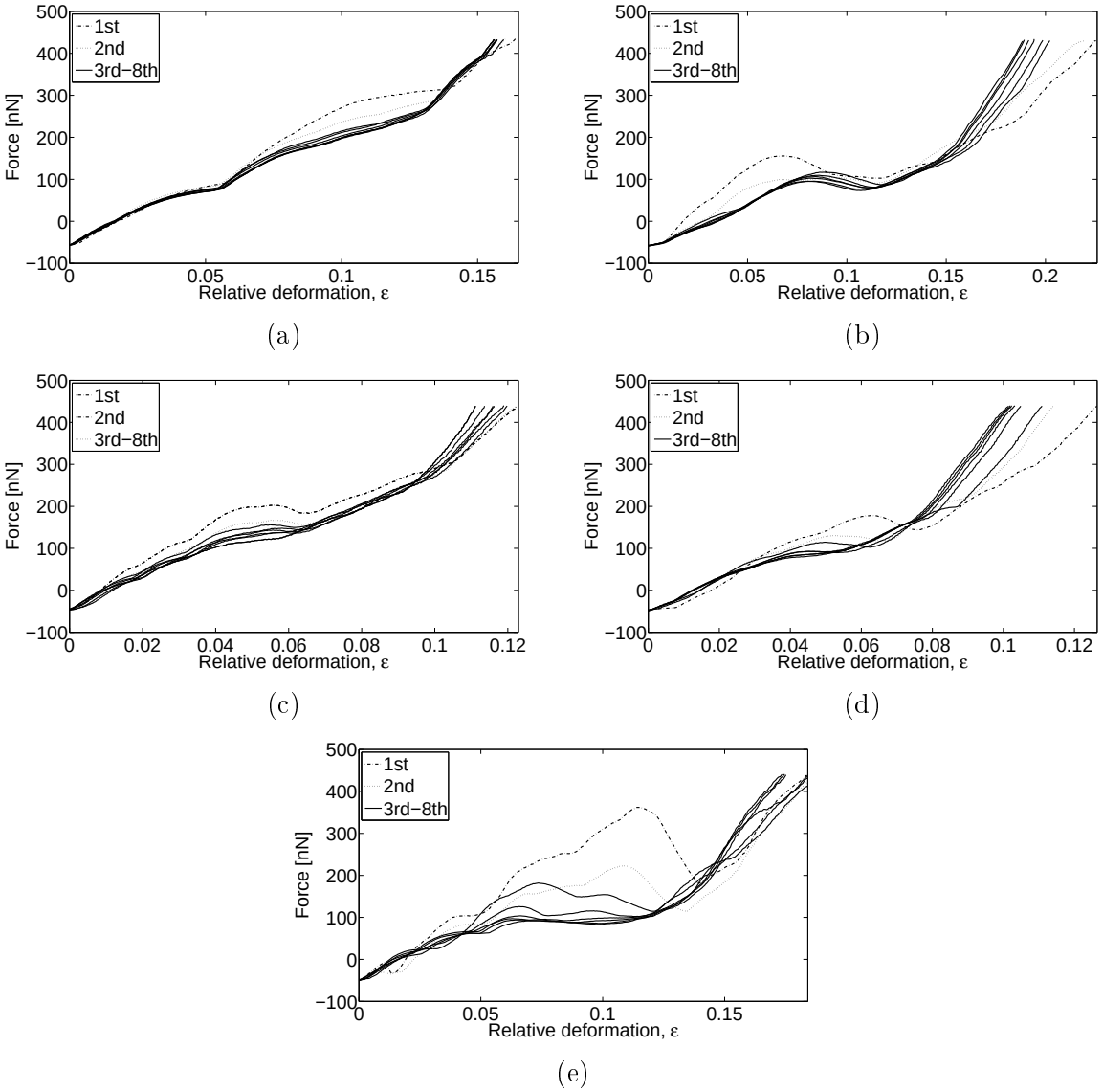


Figure 4.22: Force-relative deformation curves obtained by successive compressions of microbubbles stabilized by YM-73 and casein. The curves from the first to the eight compression is shown.

The Young's modulus is calculated from Reissner theory using the gradient of the initial linear region of each successive force curve of a microbubble. The values of the

Young's modulus calculated from the force curves in figure 4.22a - 4.22d are presented in diagrams in figure 4.23. As expected from the converging curves, the values of the Young's modulus of the microbubble shell seem to stabilize when several compressions are performed. For the microbubbles with values of Young's modulus in figures 4.23a and 4.23d, there is a minorl difference between the values obtained from the first compared to the other compression curves. For the microbubble in figure 4.23c, and in particular for the one with values in figure 4.23b, it is critical whether the first, second or the third compression is used for the estimation of Young's modulus.

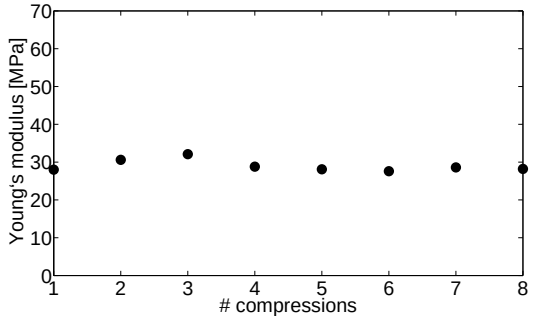


(a) Figure 4.22a

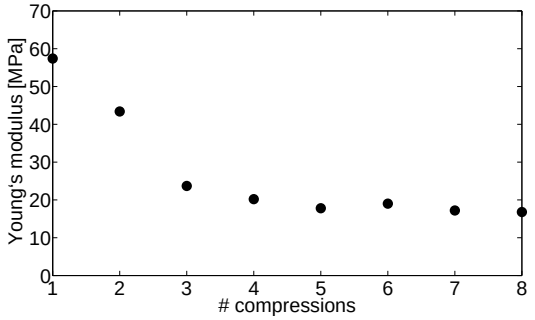


(b) Figure 4.22b

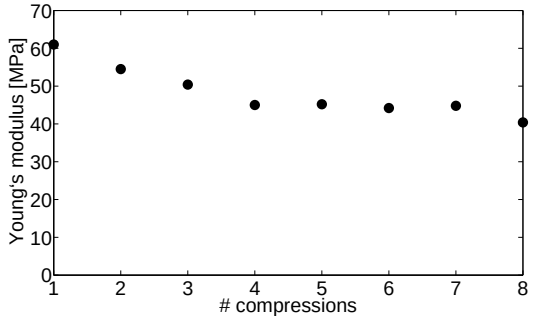


(c) Figure 4.22c

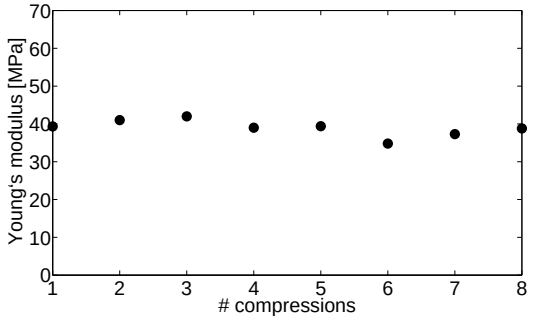


(d) Figure 4.22d

Figure 4.23: Values of Young's modulus calculated from the force-relative deformation curves obtained from successive compressions. The corresponding force curves are found in the figure referenced in the caption.

# Chapter 5

# Discussion

## 5.1 Size distributions

There is an evident size difference between the microbubble batches, according to measurements done by the Coulter Counter and presented in figure 4.1. The microbubbles stabilized by YM-73 nanoparticles and BSA were produced with 8000 rpm and 24000 rpm. Their respective peaks are located at approximately diameter 3.3 and 2.7 μm. As expected, using a higher UT velocity reduces the diameter of the bubbles. Interestingly, the size distribution of the microbubbles stabilized by YM-73 nanoparticles and casein display a peak at diameter 4.7 μm. This is obtained in spite of applying UT velocity 16000 rpm, which normally would cause the distribution to be located between the other two batches. Using casein as a surfactant protein seemingly increases the average bubble diameter. It is observed, as seen in the images in figure 3.3, that less amount of casein is necessary to produce microbubbles. This is advantageous because the surfactant protein may be toxic for the cells. In addition, the bubbles appear more spherical. It is therefore obvious that the surfactant protein is important for how the microbubbles form in the Ultra-Turrax. Why BSA and casein give different outcomes is presumably due to casein having better amphiphilic properties than BSA. Better amphiphilic properties, that is, more pronounced difference between the hydrophobic and hydrophilic part of the protein, give improved stabilizing effect and can influence the bubble formation. In addition, casein is a smaller protein than BSA, which possibly alters the organization of the proteins and the nanoparticles in the shell and the resulting bubble size.

The number of counts do not approach zero on the left side of the distribution, instead there is a tendency of increased counts. The possibility of these counts being caused by something else than microbubbles elicited the choice of 2 μm as the lower limit in the distribution. Figure 4.2a shows the continuation below 2 μm, and a log plot is depicted in figure 4.2b. The number of counts for all batches increases until a second peak at 1.2-1.3 μm is reached. A test of pure electrolyte solution states that this is not caused by noise or artifacts in the solution. It is known that the microbubble suspensions contain a considerable amount of free nanoparticles that have not been positioned in a bubble shell. In addition, experiments have indicated that the nanoparticles form aggregates [46]. The nanoparticles are slightly negatively charged, and the mutual repulsion, in addition to PEG, normally keep them separated. When nanoparticles are suspended in an electrolyte solution, the cations will cause screening of the negative charges, and thus, reduce repulsion and enhance aggregation of nanoparticles. The large amount of counts seen at lower particle diameter is therefore probably due to 1.2-1.3 μm large nanoparticle aggregates.

The counts can also be caused by coincidence measurements of free nanoparticles, that is, several nanoparticles in the aperture interpreted as one larger particle.

To confirm that the large peaks are brought into being by free nanoparticles, the size distribution of a nanoparticle suspension is measured. The concentration of the nanoparticle suspension is chosen so that the concentration of nanoparticles is equal to the concentration of nanoparticles in the microbubble suspension. Perhaps surprisingly, there is poor overlap between the peaks. However, there cannot be the same amount of free nanoparticles in the nanoparticle suspension and in the microbubble suspensions, because a large fraction of the nanoparticles in the microbubble suspension is located in the microbubble shell. A higher concentration of free nanoparticles increases the probability of forming larger aggregates, possibly explaining why there is a deviation between the peaks. In addition, surfactant proteins in the microbubble suspensions associate with the free nanoparticles and reduce aggregation. It is therefore not surprising that the peaks do not overlap. Conditions in the nanoparticle suspension favor aggregate formation to a larger degree than in the microbubble suspensions. Besides, the microbubble suspensions have been subjected to high shear stresses in the Ultra-Turrax, which possibly have broken up aggregates.

The average diameter of the three microbubble batches appear larger in images acquired by the microscope mounted to the AFM Bioscope than what is seen in the size distributions obtained by the Coulter Counter. In the images, the measured average diameters are $5.7 \pm 2.0$ μm, $5.6 \pm 1.3$ μm and $3.9 \pm 1.3$ μm for the casein microbubbles and the large and small BSA microbubbles, respectively. The difference is, however, only significant for the large microbubbles containing BSA. The seemingly greater average diameter can be explained by the fact that larger bubbles are more visible and likely to be selected. In addition, the microbubbles are attached to the dish by positioning the dish inverted on top of the microbubble suspension. It is evident from attenuation measurements of time dependent attenuation that larger bubbles have stronger buoyancy and ascend faster. More of the large bubbles have therefore probably attached to the dish than the smaller bubbles, that do not have the same tendency of floating to the surface. In comparison, the Coulter Counter measurements are done with the aperture positioned in the middle of the sample container. In this location, more of the middle-sized and small bubbles are located, whereas the largest bubbles may have ascended.

## 5.2 Acoustic attenuation

### Uncertainties of the measurements

Acoustic attenuation caused by suspended microbubbles located in an acoustic field is measured and plotted as function of transmit frequency. For the BSA microbubbles, various transducers are used, and the curves obtained with transducers with different center frequency are highly consistent. Overlapping occurs within one standard deviation at most frequencies. As a consequence, transducer characteristics do not influence attenuation measurements significantly. Differences can be due to the fact that two different transducers do not measure the same samples. A plotted attenuation spectrum for a specific transducer represents an average of spectra obtained from several samples. Even though the same method is used to prepare all the samples, there is likely to occur variations in the measurements due to the heterodisperse microbubbles.

Firstly, microbubbles are pipetted out of a microbubble container. Shaking the container may not be sufficient to ensure a homogenized mixture of microbubbles. Some variance in the concentration of microbubbles in the volume added to the sample chamber is therefore probably. In addition, microbubbles tend to attach to the outer surface of the pipette tip. This could potentially cause addition of indeterminable amount of microbubbles to the sample, but is solved by rinsing the tip before injection.

Secondly, and probably most critical for the uncertainty of the measurements, the microbubbles are not necessarily distributed homogeneously in the sample chamber. It is desired that the concentration and size distribution of microbubbles in the volume represented by the ultrasound beam reflects the concentration and size distribution in the whole sample chamber. This may not always be the case because of random fluctuations. Different measurements may not have the same concentration or size distribution of microbubbles located in the beam.

Furthermore, its observed that the attenuation depends on time post injection. It is unlikely that the reduction is caused by leakage of gas, due to the fact that the microbubbles can be stored in liquid for several weeks without noticeable changes. Attenuation reduces more rapidly with time for larger microbubbles than smaller, which implies that larger microbubbles more quickly float towards the surface of the sample. Consequently, both the concentration and the size distribution in a specific part of the chamber will change with time. However, it is shown that the attenuation can increase the first 5 minutes, meaning that the sample is not initially homogeneous. To achieve more equal conditions, all attenuation measurements are performed 5 minutes after addition of microbubbles. Though, because of uncontrollable alterations in the states of the microbubble immediately after addition, floatation effects after 5 minutes will vary and lead to differences in the measured attenuation spectra.

The length of the error bars reflects the uncertainties. The length increases at higher and lower frequency, in particular for the BSA microbubbles. This is because the transducers are less sensitive to frequencies far from the center frequency. Some transducers are more broadbanded than others, e.g., the 5 MHz transducer is sufficient to acquire the important parts of the attenuation spectrum for the casein microbubbles, while the curves obtained with the 3.5 and 7.5 MHz transducers are limited to a smaller frequency range. High frequent ultrasound is more attenuated by water, possibly explaining the increased uncertainty at higher frequencies.

Ultrasound pulses have 3 spatial dimensions in the bubbly liquid that are represented by one dimensional received signals. Potential directivity to the transducers and asymmetric acoustic fields are not accounted for and may influence the attenuation measurements.

### Variation between microbubble batches

The results demonstrate that the attenuation spectra can be altered by changing the microbubble diameter and the surfactant protein. The attenuation caused by large BSA microbubbles is maximum at 5.0 MHz, while the peak in the attenuation spectrum of the small BSA microbubbles is approximately 14 MHz. Microbubbles attenuate more strongly at the resonance frequency [22]. Therefore, the peak in an attenuation spectrum of a microbubble population corresponds to or is in proximity to the resonance frequency of the population. From equation 2.15, the resonance frequency of a bubble is inversely proportional to its radius. Because the size distributions of the measured microbubble populations are wide, the resonance frequency of a bubble population repre-

sents an average resonance frequency of all the bubbles in the population. The large BSA microbubbles, produced with UT velocity 8000 rpm, have a larger average diameter than the small BSA microbubbles, produced with UT velocity 24000 rpm. Consequently, the resonance frequency will be higher for the batch will smaller bubbles, which is observed.

A wide size distribution will lead to a broad attenuation spectrum, as seen by comparing the size distribution and attenuation spectrum of the casein microbubbles with the distribution and spectrum of the large BSA microbubbles. Microbubbles with larger and smaller diameter resonate at lower and higher frequency and contribute to a broad attenuation spectrum.

Even so, the size distribution is not sufficient to cause the broad attenuation spectrum acquired from the casein microbubbles. The viscosity of the shell modifies the width of the spectrum by increasing the damping. Comparing and fitting theoretical attenuation spectra calculated using Church model to the measured spectra, reveals that the viscosity is higher for microbubble shell containing casein than for shell containing BSA. The values, $0.46 \pm 0.03$ Ns/m$^2$ for large BSA microbubble shell and $0.25 \pm 0.03$ Ns/m$^2$ for small BSA microbubble shell, are considerably smaller than for casein microbubbles, which has estimated viscosity of the shell $1.29 \pm 0.03$ Ns/m$^2$.

Substituting BSA with casein not only shifts the size distribution to larger average diameter and broadens its width, but also increases the resonance frequency of the bubbles. This is unexpected, because increasing the average diameter should normally lower the resonance frequency. However, equation 2.15 is valid only for a free uncoated bubble. The shell of an encapsulated microbubble modifies the resonance frequency, which is described in equation 2.19. A higher shell thickness to radius ratio or a more stiff shell with larger shear modulus, both increases the resonance frequency of a bubble.

Values of the shear modulus that minimize the summed square difference between the calculated attenuation spectra using Church model and the measured spectra are $7.4 \pm 1.1$ MPa, $14.4 \pm 2.5$ MPa and $30.7 \pm 2.8$ MPa for the large and small BSA microbubbles and the casein microbubbles, respectively. Because the microbubbles with casein as surfactant protein have higher resonance frequency than the large BSA microbubbles, despite having larger average diameter, and since the shell thickness is assumed to be constant, the value of the shear modulus for casein microbubble shell must necessarily be larger. It is not unlikely that a different protein in a microbubble shell alters the viscoelastic properties of the shell. Variations in how the proteins are organized, linked together, and attached to the nanoparticles, will all probably modify the shell properties, and such variations are dependent on the protein type. Because casein is a smaller protein than BSA, it can reasonably be more densely packed and increase the stiffness and the shear modulus. What is less clear, however, is why viscoelastic properties depends on the UT velocity used to produce microbubbles with same type of shell proteins. A possibly explanation is that for bubbles with smaller diameter, the curvature is larger, and thus, the nanoparticles and the surfactant proteins organize themselves differently. A more dense packaging could result in the larger shear modulus observed. Another, and perhaps more likely reason is that the shell thickness may not be constant, but instead it may vary with the bubble diameter and also the surfactant protein.

The shear modulus and the viscosity decrease when the assumed shell thickness increases, according to table 4.5. This result suggests that the values of the shear modulus and the viscosity are overestimated for the casein microbubbles, and that casein actually causes a thicker shell, either directly by potentially attracting more nanoparticles, or indirectly by increasing the diameter and assuming that shell thickens with larger diameter.

The latter statement is not supported by the fact that large BSA microbubbles have lower $G_s$ than small BSA microbubbles. If so, the shell thickness could be proportional to the diameter for microbubbles with casein and inversely proportional for microbubbles with BSA as surfactant protein.

Hoff *et al.* measured acoustic attenuation caused by a polymeric microbubble population [43]. The shell thickness was found to be proportional to the diameter [22], approximately 200 nm for a bubble with 4 μm diameter, which is similar to the nanoparticle-stabilized microbubble characterized here. The resonance peak appeared at approximately 4.5 MHz. The shear modulus and the viscosity were estimated to be $11.5 \pm 2$ MPa and $0.4 \pm 0.1$ Ns/m$^2$, respectively. The attenuation peak and the estimated values are close to the obtained results for the large BSA microbubbles. Because of the differences in the shell structure between the microbubbles, the purpose of comparing the results is limited, still, the results indicate that the order of magnitude is correct.

The attenuation spectrum obtained from a population of commercial HEPS-Na/PFB microbubbles with shell thickness 2-3 nm has a maximum around 19-20 MHz (figure 4.5e). Because of their small size, the average diameter is reported to be 2 μm, the resonance frequency is expected to be higher than for the small BSA microbubbles with maximum in the size distribution at diameter around 2.7 μm. This is also observed. Viscoelastic parameters could not be estimated because the size distribution has not been measured. Still, the results can be compared with various studies that have examined thin-shelled microbubbles.

The contrast agent Sonazoid containing perfluorocarbon gas with approximately 4 nm shell thickness has been analyzed by Hoff [22] and Sarkar *et al.* [59]. The measured average diameter was 3 μm, and the estimated shear modulus and viscosity were $50 \pm 3$ MPa and $0.8 \pm 0.1$ Ns/m$^2$ and $52 \pm 10$ MPa and $0.99 \pm 0.3$ Ns/m$^2$ by Hoff and Sarkar *et al.*, respectively. The attenuation spectrum had a peak at 4.2-4.5 MHz for both groups, which is considerably lower than for the thin-shelled microbubble measured in this thesis.

The viscoelasticity of a 1 nm thick lipid shell of a microbubble with 2 μm average diameter has been estimated by Gong *et al.* [60] using attenuation measurements and optimizing the theoretical curve using Hoff model. The maximum attenuation appeared at 2.3 MHz, and the shear modulus and viscosity were found to be 10 MPa and 1.49 Ns/m$^2$.

Furthermore, Yu *et al.* [61] measured attenuation spectra of the contrast agent Levovist which is coated by galactose and palmitic acid. A peak at 2.3-2.5 MHz was obtained. The average diameter was 3 μm and the shell thickness estimated to about 3 nm. The viscoelastic shell parameters were $G_s \approx 80$ MPa and $\mu_s \approx 1.3$ Ns/m$^2$.

These studies show that for 2-3 μm large microbubbles with shell thickness 1-4 nm, the maximum attenuation is apt to occur at frequencies in range 2.3-4.5 MHz. This is not in agreement with what was measured for the HEPS-Na/PFB microbubble. On the other hand, there is seemingly a large variation in values of both the shear modulus and the viscosity of the shells of the different lipid microbubbles, possibly due to differences between the lipids used in the shells.

A study of how the resonance frequency depends on bubble diameter has been conducted by Goertz *et al.* [62]. The attenuation caused by lipid-coated microbubbles with varying diameters were measured. For bubbles with 6.8 μm diameter, the peak appeared at a frequency lower than 3 MHz. After the microbubbles were passed through a 2 μm

filter, so that only bubbles with diameter below 2 μm were measured, the attenuation peak shifted to 10-15 MHz. Filtering at 1 μm diameter resulted in a peak above 50 MHz. Consequently, the bubble size affects strongly the resonance frequency and the attenuation spectra. The results can also point to why the measured attenuation caused by HEPS-Na/PFB microbubbles is maximum first at 20 MHz. The measurements were done after 5 minutes, for consistency with the nanoparticle-stabilized microbubbles. If, however, these thin-shelled microbubbles have a much higher buoyancy or gas leakage, the consequence would be to effectively filter out the large bubbles, just as observed by Goertz *et al.*

**An adjusting constant**

In order to minimize the summed square difference between the measured and calculated attenuation spectra and obtain a best fit, a constant multiplied with the microbubble concentration must be introduced in the calculations. The value and significance of this constant depends on the microbubble batch. For the small BSA microbubbles, the optimal constants is 1.5, and there is minor differences between the fits obtained with and without multiplying by this constant. On the other hand, for the large BSA and the casein microbubbles, the constants are 2.8 and 3.0, respectively. With these batches, and especially for the bubbles containing casein, introducing the constant causes substantial improvements of the fits. There may be various reasons to demand such a constant. But also to question the validity of the estimated viscoelastic shell parameters.

First of all, the employed bubble model is not an ideal model for the studied microbubble structure. Church model requires a spherical bubble encapsulated by a solid, viscoelastic, incompressible and uniform shell. The nanoparticle-coated microbubbles are not necessary spherical, which is supported by images in figures 3.3 and 4.16i. Besides, oscillating bubbles may exhibit various non-spherical shapes in different vibration modes [63].

In addition, the shell is probably neither homogeneous nor uniformly distributed around the bubble. Additional nanoparticles may attach to or detach from a specific side, causing shell thickness to vary as function of time and azimuthal and polar angles. A student project work done by Andreas Bøe showed indications for a shell thickness that increases with time [57]. Because the volume of the bubble shell is required in the model, uncertainty in the shell thickness leads to large uncertainty in the calculation of attenuation and resulting parameter estimations.

Moreover, assumption of an incompressible shell may be incorrect. Loosely packed nanoparticles and surfactant proteins may re-localize and organize themselves differently upon compression.

The church model is further simplified by assuming that the oscillation amplitude is small. Low pressure amplitudes, around 10-30 kPa, are applied during the acoustic attenuation measurements, approving this assumption. However, backscatter measurements reveal that higher harmonic scattering and thus non-linear and high-amplitude oscillation can potentially be present for all microbubble batches at around 30 kPa. Therefore, neglecting effects of larger oscillation amplitudes may influence the results.

The expression for the dispersion of a sound wave propagating through a bubbly liquid (equation 2.22) is used along with the Church model to integrate the effects from a population of oscillating microbubbles and calculate the attenuation caused by them. In the derivation of the dispersion relation by Commander and Prosperetti, the oscillations

were also assumed to be linear. Yet, the linear assumption is likely not responsible for the error possibly producing the required constant [42].

Instead, probably more important is the requirement by using the dispersion relation of a small fraction of occupied volume by the bubbles (equation 2.23). Commander and Prosperetti [42] analyzed data published by Silberman [64] of attenuation caused by relatively large, 1-3 mm diameter, bubbles in water. The measured attenuation coefficients were compared to the theoretical attenuation coefficients obtained from the dispersion relation (equation 2.22), and the agreement was generally good, except in the proximity of the resonance frequency. Arbitrarily adjustment of the size distribution used in the theory could improve the conformity. Different concentrations of bubbles were used, with volume fraction ranging from $\beta = 0.000377$ to $\beta = 0.01$. Discrepancy around resonance was seen for all concentrations.

Kol'tsova *et al.* [65] measured attenuation of 15 - 20 μm large gas bubbles. The volume fractions were $\beta = 0.00002$ to $\beta = 0.0003$, i.e., very small. When the data was compared with the theory by Commander and Prosperetti, a similar pattern was observed; data and theory agreed well, except in the resonance region, where the data was consistently below theory. Reducing the volume fraction did not improve the result significantly.

The comparison between measured data and theory is in accordance with the results in this thesis. Most deviation is seen for the microbubble batches where the resonance region dominates and is in the center of the spectrum (figures 4.6a and 4.6b). If theory and experiments disagree at resonance, it is expected that attempts of fitting in this region will fail. For the small BSA microbubbles, most of the plotted spectrum and the subsequently fit are located below resonance, and not surprisingly, the discrepancy is less.

Besides, the volume fractions occupied by the microbubbles stabilized by nanoparticles in the experimental work of this thesis are substantially larger than in the studies analyzed by Commander and Prosperetti. The values of $\beta$ are approximately 0.059, 0.185 and 0.083 for the large and small microbubbles encapsulated with BSA and the casein microbubbles, respectively. The above-mentioned results were not reported to be significantly dependent on $\beta$, for $\beta < 0.01$. Terms of order $\beta^2$ were neglected in the theory. The constant multiplied with the concentration, and which effectively adjusts $\beta$, could potentially be needed to compensate for the omission of the second order term. This does, however, not explain why deviation at resonance was seen for much lower values of $\beta$. Adjustment of the size distribution was also attempted by Commander and Prosperetti to improve the results, which points to that the introduced constant adjusts an error caused by an inaccurate theory. A probable cause for the error was identified as a lack of consideration in the theory of enhanced bubble interaction in the resonance region.

Grishenkov *et al.* [41] used the same dispersion relation for PVA shelled microbubbles and achieved good agreements between the theoretical and experimental curve. As for the small microbubbles encapsulated with nanoparticles and BSA, most of the fitting was done distant from the resonance frequency. As a consequence, evidence indicates that the employed dispersion relation only holds at frequencies not close to resonance frequency.

Eventually, it must also be considered that the size distributions measured by the Coulter Counter do not accurately reflect the actual size distributions of microbubbles located in the ultrasound beam in the sample chamber during attenuation measurements. Even though similar conditions were pursued and several samples averaged, there may be systematical differences in the setups. E.g., the aperture tube, where the particles

pass through in the Coulter Counter, is positioned closer to the surface of the liquid compared to the ultrasound beam in the sample chamber. Because larger bubbles are disposed to float to the surface more rapidly than smaller bubbles, a higher number of large bubbles may be counted, which leads to shifting of the measured size distribution towards larger diameters with respect to the the real bubble size distribution in the beam volume. Besides, the distributions are probably influenced by counts of possible nanoparticle aggregates with sizes on the order of the microbubbles. This is particularly relevant for the small BSA microbubbles, where the peak barely is visible. Consequently, an overestimation of the concentration of microbubbles, especially of those with smaller diameter, is probable. Because the right side of the peaks appears non-affected, the more affected left side could alternatively be found by assuming that the bubble size distribution is symmetric or Gaussian. Nonetheless, mainly the microbubbles with large diameter contribute to the calculated attenuation spectra in the particular frequency range. Therefore, wrongful estimation of the concentration of the smallest microbubbles is not crucial for the theoretical results.

### Assumed parameters in the bubble model

Parameters required in the calculation of the theoretical attenuation spectra are not measured and may be inaccurate or wrong. The shell density is assumed to be 1200 kg/m$^3$. This is approximately the density of PBCA [58], the polymer and main component of the nanoparticles. Though, the particles may be loosely packed in the shell, effectively reducing the density. In addition, a surfactant protein is present. As a result, the estimated density is highly inaccurate. Large deviation is, however, unlikely, and the effect of changing the density by 10 % is unnoticeable.

It is assumed that the microbubbles oscillate with a high enough frequency so that heat transfer is negligible. For adiabatic processes, the polytropic constant is 1.4. A more realistic assumption is that some heat transport is happening. The process would then be neither isothermal nor adiabatic, and the constant would be between 1 and 1.4. Even so, because the second term within the parentheses in equation 2.19, $\frac{4V_s G}{R_{02}^3}$, is much larger than the first term, $3\kappa p_{0g}$, changing the constant from 1.4 to 1 does not play any role in the final result.

### The Church model compared to the Hoff model

There are agreements between the Hoff model and the Church model for the viscoelastic parameters for the shell of the large microbubble encapsulated by nanoparticles and BSA. With assumed shell thickness 150 nm, the obtained values for the two models differ, but insignificantly. Significant deviation is seen with 300 nm thickness, while no difference is present with thickness 15 nm. This is as anticipated, because the Hoff model is a simplification of the Church model with the assumption of small shell thickness. When the thickness is small, there should be no difference. The results suggest that the simplified model can be adequate for shell thickness below 150 nm, but not above.

Interestingly, the same constant multiplied with the concentration is required to get the best fit when Hoff model is employed. Hoff used a different approach to include the effects from a whole bubble population. Nevertheless, just as with the dispersion relation, it is required that the interactions between the bubbles are negligible. This may not be the case at resonance, where, e.g., a pressure field exciting a bubble may be comparable, or even smaller, than the pressure wave scattered by a neighbor bubble. That the

mentioned constant is needed in both models can therefore be due to use of an exceeding concentration of microbubbles, leading to unpredicted interactions at resonance.

It is proposed that for the microbubbles encapsulated by BSA and nanoparticles, only the albumin is in reality stabilizing the microbubble, and the nanoparticles function merely as dampers attached to the albumin shell. The consequence would be a much smaller shell thickness, approximately 15 nm. The resulting viscoelastic parameters with this thickness assumption using Church model are $G_s = 90 \pm 12$ MPa and $\mu_s = 5.2 \pm 0.6$ Ns/m$^2$. These values can be compared to the attenuation spectra obtained by Hoff for Albunex microbubbles with albumin shell and thickness 15 nm [22]. The corresponding estimations of shear modulus and viscosity were $120 \pm 20$ MPa and $2.2 \pm 0.8$ Ns/m$^2$. Whereas the shear moduli differ almost insignificantly, there is a difference of factor approximately 2 in viscosity. It is possible that the nanoparticles effectively contribute with an increased value of viscosity that can explain the deviation. This alternative interpretation of the microbubble shell structure has not been analyzed further, but is worth considering in later work.

## 5.3 Acoustic backscatter

### Non-linear oscillations and higher harmonics

Measurements of acoustic backscatter show that the microbubbles stabilized by polymeric nanoparticles scatter non-linearly and produce higher harmonics at 15-30 kPa. When compared to a commercial HEPS-Na/PFB microbubble, there is minor differences in the scattering spectra. For the HEPS-Na/PFB microbubble, the higher harmonics appear to emerge at lower pressure than for the microbubbles stabilized by nanoparticles. The earlier onset of non-linear oscillations can be explained by a thinner and more flexible shell of the HEPS-Na/PFB microbubbles. A thinner shell has less inertia and resistance against large amplitude oscillation. On the other hand, it is plausible that larger pressure is necessary to induce large-amplitude oscillations of the thicker nanoparticle shell.

Among the YM-73 microbubbles, at 5 kPa, the received power is predominantly at the transmit frequency 1 MHz. The single peak is in accordance with the expectation for microbubbles oscillating linearly with small amplitudes. There is an increase in the noise level at higher and lower frequencies around 5 MHz. Because the shown spectra are corrected to compensate for the frequency response of the receive transducer, there seems to be an underestimation of the frequency response at frequencies distant from the center frequency. An inaccurate estimated frequency response will affect all spectra equally and will not influence the comparison of the spectra, only differences in power between peaks of the same spectrum.

The applied pressures are determined from a conversion of the known voltage. The conversion factor is measured by a hydrophone at a specific voltage, and it is assumed that the pressure relates linearly to the voltage. This linear relation has not been tested and may not be true at high and low voltages. As a consequence, the pressure amplitudes have a high uncertainty and must be considered as approximations.

The scattering spectra of the casein microbubble display higher harmonics already at 15 kPa, while for the BSA microbubbles, significant peaks at 2 MHz or higher are present first at 30 kPa. This indicates that the casein protein makes the shell more susceptible for non-linear oscillation at lower pressure, either directly by changing properties of the

shell, or indirectly by increasing the average bubble diameter. In general, the resonance frequency of a bubble reduces when the diameter increases (see equation 2.15), and it is shown that the casein induces larger microbubbles. If the casein microbubbles actually have a lower resonance frequency than the large BSA microbubbles, and thus closer to the 1 MHz transmit frequency, it is expected that the casein microbubbles would oscillate with larger amplitudes and display more non-linear behavior. However, the attenuation measurements point to that the resonance frequency of the casein microbubbles is higher than for the large BSA microbubbles. Earlier emergence of harmonics because of lower resonance frequency is therefore unlikely.

When comparing the scattering spectra of the casein microbubbles at 15 and 30 kPa, the harmonics lose power. The cause can be measurements done under unequal conditions. To reduce the effect of time on the results, backscatter measurements of a microbubble batch at different pressure amplitudes are performed within 10-15 minutes after addition into sample chamber. Nevertheless, as the results for the time dependent attenuation measurements of the larger BSA bubbles show, the attenuation reduces rapidly after 10 minutes. Because the scattering at two different pressure amplitudes are not measured at the same time, it is expected that there may be differences between the resulting spectra that are not only due to different applied pressure, but also due to variation in the bubble distribution in the ultrasound beam at the two points in time. Further works should control for the time dependency and do measurements of several samples. This was not done in this thesis due to limited availability of equipments.

### Destruction of microbubbles

All measured microbubble batches show evidence for destruction at larger pressure amplitudes, in particular at 510 kPa. Bubble destruction, that is, inertial cavitation or collapse, is recognized in the scatter spectra as a high noise level. The radiated sound field of a collapsed bubble contains no more discrete harmonics, but broadband noise. The scatter spectra from the large BSA microbubbles indicate that more and more bubbles are destructed as the power of the noise gradually increases with less increase of power at the harmonics. While a substantial amount of microbubbles are destroyed at 510 kPa, the bubble destruction is initiated at lower pressures, with already a fair amount of destruction taken place at 170 kPa. This corresponds to a Mechanical Index 0.17. A comparison with received spectra from the small BSA microbubbles shows that at 510 kPa, the number of harmonics is higher and the noise level lower for the small microbubbles, indicating that larger BSA microbubbles are destructed more easily.

Pulse inversion imaging of the large BSA microbubbles (figure 4.14) is in accordance with the backscattering measurements and shows that there is a considerable reduction of bubbles between $MI = 0.15$ and $MI = 0.18$. The destruction continues, and only a small percentage of the microbubbles remain at $MI = 0.33$, as expected.

The radiation of the casein microbubbles contains small amount of harmonics already at 340 kPa. Mayor destruction therefore appears to start at lower pressure than for the large BSA microbubbles. This is not unanticipated, since the casein alters the shell properties and increases the microbubble diameter. More destruction of microbubbles at lower $MI$ is also noticeable in the ultrasound images (figure 4.15). The images indicate a first reduce of microbubbles at $MI = 0.18$. However, the reduction is more significant between $MI = 0.18$ and $MI = 0.23$ for the casein microbubbles than for the large BSA microbubbles, confirming that the casein may cause bubble destruction at lower pressure.

The scattering spectrum at 510 kPa of the thin-shelled HEPS-Na/PFB microbubbles displays more harmonics than the larger microbubbles, but similar amount of harmonics as the small BSA microbubbles. Thus, a smaller radius, and also a more flexible shell, may be protective against destruction.

Similar results were acquired by Hoff [22] from backscatter measurements of Sonazoid. The acquired results are highly similar to the results of scattering measurements for the YM-73 microbubbles, in particular those with shell of BSA. The second harmonic is still low around 17 kPa, the noise level increases significantly at 170 kPa, and substantive destruction is occurring at 430 kPa.

Quantison, an albumin-coated microbubble, was observed by Frinking *et al.* [66] to be destroyed at pressures above 500 kPa. The scattering was received by a 10 MHz transducer, and the ultrasound generated by a 1 MHz transducer. The fundamental dominates at 300 kPa, and at 600 kPa, the scattering spectrum is analogous to the spectrum of the large BSA microbubbles at 170 kPa. As a consequence, this polymer microbubble resists non-linear scattering and destruction to a higher degree than the microbubble coated with polymeric nanoparticles.

Moreover, results from scattering measurements with a 5 MHz transmit transducer suggest that using low transmit frequency, i.e., high $MI$, is more critical for destruction than a transmit frequency close to the resonance frequency. Large and small BSA microbubbles are exposed to ultrasound pulses from a 5 MHz transmit transducer, and scattering received by a 15 MHz transducer. With 510 kPa applied pressure, corresponding to $MI = 0.23$, there are no signs of significant destruction of microbubbles in the resulting spectra. Besides, there are minor differences between the two batches, even though ultrasound is transmitted at the resonance frequency of the batch with larger average diameter.

These indications are supported by the scattering spectra acquired by using a 3.5 MHz transmit transducer. At 520 kPa, albeit with an elevated noise level compared to lower pressure, the scattering spectra of both the BSA and the casein microbubbles have still highly distinct peaks at the fundamental and the second harmonic, and there is no convincing evidence for destruction.

Provided that the pressure amplitudes are correctly estimated for all the transmit transducers, these results argue that probability of microbubble destruction increases with lower transmit frequency when the same amount of pressure is applied, as predicted by the Mechanical Index.

### Sub- and ultraharmonics

Distinct peaks representing sub- and ultraharmonics are recognized in the spectra of scattering elicited by the 3.5 MHz transducer at pressures larger than 1040 kPa for the BSA and casein microbubbles. Subharmonic response has been suggested as a signature of inertial cavitation [67]. According to the results using 1 MHz transmit frequency, mayor destruction is expected at this pressure level. The observed subharmonics can therefore be due to destroyed bubbles.

The frequency content of the backscattered energy from the phospholipid-coated microbubbles SonoVue has been measured by de Jong *et al.* [63] and shows a distinct subharmonic at 48 kPa using 3.5 MHz transmit frequency. At 75 kPa, an ultraharmonic

peak appears at 5.25 MHz. These pressure amplitudes are considerably lower than for the microbubbles encapsulated by nanoparticles. A reasonable explanation is the thinner and more flexible phospholipid-coating. This finding suggest that subharmonics are not only caused by cavitation, and a model by Marmottant predicts subharmonics at low pressures for bubbles coated by lipids [68]. The reason is thought to be buckling of the bubble shell.

Furthermore, Sonazoid was shown by Sarkar *et al.* [59] to radiate subharmonics at pressure levels higher than 300 kPa at 6 MHz insonation. Gong *et al.* [60] found significant subharmonic component when transmitting with 5 MHz frequency and pressure amplitude above 400 kPa for a microbubble with approximately 1 nm thin lipid shell. These observation demonstrate that the necessary pressure for subharmonic emergence vary between different lipid-coated bubbles and seems to increase for higher transmit frequency.

The non-linear properties of Optison have been characterized by Forsberg *et al.* [69] by insonifying the microbubbles with a 4 MHz transducer and measuring the backscatter signals. Optison has a shell of albumin and is more similar to the microbubbles studied in this thesis. In contrast to the lipid-coated microbubbles, but in agreement with the nanoparticle-coated microbubbles, Optison showed significant sub- and ultraharmonic components in the scattering spectra first above 1000 kPa.

## 5.4 Mechanical properties of microbubbles using AFM

Characterization of microbubbles using AFM provides individual properties, in contrast to acoustic characterization that characterize collective properties of the microbubbles. In addition, the methods operate at different time scales; fractions of second for AFM and microseconds for ultrasound. These differences must be considered when comparing results obtained from the two techniques.

### Estimation of Young's modulus of the microbubble shell

The values of Young's modulus calculated from Reissner theory show relatively large variability among the different microbubble batches, but also among microbubbles of the same batch. YM-73 casein microbubbles have average Young's modulus $37 \pm 17$ MPa, an average value which is considerably larger than the YM-73 BSA microbubbles that have average Young's modulus $15 \pm 7.8$ MPa. That the shell is stiffer when casein is used as surfactant protein instead of BSA, is a conclusion that is in accordance with results obtained by acoustic attenuation measurements. A conversion between Young's modulus and the shear modulus exists for homogeneous isotropic materials (equation 2.39). Because the bubble shell is neither homogeneous nor isotropic, no routine conversion is possible. Even so, it is expected that the two moduli have values on the same order of magnitude, and that the Young's modulus is larger than the shear modulus. This is also observed.

All microbubble batches have values of Young's modulus with an apparent size correlation. However, only for the YM-73 casein microbubble is there a significant linear relation between the Young's modulus and the diameter. A possible explanation for this relation is that larger microbubbles actually have a thicker shell that is not taken into account. Because $E$ is inversely proportional to $t^2$, underestimation of $t$ for larger bubbles causes $E$ to be overestimated.

Alternatively, there can a difference between the shell of small and large microbubbles, but also of microbubbles of the same size, in the organization of nanoparticles and surfactant proteins. The resulting variation in electrostatic interactions hindering compression may cause or contribute to the noticed variations in the stiffness and Young's modulus.

Chen *et al.* [70] compressed phospholipid microbubbles using AFM and found values of Young's modulus for the shell in the range 0.5 - 3 MPa that decrease exponentially with the microbubble diameter. The reason for the decay was linked to a more dense packing of phospholipids for bubbles with larger curvature. This group used an equation proposed by de Jong *et al.* [71], where the Young's modulus is proportional to the gradient of the initial linear region of the force curve, just as in Reissner theory. However, in the equation used by the group, $E$ depends on $t^{-1}$ instead of $t^{-2}$.

On the other hand, Santos *et al.* [54], likewise studying properties of pospholipid microbubbles with AFM, employed Reissner theory and reported Young's modulus in the range 300 - 850 MPa and a significant linear relation between Young's modulus and diameter, in contrast to Chen *et al.* It is alarming that two different equations, both attempting to describe the elastic behavior of the compression of a same type of microbubble, differ considerably. Other estimations of the stiffness of phospholipid microbubbles done by various studies [22, 54] tend to be closer the result obtained by Santos *et al.*, indicating that Reissner theory is more appropriate.

However, the Reissner theory is derived under several assumptions that are not necessary fulfilled by the studied microbubble stabilized by polymeric nanoparticles. The shell is supposed to be thin and preferably less than 1/20 of the radius [55]. If the assumption of 150 nm shell thickness is correct, this requirement is met only for the largest microbubbles. As with the Church model, the shell is further assumed to be isotropic and homogeneous, and neither of the assumptions can be guaranteed nor are probable. The validity of the results must therefore be considered as limited. Per contra, Reissner theory was used by Glynos *et al.* [53] and Fery *et al.* [55] and provided results agreeing with other reports, as long as the deformations were small and below $\epsilon_{crossover} \approx 0.7-0.12$ for the nanoparticle-coated microbubbles (equation 2.41). The linear region used in the calculation of the Young's modulus is located below $\epsilon_{crossover}$ for all studied microbubbles in this thesis. Therefore, despite using a simple and inaccurate model, some consistency with results obtained using a more advanced and appropriate future model should be expected.

### Force-deformation curves

The representative force-relative deformation curves (figures 4.19- 4.21) acquired by compressions of microbubbles have recognizable and repeatable patterns. The initial elastic regime is represented by the region where the force depends linearly on the deformation. The length of this region is variable, and some curves display several linear regions with different slopes. The values of the Young's modulus in the result are calculated from the first linear region with reasonable length. Reasonable means here the region where the longest linear fit with coefficient of determination $R^2 > 0.995$ can be achieved. The requirement is set after inspection of various curves. A smaller or larger value of $R^2$ would for some curves lead to a selection of an alternative region, which often has a dissimilar slope, and hence, a different Young's modulus would be calculated. For example, the curve in figure 4.20c contains a linear region at lower $\epsilon$ with a larger slope, whereas the curve in figure 4.19g, there is an initial region that is considerably flatter than the selected one. Nevertheless, in both cases, the length of the regions is smaller, so they were not

chosen. Because such conflicts are absent for most force curves, and also that there is no tendency of skipping neither larger nor smaller slopes, the consequence is not of big importance, but it gives higher uncertainty. Elastic regions with variable slopes can be a result of the cantilever meeting higher or lower resistance during the compression of the bubble.

When the compression is increased further, in particular above $\epsilon \approx 0.1$ for most bubbles, the plastic regime is reached. Deformations in this regime cause low reversibility for the approaching and retracting curves, i.e., large hysteresis, and occurrence of abrupt breaks and plateau phases. Only the elasticity of the shell is of interest here, so the force curve is not analyzed at larger compressions. At this stage, whole bubble effects get more pronounced. In addition to plastic properties of the shell material, the observed responses can have causes such as buckling and failure of the shell, re-localizing of nanoparticles, leakage of gas and displacement of the bubble with respect to the surface. That the approach and retract curve do not overlap signifies that energy is dissipated during deformation. Besides, it is possible that the shell is cracked and the bubble damaged or collapsed. Though, images were acquired after the compressions, but no evidence of damage to the microbubble could be noticed.

Vinogradova *et al.* [72] noticed similar patterns of the force-deformation curve obtained by AFM compressions of hollow DNA/poly(allylamine hydrochloride) microcapsules. An interesting application of a special confocal microscope allowed confocal scanning in both vertical and horizontal direction and imaging of the capsule during compression. Information about the capsule morphology was obtained at different stages of the deformation, and severe damage to the bubble was observed when large forces were applied.

Sukhorukov *et al.* [73] did a similar AFM study, but used instead a microinterferometry technique, in which the capsule shape could be reconstructed from interference pattern of monochromatic light reflecting from the capsule and a glass slide. Images of the capsule could be linked to characteristics of the deformation curve. Sudden drops and jumps in the force curve were attributed to buckling of the capsule and increased area of cantilever contact.

The microbubbles are attached to the surface by assistance of polyethylenimine. This polymer may absorb forces and contract when compression is performed, and thus, possibly influencing the measurements. The buoyancy of the microbubble is taken advantage of during the immobilization procedure, but during measurements, it will give rise to a force pulling the attached bubbles up from the surface. The force is in piconewton range for a 1-10 μm bubble, and it may stretch the polymers. When the cantilever pushes the bubble against the surface, a relaxation process may occur, and new bonds between polyethylenimine molecules and the bubble can be formed. The result can lead to alteration of the force-deformation data, possibly causing incorrect prediction of the shell stiffness and non-reproducible measurements. The effect of the PEG layer attached to the bubble surface must also be considered.

Abou-Saleh *et al.* [74] studied mechanics of lipid microbubbles encapsulated with PEG, biotin and streptavidin molecules. Force-deformation curves were obtained by compression using AFM. It was argued by the group that during the initial compressions, the support surface and the possible bubble relaxation process had unacceptable influence on the data. As a consequence, the first 10 curves were all discarded, and only subsequent

compressions used for analysis. After this number of compressions, curves with better reproducibility were reported.

This report is in accordance with what was observed when several compressions of the YM-73 casein microbubbles are performed. The force curves tend to converge and get more reproducible. The Young's modulus is calculated from the initial compressions, because there were anticipated a risk of shell damage. The variable behavior of the force curve during the first compressions, in addition to the structural observations done by Vinogradova *et al.* and Sukhorukov *et al.* during compression, indicated that deformations would damage the bubble. Yet, because of the apparent improved consistency after multiple compressions, it seems preferable to only consider curves obtained after several compressions, as long as moderate force is applied. This was just realized during the last part of the experimental work, and further work should consider doing more compressions and rather abandon the first. Minimum 10 force-deformation curves were as well required by Chen *et al.* [70], in order to ensure reproducibility of the results. Nevertheless, that curves are more reproducible does not mean that damage to the bubbles have not occurred. Better optical characterization before and after compressions could point to if the first or the tenth compression curve should be used.

The consequence of calculating the Young's modulus from the first compression is unpredictable, but it evidently causes higher uncertainty. For the microbubbles in figure 4.22b and 4.22e, there is a large difference between the first and the fourth curve. The Young's modulus is almost a factor 2 larger. There is a small, but no obvious, propensity of the Young's modulus being larger for the first compression curves. As an effect, the values of Young's modulus are possibly overestimated.

## 5.5 Implications

Microbubbles stabilized by polymeric nanoparticles are shown to be promising candidates as drug delivery devices as well as a contrast agents. Their acoustic properties are comparable to commercial contrast agents. The resonance frequencies of the nanoparticle-coated microbubbles studied in this thesis are in the frequency range 5-14 MHz. The range 2-10 MHz is normally used in medical imaging [18], meaning that the smaller microbubbles, with resonance frequency 14 MHz, are less preferable. In comparison, lipid-coated microbubbles have generally somewhat lower resonance frequencies, despite their size often being smaller. Various studies have measured attenuation peaks for lipid microbubbles in the frequency range 2.3-4.5 MHz [22, 61, 59, 60]. A thin and soft shell reduces the resonance frequency [22], while a thick and hard shell increases it [41].

In common with commercial contrast agents [22], the nanoparticle-coated microbubbles initiated non-linear radiation with higher harmonics at reasonable low pressure, comparable to the pressure amplitudes used in medical ultrasound imaging [22]. In addition, second harmonics with power at the order of the power of the fundamental are seen at higher pressure amplitudes. This points to that the microbubbles are appropriate contrast agents for harmonic imaging. In contrast to the soft lipid-shelled microbubbles, hard-shelled microbubbles have smaller oscillation amplitudes. Even so, studies have shown that nanoparticles in the microbubble shell can enhance non-linearity in the oscillations [75]. An explanation can be that nanoparticles limits compression [76]. Therefore, loading microbubbles with nanoparticles do not have to be a disadvantage in terms of ultrasound imaging performance. Instead, good contrast abilities should be expected.

Inertial cavitation of the nanoparticle-coated microbubbles is observed for insonifi-

cation at 1 MHz with pressure amplitudes above 170 kPa. Higher pressure is needed to achieve destruction when the microbubbles are insonified at higher frequency, as predicted from the Mechanical Index. Thin-shelled lipid microbubbles are observed to be disrupted at similar pressure levels [22], while bubbles with albumin shell are demonstrated to withstand pressure up to 500 kPa [66]. On the other hand, thin-shelled lipid microbubbles display subharmonic component at lower pressure than the thick-shelled (48-400 kPa versus 1000-1050 kPa with 3-5 MHz transmit frequency [63, 59, 60, 69]). Whereas the subharmonic may signify inertial cavitation for the thick-shelled bubbles [67], subharmonics from lipid microbubbles may be due to compression only-behavior and buckling effect [68].

The results mean that the nanoparticle-coated microbubbles can be destructed with ultrasound at relatively low pressure, and both higher noise level and sub- and ultraharmonics can be signs for disruption. An important implication is that ultrasound can be used to controllably induce inertial cavitation of microbubbles, and nanoparticles can be released at a target side under ultrasound image guidance.

Microbubbles with harder shells have been shown to cause larger mechanical stresses during inertial cavitation [77]. The measured Young's and shear moduli could therefore assist not only in theoretical models but also in understanding interactions of microbubbles with the capillaries. Using casein instead of BSA as surfactant protein could therefore induce more mechanical stresses on the blood vessel walls.

## 5.6 Further studies

The uncertainties of the acoustic attenuation and backscatter results are largely affected by floatation effects. An improved sample chamber design should take the buoyancy of the microbubbles into account. A simple, but effective improvement of the current design could be to let the microbubbles flow continuously into the sample chamber from a reservoir and then out from the chamber to a second container. The flow could be driven by a pump or by assistance of gravity. Inlet and outlet tubes could be pierced into the sample chamber walls. The continuous flow would ensure a more homogeneous distribution of microbubbles. The drawback would be a less portable setup. Alternatively, the sample chamber could be replaced by a tube, which also better mimics a blood vessel.

Intravenously administered microbubbles are subjected to conditions not considered in this work which possibly affects the acoustic properties of microbubbles *in vivo*. For example, the boundary a blood vessel wall give to a bubble wall may suppress its oscillation. Simulations done by Doinikov *et al.* [78] and experiments by Strasberg [79] showed that a bubble in contact with a rigid wall decreased its resonance frequency compared to a bubble oscillating with no boundary. On the other hand, simulations [78, 80] have also demonstrated that a lipid-coated bubble oscillating in contact or near a OptiCell wall increased its resonance frequency. The OptiCell wall is more plastic and reflects better than a rigid wall the properties of a vessel. Further works could involve using an OptiCell as a sample chamber for the microbubbles.

The theoretical models used for either an oscillating or compressed bubble in this work are limited due to incorrect assumptions. No models describing oscillating or compressed bubbles loaded with secondary particles have been found in literature. The complex shell involving nanoparticles makes mathematical modeling challenging, but such models

should be pursued in further works. Finite element models (FEM) have been developed and used to simulate the compression of liquid-cored microcapsules between two parallel plates [81, 82]. The models were compared with experimental data, and Young's modulus was obtained for the shell. FEM benefits from the possibility of including relevant physical factors, e.g., non-spherical shapes and inhomogeneous shells with varying thickness. The drawbacks are the time and effort required to program, and the lack of generality and applicability to other systems.

Another possible method of characterizing microbubbles is using light scattering. Tu *et al.* [83] used this approach to measure the oscillation of individual SonoVue microbubbles to estimate their shell parameters. A highly diluted suspension of bubbles were injected into a chamber where the focus of a laser and of an ultrasound beam from a transducer intersect. Bubbles oscillating in the acoustic field scattered light that were collected by a photomultiplier tube. By employing equations based on Mie scattering theory governing absorption and scattering by small particles, a curve describing the changing bubble radius as a function of time could be obtained. Theoretical calculation of the bubble oscillation obtained by the Hoff model were fitted to the experimental data by appropriate selection of the shell parameters. When compared with high-speed optical imaging, similar results were obtained. Light scattering techniques enable assess of single microbubbles responding to ultrasound with low cost compared to high-speed optical imaging and is worth considering in further studies.

# Chapter 6

# Conclusion

The preceding work has characterized acoustic and mechanical properties of microbubbles stabilized by polymeric nanoparticles, and the properties have been shown to depend on average microbubble diameter and the surfactant protein in the shell. Acoustic attenuation caused by the microbubbles have been measured, and for microbubbles stabilized by nanoparticles and Bovine Serum Albumin, the resonance frequency was demonstrated to increase with lower average diameter. Substituting BSA med casein as a surfactant protein increased the resonance frequency, despite also increasing the average diameter. Theoretical attenuation spectra calculated from the Church model and the Hoff model were fitted to the experimental attenuation spectra, and estimations for the viscoelastic shell parameters were obtained. Discrepancy between the theoretical and experimental spectra was seen, in particular around resonance. Introducing a constant multiplied with the microbubble concentration could improve the fit substantially. Because of the arbitrariness involved, it was concluded that the used models only should be used to predict attenuation coefficients distant from the resonance.

Atomic force microscopy has been used to compress microbubbles and obtain force-deformation curves. A quantification of the elastic properties of the shell was obtained by using Reissner theory on the elastic part of the force curves. There was some consistency with the results obtained by attenuation measurements, and both methods revealed that casein compared to BSA as a surfactant protein in the microbubble shell increases the stiffness of the shell. The agreement points to that AFM is an appropriate technique to assess mechanical properties of microbubbles. However, results from multiple compressions of the same microbubble argue that several compressions should be performed to get more reproducible force curves and reduce uncertainty.

Non-linear oscillations and higher harmonics were observed in backscatter spectra from all microbubbles. Radiation of higher harmonics at lower pressure could be perceived for microbubbles with casein as a surfactant protein. Similar scatter spectra were obtained for commercial microbubbles, indicating that the nanoparticle-coated microbubbles can be used as a contrast agents for ultrasound. Inertial cavitation has been demonstrated with ultrasound imaging, observation of elevated noise levels in the scatter spectra, and possibly also by presence of subharmonics. Good accordance between noise levels and disappearing microbubbles in ultrasound images was seen. Mechanical Index as low as 0.17 was shown to induce destruction, with signs for earlier onset of destruction for microbubbles with casein compared to BSA as surfactant protein. The demonstrated inertial cavitation implies that focused ultrasound exposure can be used to trigger site-specific nanoparticle release.

# Bibliography


[1] Cancer Registry of Norway. Cancer in norway 2010: Cancer incidence, mortality, survival and prevalence in norway. http://www.kreftregisteret.no/en/General/News/Cancer-in-Norway-2010, September 2012.

[2] T. Lammers, W. E. Hennink, and G. Storm. Tumour-targeted nanomedicines: Principles and practice. *British journal of cancer*, 99(3):392–397, 2008.

[3] T. Lammers. Nanomedicine on the move: from monotherapeutic regmens to combination therapies. *Expert. Rev Clin. Pharmacol.*, 5(2):105–108, 2012.

[4] J. M. Brown and A. J. Giaccia. The unique physiology of solid tumors: Opportunities (and problems) for cancer therapy. *Cancer research*, 58(7):1408–1416, 1998.

[5] S. D. Steichen, M. Caldorera-Moore, and N. A. Peppas. A review of current nanoparticle and targeting moieties for the delivery of cancer therapeutics. *European Journal of Pharmaceutical Sciences*, 48(3):416–427, 2013.

[6] R. K. Jain and T. Stylianopoulos. Delivering nanomedicine to solid tumors. *Nature Reviews Clinical Oncology*, 7(11):653–664, 2010.

[7] B. Haley and E. Frenkel. Nanoparticles for drug delivery in cancer treatment. *Urologic Oncology: Seminars and Original Investigations*, 26(1):57–64, 2008.

[8] H. Maeda. *The enhanced permeability and retention (EPR) effect in tumor vasculature: The key role of tumor-selective macromolecular drug targeting*, volume 41 of *Advances in Enzyme Regulation*. 2001.

[9] D. E. Owens III and N. A. Peppas. Opsonization, biodistribution, and pharmacokinetics of polymeric nanoparticles. *International journal of pharmaceutics*, 307(1):93–102, 2006.

[10] J. I. Fletcher, M. Haber, M. J. Henderson, and M. D. Norris. Abc transporters in cancer: More than just drug efflux pumps. *Nature Reviews Cancer*, 10(2):147–156, 2010.

[11] Mercy Afadzi. *Delivery of Encapsulated Drugs to Cancer Cells and Tissue: The Impact of Ultrasound*. PhD thesis, NTNU, 2013.

[12] F. Yuan, M. Dellian, D. Fukumura, M. Leunig, D. A. Berk, V. P. Torchilin, and R. K. Jain. Vascular permeability in a human tumor xenograft: Molecular size dependence and cutoff size. *Cancer research*, 55(17):3752–3756, 1995.

[13] W. B. Liechty and N. A. Peppas. Expert opinion: Responsive polymer nanoparticles in cancer therapy. *European Journal of Pharmaceutics and Biopharmaceutics*, 80(2):241–246, 2012.

[14] M. T. Peracchia, E. Fattal, D. Desmaële, M. Besnard, J. P. Noël, J. M. Gomis, M. Appel, J. D'Angelo, and P. Couvreur. Stealth(®) pegylated polycyanoacrylate nanoparticles for intravenous administration and splenic targeting. *Journal of Controlled Release*, 60(1):121–128, 1999.

[15] M. Wang and M. Thanou. Targeting nanoparticles to cancer. *Pharmacological Research*, 62(2):90–99, 2010.

[16] V. F. Humphrey. Ultrasound and matter-physical interactions. *Progress in biophysics and molecular biology*, 93(1-3):195–211, 2007.

[17] Jan R. Lien and Gunnar Løvhøiden. *Generell fysikk for universiteter og høyskoler*, volume 1. Universitetsforlaget, 2001.

[18] B. A. J. Angelsen. *Ultrasound Imaging*. Emantec, Trondheim, Norway, 2000.

[19] J. Wu and W. L. Nyborg. Ultrasound, cavitation bubbles and their interaction with cells. *Advanced Drug Delivery Reviews*, 60(10):1103–1116, 2008.

[20] J. Powers, T. R. Porter, S. Wilson, M. Averkiou, D. Skyba, and M. Bruce. Ultrasound contrast imaging research. *MEDICA MUNDI*, 44(2), 2000.

[21] S. Tinkov, R. Bekeredjian, G. Winter, and C. Coester. Microbubbles as ultrasound triggered drug carriers. *Journal of pharmaceutical sciences*, 98(6):1935–1961, 2009.

[22] Lars Hoff. *Acoustic characterization of contrast agents for medical ultrasound imaging*. PhD thesis, NTNU, 2000.

[23] E. Stride. Physical principles of microbubbles for ultrasound imaging and therapy. *Cerebrovascular Diseases*, 27(SUPPL. 2):1–13, 2009.

[24] R. Gramiak and P. M. Shah. Echocardiography of the aortic root. *Investigative radiology*, 3(5):356–366, 1968.

[25] T. Faez, M. Emmer, K. Kooiman, M. Versluis, A. Van Der Steen, and N. De Jong. 20 years of ultrasound contrast agent modeling. *IEEE transactions on ultrasonics, ferroelectrics, and frequency control*, 60(1):7–20, 2013.

[26] F. Kiessling, S. Fokong, P. Koczera, W. Lederle, and T. Lammers. Ultrasound microbubbles for molecular diagnosis, therapy, and theranostics. *Journal of Nuclear Medicine*, 53(3):345–348, 2012.

[27] E. P. Stride and C. C. Coussios. Cavitation and contrast: The use of bubbles in ultrasound imaging and therapy. *Proceedings of the Institution of Mechanical Engineers, Part H: Journal of Engineering in Medicine*, 224(2):171–191, 2010.

[28] N. de Jong, M. Emmer, C. T. Chin, A. Bouakaz, F. Mastik, D. Lohse, and M. Versluis. "compression-only" behavior of phospholipid-coated contrast bubbles. *Ultrasound in Medicine and Biology*, 33(4):653–656, 2007.

[29] M. Emmer, A. van Wamel, D. E. Goertz, and N. de Jong. The onset of microbubble vibration. *Ultrasound in Medicine and Biology*, 33(6):941–949, 2007.

[30] A. Schroeder, J. Kost, and Y. Barenholz. Ultrasound, liposomes, and drug delivery: principles for using ultrasound to control the release of drugs from liposomes. *Chemistry and physics of lipids*, 162(1-2):1–16, 2009.

[31] Y. T. Didenko, W. B. McNamara, and K. S. Suslick. Temperature of multibubble sonoluminescence in water. *Journal of Physical Chemistry A*, 103(50):10783–10788, 1999.

[32] R. Metoki, F. Moriyasu, N. Kamiyama, K. Sugimoto, H. Iijima, H. . Xu, T. Aoki, Y. Miyata, K. Yamamoto, K. Kudo, M. Shimizu, and M. Yamada. Quantification of hepatic parenchymal blood flow by contrast ultrasonography with flash-replenishment imaging. *Ultrasound in Medicine and Biology*, 32(10):1459–1466, 2006.

[33] W. G. Pitt, G. Husseini, and B. J. Staples. Ultrasonic drug delivery - a general review. *Expert Opinion on Drug Delivery*, 1(1):37–56, 2004.

[34] L. J. M. Juffermans, O. Kamp, P. A. Dijkmans, C. A. Visser, and R. J. P. Musters. Low-intensity ultrasound-exposed microbubbles provoke local hyperpolarization of the cell membrane via activation of bkca channels. *Ultrasound in Medicine and Biology*, 34(3):502–508, 2008.

[35] Lord Rayleigh. *The Theory of Sound*, volume 2. Dover Publications, New York, USA, 1945.

[36] M. Minnaert. On musical air-bubbles and the sounds of running water. *Philos.Mag.*, 16:235–248, 1933.

[37] L. Rayleigh. On the pressure developed in a liquid during the collapse of a spherical cavity. *Phil.Mag.*, 34(200):94–98, 1917.

[38] M. S. Plesset. The dynamics of cavitation bubbles. *J.Appl.Mech.*, 16:277–282, 1949.

[39] B. E. Noltingk and E. A. Neppiras. Cavitation produced by ultrasonics. *Proceedings of the Physical Society.Section B*, 63(9):674–685, 1950.

[40] C. C. Church. The effects of an elastic solid surface layer on the radial pulsations of gas bubbles. *Journal of the Acoustical Society of America*, 97(3):1510–1521, 1995.

[41] D. Grishenkov, C. Pecorari, T. B. Brismar, and G. Paradossi. Characterization of acoustic properties of pva-shelled ultrasound contrast agents: Linear properties (part i). *Ultrasound in Medicine and Biology*, 35(7):1127–1138, 2009.

[42] K. W. Commander and A. Prosperetti. Linear pressure waves in bubbly liquids: Comparison between theory and experiments. *J.Acoust.Soc.Am.*, 85(2):732–746, 1989.

[43] L. Hoff, P. C Sontum, and J. M. Hovem. Oscillations of polymeric microbubbles: Effect of the encapsulating shell. *J.Acoust.Soc.Am.*, 107(4):2272–2280, 2000.

[44] A. A. Doinikov and A. Bouakaz. Review of shell models for contrast agent microbubbles. *IEEE transactions on ultrasonics, ferroelectrics, and frequency control*, 58(5):981–993, 2011.

[45] Compendium tfy4265 biophysical micromethods, 2012.

[46] Andreas Finnøy. Characterization and mechanical properties of microbubbles stabilized by nanoparticles. Prosjektoppgave, NTNU.

[47] W. C. Oliver and G. M. Pharr. Measurement of hardness and elastic modulus by instrumented indentation: Advances in understanding and refinements to methodology. *Journal of Materials Research*, 19(1):3–20, 2004.

[48] R. Lakes. Meaning of poisson's ratio, February 2012. http://silver.neep.wisc.edu/ lakes/PoissonIntro.html.

[49] E. Reissner. Stresses and small displacements of shallow spherical shells. *J.Math.Phys.*, 25:80–85, 1946.

[50] E. Reissner. Stresses and small displacements of shallow spherical shells, ii. *J.Math.Phys.*, 25(4):279–300, 1946.

[51] E. Glynos, V. Koutsos, W. N. McDicken, C. M. Moran, S. D. Pye, J. A. Ross, and V. Sboros. Nanomechanics of biocompatible hollow thin-shell polymer microspheres. *Langmuir*, 25(13):7514–7522, 2009.

[52] N. Elsner, F. Dubreuil, R. Weinkamer, M. Wasicek, F. D. Fischer, and A. Fery. Mechanical properties of freestanding polyelectrolyte capsules: A quantitative approach based on shell theory. *Progress in Colloid and Polymer Science*, 132:117–123, 2006.

[53] E. Glynos, V. Sboros, and V. Koutsos. Polymeric thin shells: Measurement of elastic properties at the nanometer scale using atomic force microscopy. *Materials Science and Engineering B: Solid-State Materials for Advanced Technology*, 165(3):231–234, 2009.

[54] E. Buchner Santos, J. K. Morris, E. Glynos, V. Sboros, and V. Koutsos. Nanomechanical properties of phospholipid microbubbles. *Langmuir*, 28(13):5753–5760, 2012.

[55] A. Fery, F. Dubreuil, and H. Möhwald. Mechanics of artificial microcapsules. *New Journal of Physics*, 6:1–13, 2004.

[56] Marit Ulset Sandsaunet. Etablering av metoder for bestemmelse av mekaniske egenskaper for gassbobler. Prosjektoppgave, NTNU.

[57] Andreas Bøe. Prosjektoppgave, NTNU.

[58] W. Schmidt and G. Roessling. Novel manufacturing process of hollow polymer microspheres. *Chemical Engineering Science*, 61(15):4973–4981, 2006.

[59] K. Sarkar, W. T. Shi, D. Chatterjee, and F. Forsberg. Characterization of ultrasound contrast microbubbles using in vitro experiments and viscous and viscoelastic interface models for encapsulation. *Journal of the Acoustical Society of America*, 118(1):539–550, 2005.

[60] Y. . Gong, D. Zhang, X. . Gong, K. . Tan, and Z. Liu. The viscoelasticity of lipid shell and the hysteresis of subharmonic in liquid containing microbubbles. *Chinese Physics*, 15(7):1526–1531, 2006.

[61] J. . Yu, D. Zhang, X. . Gong, Y. . Gong, Z. . Zhu, and X. . Liu. Frequency dependences of sound attenuation and phase velocity in suspensions containing encapsulated microbubbles. *Chinese Physics Letters*, 22(4):892–895, 2005.

[62] D. E. Goertz, M. E. Frijlink, M. M. Voormolen, N. de Jong, and A. F. W. van der Steen. High frequency attenuation measurements of lipid encapsulated contrast agents. *Ultrasonics*, 44(SUPPL.):e131–e134, 2006.

[63] N. de Jong, M. Emmer, A. van Wamel, and M. Versluis. Ultrasonic characterization of ultrasound contrast agents. *Medical and Biological Engineering and Computing*, 47(8):861–873, 2009.

[64] E. Silberman. Sound velocity and attenuation in bubbly mixtures measured in a standing wave tube. *J.Acoust.Soc.Am.*, 29:925–933, 1957.

[65] I.S Kol'tsova, L. O. Krynskii, I. G. Mikhalov, and I. E. Pokrovskaya. Attenuation of ultrasonic waves in low-viscosity liquid containing gas bubbles. *Akust. Zh.*, 25:725–731, 1979.

[66] P. J. A. Frinking, N. de Jong, and E.I. Cespedes. Scattering properties of encapsulated gas bubbles at high ultrasound pressures. *Journal of the Acoustical Society of Americal*, 105:1989–1996, 1999.

[67] A. Prosperetti. Nonlinear oscillation of gas bubbles in liquids: Transient solutions and the connection between subharmonic signal and cavitation. *Journal of the Acoustical Society of America*, 57:810–821, 1975.

[68] P. Marmottant, S. Van Der Meer, M. Emmer, M. Versluis, N. De Jong, S. Hilgenfeldt, and D. Lohse. A model for large amplitude oscillations of coated bubbles accounting for buckling and rupture. *Journal of the Acoustical Society of America*, 118(6):3499–3505, 2005.

[69] W. T. Shi and F. Forsberg. Ultrasonic characterization of the nonlinear properties of contrast microbubbles. *Ultrasound in Medicine and Biology*, 26(1):93–104, 2000.

[70] C. C. Chen, S. . Wu, J. Finan, B. Morrison, and E. Konofagou. An experimental study on the stiffness of size-isolated microbubbles using atomic force microscopy. *IEEE transactions on ultrasonics, ferroelectrics, and frequency control*, 60(3):524–534, 2013.

[71] N. De Jong, L. Hoff, T. Skotland, and N. Bom. Absorption and scatter of encapsulated gas filled microspheres: Theoretical considerations and some measurements. *Ultrasonics*, 30(2):95–103, 1992.

[72] O. I. Vinogradova, O. V. Lebedeva, and B. S. Kim. Mechanical behavior and characterization of microcapsules. *Annual Review of Materials Research*, 36:143–178, 2006.

[73] F. Dubreuil, N. Elsner, and A. Fery. Elastic properties of polyelectrolyte capsules studied by atomic-force microscopy and ricm. *European Physical Journal E*, 12(2):215–221, 2003.

[74] R. H. Abou-Saleh, S. A. Peyman, K. Critchley, S. D. Evans, and N. H. Thomson. Nanomechanics of lipid encapsulated microbubbles with functional coatings. *Langmuir*, 29(12):4096–4103, 2013.

[75] J. I. Park, D. Jagadeesan, R. Williams, W. Oakden, S. Chung, G. J. Stanisz, and E. Kumacheva. Microbubbles loaded with nanoparticles: A route to multiple imaging modalities. *ACS Nano*, 4(11):6579–6586, 2010.

[76] E. Stride, K. Pancholi, M. J. Edirisinghe, and S. Samarasinghe. Increasing the nonlinear character of microbubble oscillations at low acoustic pressures. *Journal of the Royal Society Interface*, 5(24):807–811, 2008.

[77] S. Mehier-Humbert, F. Yan, P. Frinking, M. Schneider, R. H. Guy, and T. Bettinger. Ultrasound-mediated gene delivery: Influence of contrast agent on transfection. *Bioconjugate chemistry*, 18(3):652–662, 2007.

[78] A. A. Doinikov, L. Aired, and A. Bouakaz. Dynamics of a contrast agent microbubble attached to an elastic wall. *IEEE Transactions on Medical Imaging*, 31(3):654–662, 2012.

[79] M. Strasberg. The pulsation frequency of nonspherical gas bubbles in liquids. *J.Acoust.Soc.Am.*, 25(3):536–537, 1953.

[80] L. Aired, A. A. Doinikov, and A. Bouakaz. Effect of an elastic wall on the dynamics of an encapsulated microbubble: A simulation study. *Ultrasonics*, 53(1), 2013.

[81] R. Mercadé-Prieto and Z. Zhang. Mechanical characterization of microspheres capsules, cells and beads: A review. *Journal of microencapsulation*, 29(3):277–285, 2012.

[82] R. Mercadé-Prieto, B. Nguyen, R. Allen, D. York, J. A. Preece, T. E. Goodwin, and Z. Zhang. Determination of the elastic properties of single microcapsules using micromanipulation and finite element modeling. *Chemical Engineering Science*, 66(10):2042–2049, 2011.

[83] J. Tu, J. Guan, Y. Qiu, and T. J. Matula. Estimating the shell parameters of sonovue® microbubbles using light scattering. *Journal of the Acoustical Society of America*, 126(6):2954–2962, 2009.